Die approbierte Originalversion dieser Diplom-/Masterarbeit ist in der Hauptbibliothek der Technischen Universität Wien aufgestellt und zugänglich.
http://www.ub.tuwien.ac.at

The approved original version of this diploma or master thesis is available at the main library of the Vienna University of Technology.
http://www.ub.tuwien.ac.at/eng

Unterschrift Betreuer

DIPLOMARBEIT

Beam Emittance Preservation and Tuning in the FCC-ee Lepton Collider

ausgeführt am Atominstitut
der Technischen Universität Wien
und am CERN

unter der Anleitung von
Privatdoz. Dipl.-Ing. Dr.techn. Michael Benedikt
Berhard Holzer, PhD

durch

Andreas Doblhammer, BSc

Theresianumgasse 6/23
1040 Wien

March 2, 2018

Unterschrift Student

Kurzfassung

Aufgrund der langen Planungs- und Bauzeit von Teilchenbeschleunigern hat die "European Strategy Group for High Energy Physics" die Empfehlung ausgesprochen, bereits jetzt mögliche Nachfolgeprojekte des LHC zu entwickeln. Daher wurde die sogenannte "Future Circular Collider (FCC)" Design Studie ins Leben gerufen, welche unter der Leitung des CERN den Nutzen und die Realisierbarkeit neuer Speicherringe für Teilchenkollisionen im Hinblick auf die Beantwortung aktueller Fragen der Teilchenphysik und die Suche nach Physik jenseits des Standard-Modells untersucht.

Im Elektron-Positron Speicherring dieser Studie, FCC-ee, verursacht Synchrotronstrahlung große Abweichungen des Strahles von seiner Designenergie. Die Energieabweichungen führen ihrerseits zu Verschiebungen im Orbit und verursachen den sogenannten Sawtooth-Effekt. Der Teilchenstrahl durchläuft daher die Magneten des Speicherringes nicht mittig. Dies erzeugt über den Feed-down Effekt zusätzliche, störende Magnetfelder, welche die Strahloptik und die Emittanz beeinflussen. Um den Sawtooth-Effekt und damit auch den Feed-down Effekt zu korrigieren, können Dipolmagnete im Speicherring an die lokale Strahlenergie angepasst werden. Dieser Prozess wird Dipol-Tapering genannt. Im Laufe dieser Arbeit werden verschiedene Taperingszenarien in Hinblick auf Effektivität, Realisierbarkeit und Kosten verglichen und ihr Einfluss auf die Strahloptik und Emittanz wird untersucht.

Das zweite Kapitel der Arbeit beschäftigt sich mit der direkten Justierung der Strahlemittanz durch Wiggler. Ein Idealwert der Strahlemittanz führt zu einem Maximum der Luminosität. Zahlreiche Faktoren in einem Speicherring führen jedoch zu kleinen Abweichungen der Emittanz von diesem Idealwert. Um diesen Wert nachträglich wiederherzustellen, werden Wiggler eingesetzt. In dieser Arbeit werden verschiedene Wigglerdesigns vorgestellt, welche als Anregungswiggler die Strahlemittanz erhöhen und als Dämpfungwiggler die Emittanz erniedrigen. Es wird gezeigt, dass eine Emittanzerhöhung bzw -absenkung von 10 % mit einer akzeptablen Zunahme von Synchrotronstrahlung möglich ist.

Das letzte Kapitel der Arbeit fokussiert sich auf die Korrektur der Chromatizität in FCC-ee und den Einfluss einer solchen Chromatizitätskorrektur auf die Strahlemittanz. Systeme zur Chromatizitätskontrolle mit unterschiedlicher Anzahl von Sextupol-Familien wurden in den Speicherring eingebaut. Die Stärken dieser Sextupole wurden mit einem Downhill-Simplex Optimierungsalgorithmus angepasst, welcher die Chromatizität bis zur vierten Ordnung korrigiert. Berechnungen der Emittanz vor und nach dem Einbau der Chromatitzätskorrektur zeigen, dass diese einen nicht zu vernachlässigenden Einfluss auf die Emittanz haben können, welcher bei der Planung der Korrektursysteme berücksichtigt werden muss.

Abstract

Following the recommendations of the European Strategy Group for High Energy Physics, CERN launched the Future Circular Collider Study (FCC) to investigate the feasibility of large-scale circular colliders for future high energy physics research. In the electron-positron collider of the study, FCC-ee, large synchrotron radiation losses cause the beam to have large local deviations from the design energy. These energy deviations cause orbit offsets and create the so-called sawtooth effect, which causes particles to pass the magnets of the accelerator off-centre. This in turn causes perturbing magnetic fields via the feed-down effect. In order to correct the sawtooth effect and therefore the feed-down effect, the dipole magnets in the machine can be adjusted to the local beam energy in a process called dipole tapering. In the course of this thesis, different dipole magnet tapering scenarios are compared in terms of their effectiveness, feasibility and cost.

Furthermore, this thesis focuses on tuning the horizontal beam emittance using wigglers. A small value of the beam emittance corresponds to a small beam cross-section, resulting in an increased likelihood of particle collisions and thus a higher luminosity. However, a number of perturbations can cause the beam emittance to deviate from its design value. In order to restore the design emittance, wigglers are implemented in the accelerator lattice. Different wiggler designs will be presented for both decreasing and increasing the value of the horizontal beam emittance. It will be shown, that an emittance decrease and increase by a factor of 10 % with an acceptable increase in synchrotron radiation is possible.

The last section of this thesis focuses on chromaticity correction in FCC- ee and its influence on the beam emittance. Chromaticity correction schemes with varying numbers of sextupole families are implemented into the FCC-ee lattice. Sextupole strengths are optimized using a downhill simplex algorithm in order to reduce chromaticities up to the fourth order. Finally, emittance calculations after the application of each correction scheme show, that chromaticity correction schemes can have a significant influence on the beam emittance, which should be considered in the design of these correction schemes.

Contents

1 Introduction

Following the recommendation of the European Strategy Group for High Energy Physics, a five-year international "Future Circular Collider" (FCC) design study was initiated at CERN in February 2014, representing the combined efforts of several international institutes. This study covers three new accelerators in order to delve into questions of particle physics yet to be answered, such as: the existence and nature of dark matter and dark energy, the origin of the non-zero neutrino masses, the reason for the mass of the Higgs boson being at approximately 125.4 GeV/c^2, as well as the apparent asymmetry in the distribution of matter and antimatter in the early universe. The three accelerators included in the FCC study, each with a circumference of 80 to 100 km, are:

- A proton-proton collider (FCC-hh), aiming for a center-of-mass energy of 100 TeV and thus accessing a whole new energy region and representing the new frontier of high-energy physics. In order for FCC-hh to reach its peak energy, dipole strengths between 16 and 20 T are required.
- A proton-electron collider (FCC-he) for deep elastic scattering experiments of hadrons and leptons in order to precisely study the quark structure of the proton.
- An electron-positron collider (FCC-ee) with a center-of-mass energy between 90 and 350 GeV, which is the basis for the work done in this thesis. The FCC-ee is intended to be a machine for high-precision measurements of the Higgs boson and other, already known particles like the W and Z bosons and the top quark, as well as an instrument to observe rare decay events.

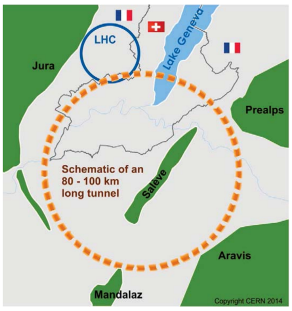

Figure 1: Schematic of a 80-100 km tunnel for the FCC in the Lake Geneva basin

FCC-ee is optimized for four different center-of-mass energies:

- the Z pole at 90 GeV
- the W pair production threshold at 160 GeV
- the H production at 240 GeV
- the $t\bar{t}$ threshold at 350 GeV

Electrons and positrons are (according to current knowledge) point-like particles, hence their center-of-mass energy can be measured precisely. This allows for precision measurements of the produced particles like the W and Z bosons, the Higgs boson, as well as the top quark. An overview of some baseline parameters of FCC-ee, which are relevant for the calculations and simulations in this thesis, is given in the following table:

Table 1: Overview of FCC-ee baseline parameters at different energies

	Z	**W**	**H**	**$\mathbf{t\bar{t}}$**
Beam energy (GeV)	45.5	80	120	175
Horizontal emittance ϵ_x (nm)	0.09	0.26	0.61	1.3
Vertical emittance ϵ_y (pm)	1	1	1.2	2.5
Beta function at IP				
- Horizontal β_x (m)	1	1	1	1
- Vertical β_y (mm)	2	2	2	2
Synchrotron radiation power P_γ (MW)	50	50	50	50
Energy loss / turn (GeV)	0.03	0.33	1.67	7.55
Total RF voltage (GV)	0.2	0.8	3	10

These parameters are currently fulfilled by two different designs, the 12-fold and the racetrack layout. Tables (2) and (3) list the main parameters of these two designs. The 12-fold layout consists of 12 arc sections with a length of 6.8 km each and 12 straight sections with a length of 1.5 km each. This layout reproduces the general requirements of a 100 km lepton accelerator and was thus used for first studies of beam dynamics. In the racetrack layout, there are two different arc sections. Four short arc sections (SARC) with a length of 4.4 km each and four long arc sections (LARC) with a length of 16.4 km each. Six long straight sections (LSS) with a length of 1.4 km and two extended straight sections (ESS) with a length of 4.2 km separate the arc sections. This layout incorporates input of the civil-engineering group regarding the boundary conditions of the Geneva basin and is already in agreement with the requirements of the hadron collider (FCC-hh).

Figures (2) and (3) show a schematic overview of the FCC-ee 12-fold and racetrack lattices, each with two radiofrequency (RF) sections installed.

One of the main problems of circular lepton colliders is synchrotron radiation. At an energy of 175 GeV, the energy loss due to synchrotron radiation in FCC-ee is approximately 7.5 GeV per turn. Other high energy lepton colliders currently in design, like the *International Linear Collider (ILC)* and the *Compact Linear Collider (CLIC)*, circumvent this problem by using a different approach. They are designed as linear accelerators, because in linear acceleration the energy loss due to synchrotron radiation is negligible. However, one

Table 2: Main parameters of FCC-ee 12fold lattice at 175 GeV

Circumference	99.6 km
Energy loss per turn	$\approx$ 8078 MeV
Synchrotron radiation power per beam	50 MW
Critical energy in the arcs	1.13 MeV
Horizontal design emittance	1.6 nm

Table 3: Main parameters of FCC-ee racetrack lattice at 175 GeV

Circumference	100 km
Energy loss turn	$\approx$ 7800 MeV
Synchrotron Radiation Power per beam	50 MW
Critical energy in the arcs	1.13 MeV
Horizontal design emittance	1 nm/2 nm

of the main goals of FCC-ee will be to precisely measure the Higgs boson, which has a mass of approximately 126 GeV/c^2. Within an energy range of up to 400 GeV, circular colliders have one great advantage over linear colliders. They are able to achieve a luminosity which is up to two orders of magnitude higher, mainly because in a circular collider particles can be stored for much longer periods of time. With the current baseline parameters, the FCC-ee will be able to achieve a higher luminosity than any other comparable lepton collider currently in design.

The synchrotron radiation losses in FCC-ee, however, cause the beam to have large local deviations from the design energy. These energy deviations cause orbit offsets and create the so-called sawtooth effect as well as optics distortions due to quadrupole focussing errors. In order to reduce these orbit offsets, the dipole magnets in the machine can be adjusted to the local beam energy. This process is referred to as dipole tapering. In the course of this thesis, different dipole magnet tapering scenarios will be compared in terms of their effectiveness, feasibility and cost. Additionally, their influence on the beam optics will be determined.

Furthermore, this thesis will focus on tuning the horizontal beam emittance using wigglers. The beam emittance is a parameter which describes an area in phase space. A point in phase space represents one specific setting of position and momentum variables. Therefore, the beam emittance represents the entirety of possible positions and momenta the particles of a beam can occupy. A small value of the beam emittance corresponds to a small beam cross-section, resulting in an increased likelihood of particle collisions and thus a higher luminosity.

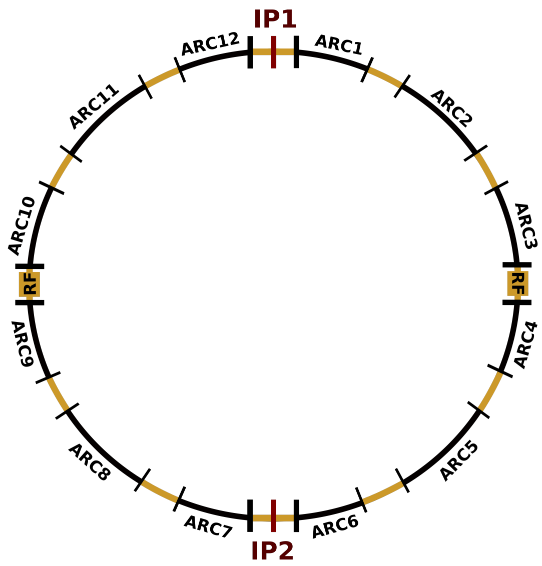

Figure 2: Schematic of the FCC-ee 12fold lattice. Arcs are depicted in black, straight sections in yellow. Insertion points (IPs) and radiofrequency (RF) sections are labelled. The arcs have a length of 6.8 km each, the straight sections have a length of 1.5 km each.

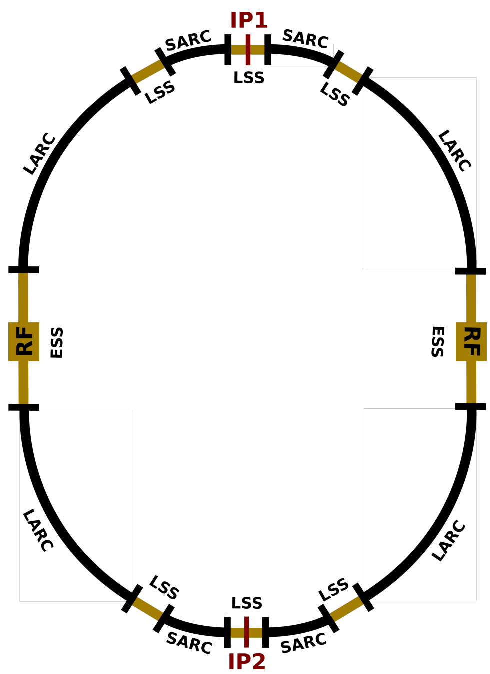

Figure 3: Schematic of the FCC-ee racetrack lattice. Arcs are depicted in black, straight sections in yellow. Insertion points (IPs) and radiofrequency (RF) sections are labelled. The shorts arcs (SARC) have a length of 4.4 km, the long arcs (LARC) have a length of 16.4 km. The long straight sections (LSS) have a length of 1.4 km, the extended straight sections (ESS) are 4.2 km long. This geometry, which has been chosen for the project, is the result of an optimization considering the boundary conditions of the Geneva region and the layout of the hadron version of the FCC study.

However, a number of perturbations can cause the beam emittance to deviate from its design value. In order to restore the design emittance, wigglers are implemented in the accelerator lattice. In this thesis, different wiggler designs will be presented for both de- and increasing the value of the horizontal beam emittance.
The last section of this thesis focuses on chromaticity correction in FCC-ee and its influence on the beam emittance. Chromaticity correction schemes with varying numbers of sextupole families are implemented into the FCC-ee lattice. Sextupole strengths are optimized using a downhill simplex algorithm in order to reduce chromaticities up to the fourth order. Finally, emittance calculations after the application of each correction scheme will determine, whether the correction schemes have any influence on the beam emittance, which should be considered in the design.

2 Concepts of Beam Dynamics in Electron Storage Rings

In this section, a few concepts will be explained in order to understand the physics of an electron storage ring.
In storage rings, particles are moving within a magnetic field. This field can be expanded into multipole terms according to the following formula:

$$
\begin{aligned}
\frac{e}{p}B_y(x) &= \frac{e}{p}B_{y0} + \frac{e}{p}\frac{dB_y}{dx}x + \frac{1}{2!}\frac{e}{p}\frac{d^2B_y}{dx^2}x^2 + \frac{1}{3!}\frac{e}{p}\frac{d^3B_y}{dx^3}x^3 + \ldots \\
&= \underbrace{\frac{1}{\rho}}_{\text{Dipole}} + \underbrace{K_1x}_{\text{Quadrupole}} + \underbrace{\frac{1}{2!}K_2x^2}_{\text{Sextupole}} + \underbrace{\frac{1}{3!}K_3x^3}_{\text{Octupole}} + \ldots
\end{aligned}
\tag{1}
$$

where ρ is the bending radius of the dipole magnet and K_i represents the strength of the i-th multipole. In most cases, separate function magnets are used, where each multipole serves a different purpose. Dipoles are used to bend the beam along the design orbit and quadrupoles are used to focus the beam. While quadrupoles with a focussing effect in the horizontal plane have a defocussing effect in the vertical and vice versa, a sequence of alternating focussing and defocussing quadrupoles can lead to an overall focussing of the beam in both planes. An example of this focussing strategy, which is used in most high energy accelerators, is the so-called FODO-lattice.

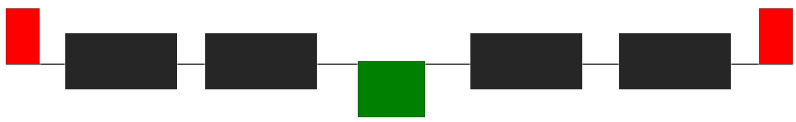

Figure 4: Typical layout of a FODO lattice. The red elements represent focussing quadrupoles, the green a defocussing quadrupole and the black elements represent dipoles.

Multipoles of a higher order are used to correct errors of the linear beam optics. Specifically, sextupoles are used to correct quadrupole focussing errors due to the momentum dependent quadrupole strength

$$K_1(p) = \frac{e}{p}\frac{dB_y}{dx}. \tag{2}$$

This momentum dependency of the quadrupole focussing strength leads to the so-called *natural chromaticity* of an accelerator.
The *accelerator lattice* or *magnetic lattice* is a periodic sequence of magnets. If the lattice

only contains dipoles and quadrupoles, it is called a *linear lattice*.

Equations of Motion In order to calculate the beam dynamics of a storage ring, it is most convenient to use a curvilinear coordinate system (x, y, z), which follows a reference particle with design energy at its reference orbit. In this right-handed reference system, which is also called the *Frenet-Serret Coordinate System*, the z-axis is the tangent to the reference orbit s. x and y are orthogonal to z with x pointing into the direction of radial vector ρ and are called the horizontal and vertical orbit offsets, respectively (see figure 5).

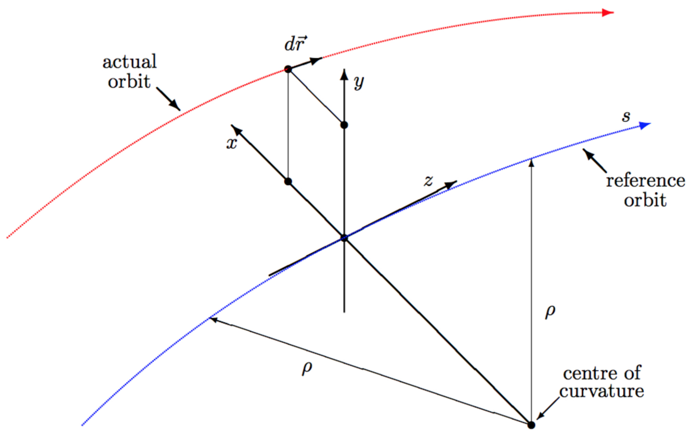

Figure 5: Curvilinear Frenet-Serret coordinate system used in accelerator physics

Using these coordinates, the linear equations of motion for the transverse planes are [6]

$$x'' + K_x x = 0 \quad , \quad K_x = \frac{e}{p}\frac{\partial B_y}{\partial x} + \frac{1}{\rho^2} \tag{3}$$

$$y'' + K_y y = 0 \quad , \quad K_y = -\frac{e}{p}\frac{\partial B_x}{\partial y}. \tag{4}$$

with K_i describing the horizontal and vertical focussing properties of the accelerator. The additional factor of $\frac{1}{\rho^2}$ contributing to the horizontal focussing is due to the so-called *weak focussing* of dipole magnets, a purely geometrical effect.

A differential equation of the type

$$\frac{d^2x}{ds^2} + K(s)x = 0 \tag{5}$$

is called *Hill equation* and can be solved following *Floquet's theorem*. The general solution to this type of differential equation is

$$x(s) = \sqrt{\epsilon}\sqrt{\beta(s)}\cos(\Psi(\mathrm{s}) + \phi). \tag{6}$$

This solution describes a pseudo-harmonic oscillation with a position-dependent ampli-

tude $\sqrt{\epsilon\beta(s)}$ and phase $\Psi(\mathrm{s}) + \phi$. The phase factor $\Psi(s)$ and the *beta function* $\beta(s)$ are determined by the magnetic focussing properties and thus by the magnet structure of the lattice. ϕ is a constant phase factor determined by initial conditions. ϵ is a constant of motion called *beam emittance* and will be explained later in this section.
As betatrons played an important role in the development of the theory of transverse particle oscillations around a design orbit, this form of oscillation kept the name *betatron oscillation.*

Tune The *phase advance* between two positions of an accelerator lattice is given by

$$\mu_u := \Delta\Psi_u = \Psi_u(s_2) - \Psi_u(s_1) \tag{7}$$

It is defined by the beta function and thus by the lattice elements between these points:

$$\mu_u := \int_{s_1}^{s_2} \frac{1}{\beta(s)} ds. \tag{8}$$

u stands for either x or y. The *tune* Q_u is defined as the phase advance of a full revolution, in units of 2π.

$$Q_u := \frac{\mu_u}{2\pi} = \frac{1}{2\pi} \oint \frac{ds}{\beta_u(s)}, \tag{9}$$

The tune represents the number of horizontal or vertical oscillations a particle undergoes during a full revolution in an accelerator. The choice of the correct tune or *working point* is crucial for the performance of an accelerator, for with a poorly chosen working point the beam can fulfill a so-called resonance condition. In a real storage ring, there are always errors due to slightly misaligned magnets or slight variations in the magnetic field. Normally, a particle passes these errors with a different betatron phase each turn, resulting in randomly different deflections. In case of an integer resonance, however, the betatron phase of each turn is a multiple of π. This results in the deflections adding up each turn, effectively destabilising the beam. The same is true for a n-th-order resonance, where the betatron phase of each turn is a multiple of $\frac{\pi}{n}$. Here, the deflections of every n-th revolution add up. Referring to one plane, the resonance condition is therefore:

$$mQ_u := n \quad (m, n \in \mathbf{Z}), \tag{10}$$

Dispersion Equation (6) describes the general solution to the equations of motion for particles with reference momentum p_0. In a storage ring, however, deviations from the design momentum occur, which are caused by

- energy loss due to synchrotron radiation, as well as
- energy gain in radiofrequency (RF) cavities.

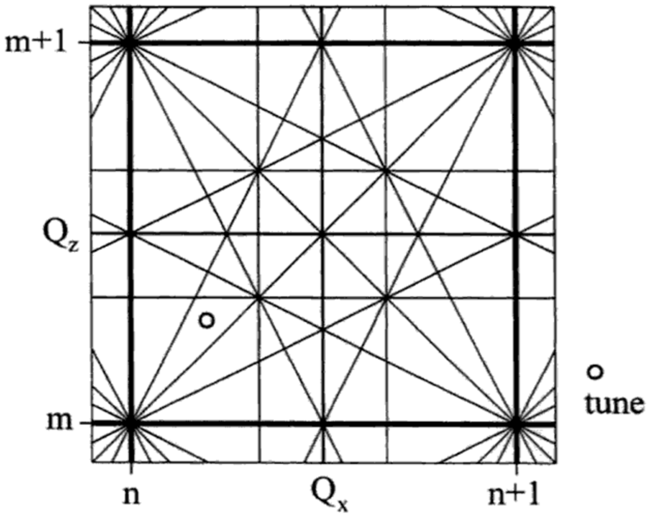

Figure 6: Tune diagram in both planes with optical resonances up to third order. A possible working point is marked.

According to

$$\frac{1}{\rho} = \frac{e}{p} B_y, \tag{11}$$

the bending radius of a dipole with the strength B_y depends on the particle momentum. Thus, particles with different momenta move through the accelerator lattice on different trajectories. The dependence of the trajectory on the particle momentum is called dispersion. Trajectories of particles with a momentum deviation $\frac{\Delta p}{p_0}$ contain an additional term

$$u_\mathrm{D}(s) = u_\beta + D_u(s) \frac{\Delta p}{p_0} \tag{12}$$

where $D_u(s)$ is the dispersion function of the respective plane. In linear approximation, the dispersion function satisfies the inhomogeneous equation of motion

$$D_u''(s) + K_u D_u(s) = \frac{1}{\rho} \tag{13}$$

and represents the closed orbit for a relative momentum deviation $\frac{\Delta p}{p_0}$ of 1. As a consequence, in electron storage rings, the antagonistic effects of energy loss via synchrotron radiation and energy gain in RF cavities lead to a characteristic oscillation of the local momentum and, via the dispersion function, to an oscillating orbit, the so-called sawtooth trajectory (see figure 7).

In an ideal accelerator, dispersion only occurs in the horizontal plane as there are no dipole fields in vertical direction. However, if imperfections are taken into account, vertical dispersion is caused by magnet misalignments, field errors of magnets and fringe field effects.

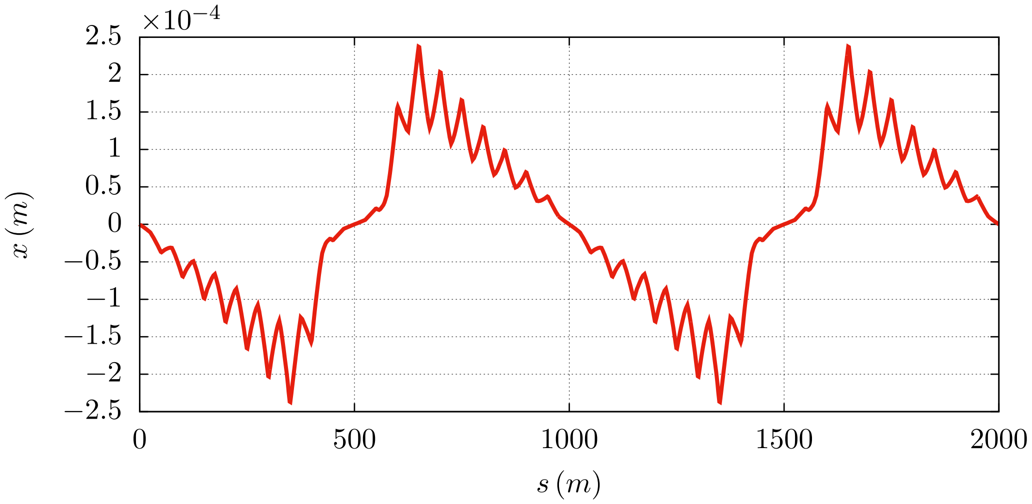

Figure 7: Example of a sawtooth trajectory of a particle in an accelerator. Due to the energy loss caused by synchrotron radiation, the particle drifts inward and the orbit offset becomes negative. After passing the RF cavities in the straight section, the particle has gained energy and therefore drifts onto an outer dispersion trajectory in the following arc.

Synchrotron Oscillation A particle in an accelerator oscillates not only in the transverse planes, but also in the longitudinal plane. The longitudinal oscillation is called synchrotron oscillation and is caused by consecutive loss and gain of energy throughout the accelerator. It is a harmonic oscillation, which follows the equation

$$\Delta\ddot{E} + \Omega^2 \Delta E = 0 \tag{14}$$

with the synchrotron oscillation frequency Ω. As explained above, particles with a relative momentum deviation $\frac{\Delta p}{p_0}$ move on dispersion trajectories (see eq. (12)). In high-energy accelerators, the particle velocity is only marginally different from the speed of light and stays constant for small variations of energy. Therefore, the time a particle requires to travel the distance between two RF cavities becomes dependent on the particle energy. Inside the RF cavity, there is an oscillating electric field. Its phase is set in a way that causes a particle on the design orbit to gain exactly the amount of energy it lost via synchrotron radiation. This value of the phase of the electric field inside the RF cavity will be referred to as the design phase. A particle on an inner dispersion trajectory has an energy lower than the design energy and reaches the RF cavity before the design particle. It therefore passes a higher electric field and is able to gain more energy. A particle with an energy higher than the design energy moves on an outer dispersion trajectory. It reaches the RF cavity after the design particle, passes a lower electric field and gains less energy (see fig. 8). This results in an oscillation around the design phase, which is referred to as synchrotron oscillation. These oscillations stabilize the beam in the longitudinal direction.

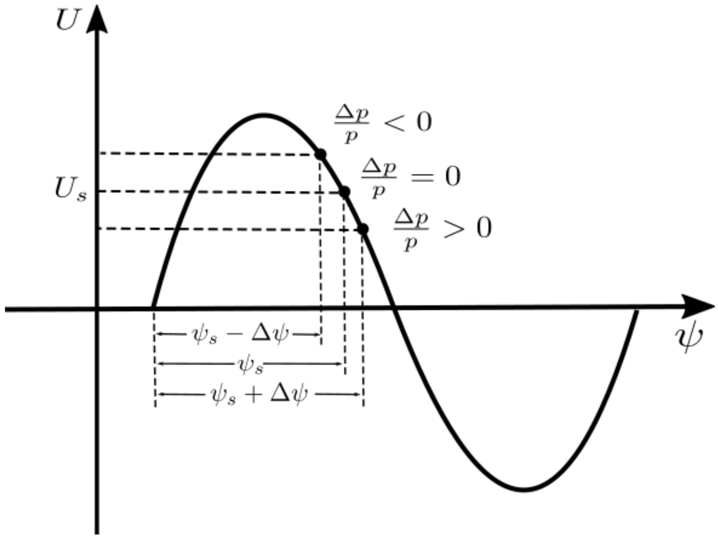

Figure 8: Phase ψ and voltage U of a RF cavity. A design particle passes the cavity at the design phase ψ_s and acquires the exact amount of energy lost via synchrotron radiation. A particle on a dispersion trajectory $\frac{\Delta p}{p} > 0$ passes the RF cavity after the design particle at $\psi_s + \Delta\psi$. It therefore acquires less energy than a design particle. For the same reason, a particle on a dispersion trajectory $\frac{\Delta p}{p} < 0$ acquires more energy than a design particle. The particles of the beam therefore perform synchrotron oscillations around the design phase ψ_s.

Chromaticity The penultimate paragraph described the momentum dependency of the dipole bending angle α or radius ρ for a dipole magnet of given strength B. However, it is not only the dipole strength, but all multipole strengths K_i that show a dependency of the particle momentum. While the momentum dependency of a dipole bending angle leads to dispersion, the momentum dependency of the quadrupole focussing strength causes the so-called chromaticity of an accelerator. A deviation in the quadrupole focussing strength

$$\Delta K_1 = -\frac{e}{p_0^2}\frac{dB_y}{dx}\Delta p = -K_1\frac{\Delta p}{p_0} \tag{15}$$

in linear approximation leads to a shift of the tune

$$\Delta Q_u = \frac{1}{4\pi}\int_{quad}\beta_u(s)\Delta K_1 ds = -\frac{1}{4\pi}\int_{quad}\beta_u(s)K_1 ds\frac{\Delta p}{p_0}. \tag{16}$$

The total tune shift is obtained by summing up all quadrupole contributions, or, equivalently, by integrating over the position-dependent quadrupole strength $K_1(s)$.

$$\Delta Q_u = -\frac{1}{4\pi}\oint\beta_u(s)K_1(s)ds\frac{\Delta p}{p_0} \tag{17}$$

The factor

$$Q' = \frac{dQ}{d(\frac{\Delta p}{p_0})} = \oint \beta(s) K_1(s) ds \tag{18}$$

is called the *natural chromaticity* of the accelerator. As was explained further up in this section, choosing the correct working point is crucial for the performance of an accelerator. However, with the tune depending on the particle energy, there is always the threat of particles running into optical resonances and being lost, thus decreasing the luminosity of the accelerator or causing the beam to become unstable altogether. On the other hand, in a lepton machine there are unavoidable energy fluctuations due to the loss of energy via synchrotron radiation and the gain of energy in RF sections. Thus, in order to avoid a tune shift, the chromaticity must be corrected. This is done by introducing sextupole magnets into the accelerator lattice. The sextupole field has the following form:

$$\frac{e}{p} B_x = K_2 xy \qquad \Rightarrow \qquad \frac{e}{p}\frac{dB_x}{dy} = K_2 x \tag{19}$$

$$\frac{e}{p} B_y = \frac{1}{2} K_2 (x^2 - y^2) \qquad \Rightarrow \qquad \frac{e}{p}\frac{dB_y}{dx} = K_2 x \tag{20}$$

with the normalized sextupole strength K_2. For a given orbit offset in the sextupole, the focussing strength of a sextupole evaluates to:

$$K_{1,sext} = \frac{e}{p}\frac{dB_y}{dx} = K_2\, x. \tag{21}$$

In the horizontal plane, particles move on a dispersion orbit which depends on the relative momentum deviation $x(s) = D_x(s)\frac{\Delta p}{p_0}$, so $K_{1,sext}$ becomes

$$K_{1,sext}(s) = K_2 D(s) \frac{\Delta p}{p_0}. \tag{22}$$

Therefore, sextupoles have their own contribution to the tune shift:

$$\Delta Q_u = \frac{1}{4\pi} \oint \beta_u(s) (K_2 D(s) - K_1(s)) ds \frac{\Delta p}{p_0}. \tag{23}$$

The sextupole strengths K_2 can be used to correct the quadrupole contributions to the tune shift and thus to match the chromaticity to zero. Chromaticity correction is a very important step in accelerator design. In section 5, an approach for chromaticity correction is introduced which uses a so-called *downhill simplex algorithm* in order to numerically optimize the sextupole strengths and to correct the chromaticity of FCC-ee.

Effects of Synchrotron Radiation It has already been mentioned that particles in an accelerator lose energy due to the emission of electromagnetic waves. Synchrotron radiation specifically is the emission of radiation due to acceleration of a particle orthogonal to its momentum vector, for instance by a magnetic dipole field. Due to the relativistic velocities of particles in an accelerator, the radiation is emitted not with the angular distribution of a Hertzian dipole, but symmetrically along a cone with an opening angle defined by the Lorentz factor $\theta \approx \frac{1}{\gamma_L}$ around its momentum vector. The total power emitted via synchrotron radiation is

$$P_s = \frac{e^2 c}{6\pi\epsilon_0} \frac{1}{(m_0 c^2)^4} \frac{E^4}{\rho^2} \tag{24}$$

with e being the electron charge, c the speed of light, ϵ_0 the permeability of vacuum, m_0 the electron mass, ρ the bending radius of the dipole magnet and E the particle energy. The emitted power strongly depends on the particle energy, as well as its mass. Thus, the radiated power is much higher for electrons than for protons or even heavier particles. For that reason, emission of synchrotron radiation is a serious problem in lepton accelerators, while it can often be neglected in hadron machines. Due to the synchrotron power being dependent on the dipole bending radius, dipole fields should be as weak as possible, as otherwise too much energy would be lost via radiation. This explains why a circumference of 80-100 km is necessary for a machine like FCC-ee to work. The emission of synchrotron radiation results in two antagonistic effects which influence the equilibrium emittance in an equal way: radiation damping and quantum excitation:

Radiation Damping: The emission of synchrotron radiation has a damping effect on both the longitudinal and the transverse oscillations. Synchrotron oscillations are damped, because particles with a higher momentum radiate off more energy than particles with a lower momentum. This causes the amplitude of the longitudinal oscillation to decrease. Betatron oscillations are damped, because synchrotron radiation is emitted in the direction of the current particle momentum, which means that the particle loses momentum $\delta\vec{p}$ both in the longitudinal, as well as in the transverse plane, $\delta\vec{p_L}$ and $\delta\vec{p_T}$ respectively. The longitudinal component of the momentum is however quickly restored in the RF cavities, resulting in an overall decrease of the transverse particle momentum.
Both the longitudinal and transverse oscillation amplitude are exponentially damped:

$$A_u(t) = A_{u,0} e^{-a_u t} \tag{25}$$

with a_u being the damping constants and u in this case $\in \{x, y, z\}$. The damping constants can be expressed in terms of the *damping partition numbers* J_u:

$$a_u = \frac{r_e}{3} (\frac{E_0}{mc^2})^3 \frac{c}{L_0} \mathcal{I}_2 J_u \tag{26}$$

with r_e being the classical electron radius, L_0 the length of the design orbit and $\mathcal{I}_2$ the second so-called *synchrotron radiation integral*, which has the form

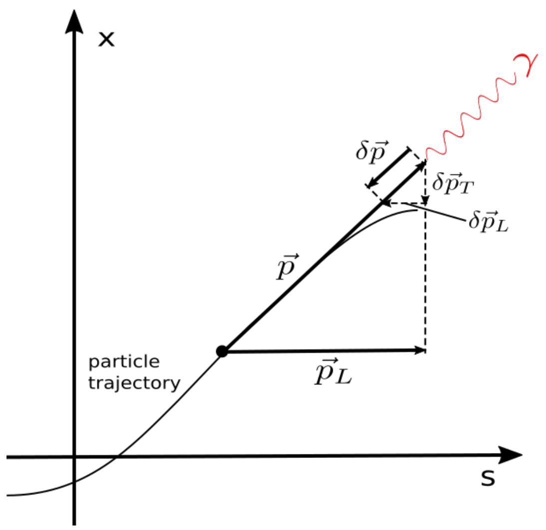

Figure 9: Damping of betatron oscillations due to the emission of a photon. The photon is emitted in the direction of the local particle momentum $\vec{p}$ and carries the momentum $\delta\vec{p}$. The new electron momentum is $\vec{p}^* = \vec{p} - \delta\vec{p}$. However, the longitudinal component $\delta\vec{p}_L$ is restored in the RF cavities, resulting in an overall decrease of the transverse particle momentum.

$$\mathcal{I}_2 = \oint \frac{1}{\rho^2}\mathrm{d}x = \sum_i \frac{l_i}{\rho_i^2}. \tag{27}$$

The synchrotron radiation integrals will be explained in detail later in this section. The damping partition numbers themselves can in turn be expressed in terms of the synchrotron radiation integrals. The important *Robinson Theorem* states, that the sum of the three damping partition numbers is invariant:

$$J_x + J_y + J_z = 4 \tag{28}$$

An accelerator only consisting of separated dipoles and quadrupoles always has the damping partition numbers $J_x = 1, J_y = 1, J_z = 2$. This is called the *natural damping distribution*. Effects like betatron coupling, which cause the transfer of energy from one plane to another, result in a deviation of the damping partition numbers from these natural values.

Quantum Excitation: Radiation damping decreases the amplitude of both synchrotron and betatron oscillations. If this were the only effect synchrotron radiation had on the particle beam, the amplitude of the oscillation would damp down to virtually zero within a few damping times and all particles within the beam would move on the design orbit. This corresponds to volume of zero in phase space (respectively the volume a Fermi gas in its ground state has in phase space). This would be the case if electromagnetic waves were emitted continuously. However, electromagnetic energy is emitted stochastically via photons. The discontinuous loss of an often significant amount of energy means that the particle suddenly has an offset regarding its new dispersion orbit, which depends on its energy deviation $x_{\Delta E} = D_x \frac{\delta E}{E_0}$. This offset is responsible for the start of a betatron oscillation around the new orbit. Therefore, synchrotron radiation not only damps down oscillation amplitudes, but also induces new oscillations. These two effects lead to a non-zero phase space volume of the beam, the so-called *equilibrium emittance.*

Emittance According to equation (6), the amplitude of the particle oscillation is defined by both the beta function and a factor called the beam emittance. While the beta function oscillates depending on the focussing properties of the magnet structure, the emittance is a constant of motion. It represents the volume in the six-dimensional phase space the beam occupies. This way, it is a measure of beam size as well as of beam divergence. A particle beam is an ensemble of fermions. Thus, it has a certain six-dimensional phase space density $\Psi(x, y, z, p_x, p_y, p_z)$, as well as a phase space current $\overrightarrow{j} = (\Psi\dot{x}, \Psi\dot{y}, \Psi\dot{z}, \Psi\dot{p_x}, \Psi\dot{p_y}, \Psi\dot{p_z})$. Liouville's Theorem states, that as long as a particle density distribution is under the influence of conservative forces, it behaves like an incompressible fluid. This means, it has to follow a continuity equation

$$\frac{\partial \Psi}{\partial \tau} + \nabla \overrightarrow{j} = 0. \tag{29}$$

With the assumptions that $\overrightarrow{r}$ and $\overrightarrow{p}$ are independent phase space coordinates, that the derivative of the space vector $\overrightarrow{\dot{r}}$ does not depend on spatial coordinates and that the magnetic field $\overrightarrow{B}$ does not depend on particle momentum, this equation becomes

$$\frac{\partial \Psi}{\partial \tau} + (\nabla_r \Psi)\overrightarrow{\dot{r}} + (\nabla_p \Psi)\overrightarrow{\dot{p}} = \frac{d\Psi}{d\tau} = 0. \tag{30}$$

Equation (30) describes Liouville's Theorem for the specific case of a particle beam within a magnetic focussing field and is proof of the phase space volume or emittance being constant, as long as the beam is guided only by conservative forces. This statement, however, is only true for a hadron storage ring. In an electron storage ring, the beam's initial emittance is not conserved at all. On the contrary, two antagonistic, non-conservative effects of synchrotron radiation dominate the evolution of the beam emittance in time: radiation damping and quantum excitation.

These effects result in an equilibrium emittance which, for constant particle momentum, is solely dependent on the lattice structure of the storage ring. As long as these two effects are in equilibrium, the beam emittance is again a constant of motion. In a linear environment, i.e. without sextupoles and betatron coupling, the six-dimensional phase space can be split into three two-dimensional phase spaces. For each of the two transverse planes, a constant of motion can be obtained from the equations of motion, called the Courant-Snyder-Invariant E_u of the respective plane:

$$E_u = \gamma_u u^2 + 2\alpha_u u u' + \beta_u u'^2 \tag{31}$$

with $u \in \{x, y\}$. This invariant represents a single particle travelling on a phase space ellipse determined by the Twiss parameters $\beta_u, \alpha_u(s) := -\frac{\beta_u'(s)}{2}$ and $\gamma_u(s) := \frac{1+\alpha_u^2(s)}{\beta_u(s)}$. Liouville's Theorem states that every particle starting on a phase space ellipse will stay on it. Therefore, it is sufficient to find a suitable ellipse, as every particle with a smaller betatron amplitude will stay within that ellipse. The equilibrium emittance can be obtained by choosing a particle with a momentum deviation $\frac{\Delta p}{p} = 1$. The orbit of such a particle is described by the dispersion function. The Courant-Snyder-Invariant of this particle is called the $\mathcal{H}$ function [7]

$$\mathcal{H}_u = \gamma_u D_u^2 + 2\alpha_u D_u D_u' + \beta_u D_u'^2. \tag{32}$$

In this function, D_u is the dispersion and D_u' is the derivative of the dispersion. $\mathcal{H}_u$ therefore contains the entire information of the lattice structure of the accelerator. The equilibrium emittance can now be calculated as follows:

$$\epsilon_u = \frac{55}{32\sqrt{2}} \frac{\hbar}{m_e c} \frac{\gamma_L^2}{J_u} \frac{\oint \frac{\mathcal{H}_u}{|\rho^3|} \mathrm{d}x}{\oint \frac{1}{\rho^2} \mathrm{d}x} \tag{33}$$

with the Lorentz gamma factor γ_L, the damping partition number J_u and the dipole bending radius ρ.

In an ideal storage ring, there is no vertical dispersion, so according to this formula, the vertical emittance is zero. In reality, the vertical emittance is not zero, but damps down to a certain minimum. This can be explained as follows: particles in the beam move on the vertical design orbit. There are no initial betatron oscillations in the vertical plane, so synchrotron radiation is emitted into an opening angle depending on the Lorentz factor $\theta = \frac{1}{\gamma_L}$ along the longitudinal axis. The small transverse momentum of these photons in turn induces small vertical betatron oscillations, which define the theoretical minimum of the vertical emittance.

In a real storage ring however, magnet alignment errors and betatron coupling introduce dispersion in the vertical plane. The theoretical emittance limit is therefore virtually unreachable and it is customary for storage rings to operate with a vertical emittance in the order of 1 % of the horizontal emittance.

Synchrotron Radiation Integrals In the previous paragraphs, several parameters were introduced which can be derived from synchrotron radiation integrals. The synchrotron radiation integrals describe the entire dynamics of a lepton accelerator, albeit only in linear approximation and far from any betatron coupling resonances. They are calculated as follows:

$$\mathcal{I}_1 = \oint \frac{D_x}{\rho}\mathrm{d}s = \sum_i \frac{l_i}{\rho_i} < D_x >_i \tag{34}$$

$$\mathcal{I}_2 = \oint \frac{1}{\rho^2}\mathrm{d}s = \sum_i \frac{l_i}{\rho_i^2} \tag{35}$$

$$\mathcal{I}_3 = \oint |\frac{1}{\rho^3}|\mathrm{d}s = \sum_i \frac{l_i}{|\rho_i^3|} \tag{36}$$

$$\mathcal{I}_{4u} = \oint \frac{(1-2n)D_u}{\rho_u^3}\mathrm{d}s = \sum_i [\frac{l_i}{\rho_{u,i}^3} < D_u >_i -2l_i < \frac{nD_u}{\rho_u^3} >_i] \tag{37}$$

$$\mathcal{I}_{5u} = \oint \frac{\mathcal{H}_\mathrm{u}}{|\rho^3|}\mathrm{d}s = \sum_i \frac{l_i}{|\rho_i^3|} < \mathcal{H}_\mathrm{u} >_i \tag{38}$$

with $u \in \{x, y\}$. These integrals contain all the information of the lattice structure of an electron storage ring. Parameters that can be derived from them include

- the momentum compaction factor α_c, which is the proportionality factor between relative orbit length and relative momentum deviation

$$\alpha_c = \frac{\frac{\Delta L}{L}}{\frac{\Delta p}{p_0}}. \tag{39}$$

  It can be derived from $\mathcal{I}_1$ via

$$\alpha_c = \frac{\mathcal{I}_1}{L}. \tag{40}$$

- the total energy loss per turn

$$U_0 = [\frac{2}{3}\mathrm{r_e}\gamma_\mathrm{L}^4\mathrm{m_e c^2}]\mathcal{I}_2, \tag{41}$$

- the damping partition numbers

$$J_x = 1 - \frac{\mathcal{I}_{4x}}{\mathcal{I}_2} \tag{42}$$

$$J_y = 1 - \frac{\mathcal{I}_{4y}}{\mathcal{I}_2} \tag{43}$$

$$J_z = 2 + \frac{\mathcal{I}_{4x} + \mathcal{I}_{4y}}{\mathcal{I}_2}, \tag{44}$$

- and, finally, the equilibrium beam emittances, which now have the form

$$\epsilon_u = C_q \frac{\gamma_L^2}{J_x}\frac{\mathcal{I}_{5u}}{\mathcal{I}_2}, \tag{45}$$

where $C_q = \frac{55}{32\sqrt{3}}\frac{\hbar}{\mathrm{m_e c}} \approx 3,832 \cdot 10^{-13}$.

Betatron Coupling The formula for the equilibrium emittances given above is correct only, if the particle motion in both planes can be calculated independently. If this is not the case, coupled equations of motion have to be introduced. In the case of weak coupling (flat beam case), a perturbative approximation can be made. In this approximation, the horizontal equation of motion is unchanged, while the vertical equation of motion describes an oscillation driven by the horizontal motion [8].

$$x'' + K_x x = 0, \qquad K_x = \frac{e}{p}\frac{\partial B_y}{\partial x} + \frac{1}{\rho^2} \tag{46}$$

$$y'' + K_y y = -\tilde{K}_1 x, \;\; K_y = -\frac{e}{p}\frac{\partial B_y}{\partial x}, \;\; \tilde{K}_1 = \frac{e}{p}\frac{\partial B_x}{\partial x}. \tag{47}$$

In the case of weak coupling, the horizontal equilibrium emittance is unchanged. The vertical emittance due to coupling is in linear approximation:

$$\epsilon_y = \frac{C_q \gamma_L^2}{16 J_y \mathcal{I}_2} \oint ds \frac{\mathcal{H}}{|\rho^3|}[\sum_{\pm} \frac{|Q_{\pm}(s)|^2}{\sin^2(\pi \Delta \mathrm{Q}_{\pm})} + 2\mathrm{Re}\frac{\mathrm{Q}_+(\mathrm{s})\mathrm{Q}_-(\mathrm{s})}{\sin(\pi\Delta\mathrm{Q}_+)\sin(\pi\Delta\mathrm{Q}_-)}], \tag{48}$$

with

$$Q_{\pm}(s) = \oint dz \tilde{K}_1(z)\sqrt{\beta_x\beta_y} e^{i[(\Psi_x(s)\pm\Psi_y(s))-(\Psi_x(z)\pm\Psi_y(z))+\pi(Q_x\pm Q_y)]}. \tag{49}$$

In these formulae, $Q_{\pm}$ is called the coupling integral which effectively defines the strength of the betatron coupling. $\tilde{K}_1(z)$ is the quadrupole field gradient $\frac{dB_x}{dx}$ or $\frac{dB_y}{dy}$, Ψ is the horizontal or vertical phase advance, Q is the horizontal or vertical tune and $\Delta Q_+ = Q_x + Q_y$ and $\Delta Q_- = Q_x - Q_y$ are the sum and difference coupling resonance, respectively. Common sources of coupling are for example tilted quadrupole or misaligned sextupole magnets.

The accelerator code MAD-X The standard tool for designing accelerators and lattices at CERN is called *Methodical Accelerator Design*, or *MAD*. It was optimized specifically for high-energy synchrotrons and particle colliders. The current version of *MAD*, *MAD-X* was released in 2002 and is maintained by the *MAD* group at CERN. The *MAD* user's guide can be found on the *MAD* homepage [2]. *MAD-X* was used for most of the work done in this thesis, as well as for all the accelerator lattice designs on which that work is based. Once a specific lattice is implemented, *MAD-X* finds the closed orbit of the machine and calculates the optical functions, as well as machine parameters such as: tunes, horizontal and vertical chromaticities, the synchrotron radiation integrals, damping partition numbers and equilibrium beam emittances. In addition to that, several numerical matching and optimization routines exist in order to optimize every element of the machine.

3 Dipole Tapering Procedures

A charged particle moving in a magnetic field constantly loses energy due to synchrotron radiation. In particle accelerators, the radiated synchrotron power P_γ within a dipole field is quantitatively described by

$$P_\gamma = \frac{2}{3} r_e \gamma_L^4 m_e \frac{l}{\rho^2} \tag{50}$$

where l is the length of the dipole and ρ is its bending radius. This constant loss of energy in combination with the energy gain in radiofrequency (RF) cavities leads to a periodic deviation of the local particle energy from the design energy. As the bending angle α of a dipole depends on the local particle energy

$$\frac{\alpha}{l} = \frac{e}{E_{local}} cB, \tag{51}$$

particles with different energies are forced onto dispersion trajectories, causing the so-called sawtooth effect of the orbit. Roughly spoken, for a constant magnetic dipole field B the bending angle α is smaller for energies higher than the design energy, causing the particles to drift outward, and higher for energies lower than the design energy, causing the particles to drift inward.

The exact orbit of a particle can be obtained by solving Hill's equation (see section 2) for the particular accelerator lattice. However, as it is rarely necessary to solve the complete equation, a transformation matrix formalism was developed. In this formalism, the orbit offset x, the slope x' and the local energy deviation $\frac{\Delta E}{E_0}$ form a three vector and each accelerator element is represented by a $3 * 3$ transformation matrix. By transforming a set of initial conditions $\vec{x}_i$ element by element, the complete orbit throughout the accelerator can be constructed. The matrix representing a dipole bending magnet is:

$$\begin{pmatrix} x(s) \\ x'(s) \\ \frac{\Delta E}{E_0} \end{pmatrix} = \begin{pmatrix} cos(\alpha) & \rho sin(\alpha) & \rho(1 - cos(\alpha)) \\ -\frac{1}{\rho} sin(\alpha) & cos(\alpha) & sin(\alpha) \\ 0 & 0 & 1 \end{pmatrix} \begin{pmatrix} x_i(s) \\ x_i'(s) \\ \frac{\Delta E}{E_0} \end{pmatrix} \tag{52}$$

The contribution of a local energy deviation within a dipole to the orbit offset and slope evaluates to:

$$x(s) = -\rho(1 - cos\alpha) \frac{\Delta E}{E_0} \quad \text{and} \quad x'(s) = -sin\alpha \frac{\Delta E}{E_0}. \tag{53}$$

This orbit offset due to local energy deviations is called sawtooth effect. It is the major contribution to orbit offsets in high-energy lepton machines, causing the orbit in FCC-ee

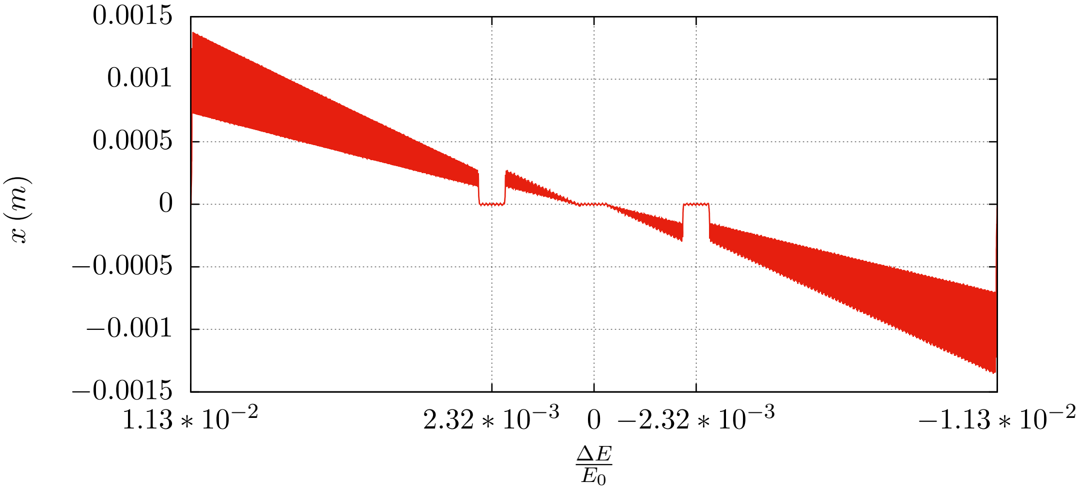

Figure 10: orbit offset $x(s)$ depending on the local energy deviation $\frac{\Delta E}{E_0}$ of a FCC-ee lattice at 175 GeV before tapering

to reach offsets of up to 1.4 mm at its peak energy of 175 GeV. Schematically, the effect of a local energy deviation on the orbit offset is shown in figure 11.

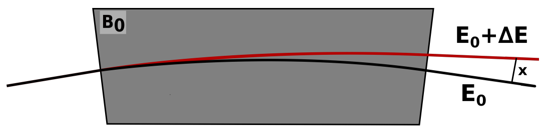

Figure 11: Dipole before tapering. A particle with an energy deviation ΔE is forced onto a dispersion trajectory.

If a particle passes a quadrupole at such a large offset, it "sees" an additional, perturbing dipole field. In the same way, when the particle passes a sextupole at a large offset, this feed-down effect leads to an additional quadrupole field. While perturbing dipole fields cause orbit and dispersion distortions, perturbing quadrupole fields lead to distortions of the beam optics. Both in turn lead to an increase of the beam emittance. By *tapering* a dipole magnet, where tapering means adjusting its field strength to the local beam energy, the sawtooth effect and thus negative effects on emittance, chromaticity, etc. can be avoided.

Individual Tapering Strategies

In a lepton storage ring a non-constant, periodic oscillation of the beam energy leads to both orbit and optics distortions, as all lattice elements (dipoles, quadrupoles, sextupoles,...) are designed for the nominal beam energy. The ideal solution to this problem would be to adjust the strength of each lattice element to the local beam energy. This

way, the closed orbit would be the design orbit, there would be zero orbit offset and the limiting factor of the beam size would be the equilibrium emittance. In a real machine, however, this would mean a tremendous effort both logistically and financially, as in that case each magnet would need its own power supply. For that reason, the tapering studies conducted in this thesis focus primarily on an optimization of dipole fields and thus on the elimination of the sawtooth orbit.
Different tapering strategies will show, how much of an orbit decrease is ideally possible and what effect this decrease will have on the beam optics. Afterwards, the focus will shift from what is possible to what is necessary. At a certain point, a further orbit reduction is unnecessary, as other factors like quadrupole misalignments become the dominant influence on the orbit. A compromise has to be found between an optimization of the beam optics and cost efficiency. For that reason, so-called *averaged tapering strategies* will be introduced, where the strength of every dipole is not adjusted individually to the local beam energy, but families of dipoles are assigned an averaged tapered strength.

Tapering studies have been conducted with both the 12-fold (see figure 2) and the racetrack (see figure 3) layout at particle energies of 45.5 GeV, 120 GeV and 175 GeV, as well as with 12, 6, 4 and 2 RF sections in the 12-fold layout, respectively 8, 6, 4 and 2 RF sections in the racetrack layout. The reason behind studies with varying numbers of RF cavity straight sections is that the implementation of RF cavities into an accelerator is expensive. It is therefore better from a financial point of view to implement as few as possible. This on the other hand means that the energy deviations in between these sections become larger as the distance in between RF cavities grows. The power of the RF cavities needs to be increased accordingly. The sawtooth effect and thus the particle offset increases as well. In order to keep both the financial cost of implementing RF sections and the orbit offset low, dipole tapering can be introduced.

The sawtooth effect increases with increasing energy and with a decreasing number of RF sections. The so-called worst case scenario is therefore the racetrack layout at an energy of 175 GeV and with RF cavities installed in only two straight sections. Here, orbit offsets reach amplitudes as high as 1.4 mm (see figure 12). The feed-down effect of particles passing quadrupole and sextupole magnets at this offset causes significant optics distortions. This lattice layout will therefore be the primal example on which different tapering strategies will be tested. The tapering strategies conducted in this thesis can be divided into two sub-strategies:

- dipole tapering using additional magnets after each dipole and
- dipole tapering by adjusting the strength of the dipole itself.

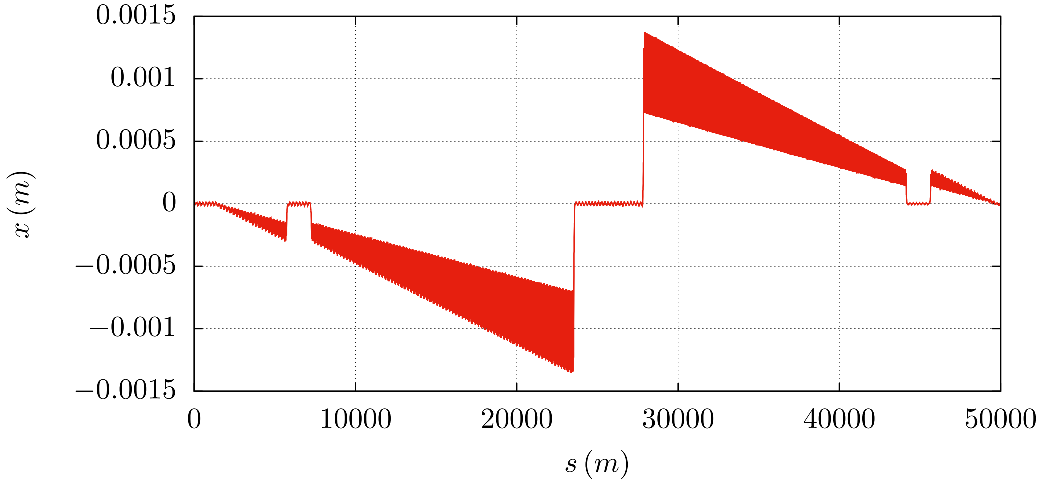

Figure 12: Sawtooth trajectory of a particle with an energy of 175 GeV in the racetrack layout with 2 RF sections. This is the most extreme case with the orbit reaching an offset of approximately 1.4 mm. As the dispersion is zero in the straight sections, no sawtooth effect is observed there.

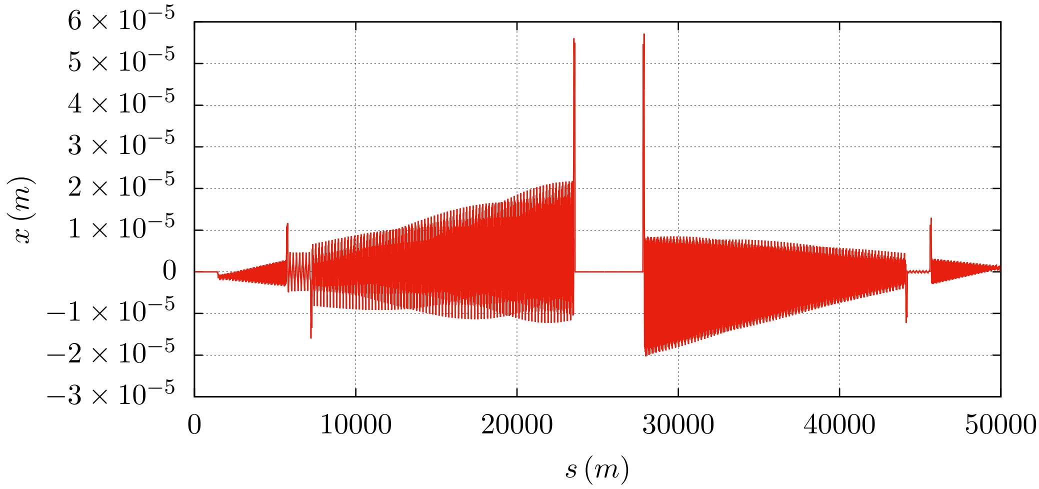

Figure 13: After the implementation of tapering magnets, the orbit decreases to approximately $2.5 * 10^{-5}$ m. The peaks in the orbit are caused by quadrupoles in the dispersion suppressors, which are used to match the dispersion in the straight sections to zero.

Dipole Tapering with Additional Magnets

This strategy has the advantage that all dipole magnets can be powered by the same power source, as they are operated at the same strength. Only individually powered dipole correctors have to be installed in the machine. They however have to be included into the design anyway, as they are necessary for orbit correction.
These additional tapering magnets after each dipole are adjusted in such a way that the sum of the energy dependent dipole bending angle $\alpha_{Dipole}(\Delta E)$ and the bending angle of the tapering dipole field α_{Local} is once again α_0. With this assumption, the bending angle of the local dipole field evaluates to:

$$\alpha_{Dipole}(\Delta E) = \alpha_0(1 - \frac{\Delta E}{E_0}) \tag{54}$$

$$\alpha_{Local} = \alpha_0 \frac{\Delta E}{E_0} \tag{55}$$

This method will be referenced to as the *bending angle method.* Figure 14 shows the effects of the tapering magnet after the dipole.

Using this tapering strategy, the maximum orbit offset decreases to about $20\mu m$, which is an improvement of about a factor 70 (see figure 13). However, the plot also shows a certain level of inhomogeneity of the orbit, as well as some "peaks", where the orbit reaches offsets of up to $5.5 * 10^{-5}$ m. These peaks originate from the dispersion suppressor sections in the lattice.
Dispersion suppressors are sections in the accelerator lattice that are installed between the arcs and the straight sections. These are used to decrease the dispersion function from its default oscillating value in the arcs to zero in the straight sections. This is necessary, as dispersion at the interaction point would lead to an increased effective beam size and a smaller luminosity. Furthermore, the RF cavities used for acceleration couple the longitudinal and transverse plane in the presence of dispersion, leading to additional coupling resonances and potential beam instabilities.
The orbit irregularities as well as the peaks lead to the conclusion, that the method used above to calculate the value of the tapering bending angle is not the optimal setting of the tapering magnet strengths. This makes sense, because completing the bending angle for

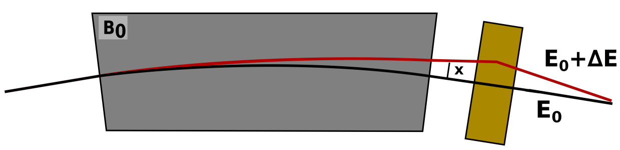

Figure 14: Tapering with an additional magnet after the dipole. A particle with an energy deviation ΔE is now kicked towards the design orbit.

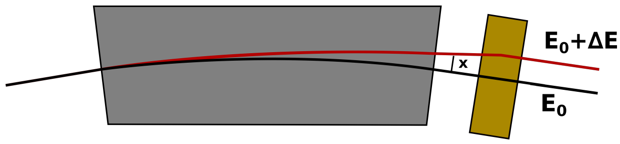

Figure 15: Dipole tapering strategy according to the bending angle method. After the tapering magnet, the already created offset still remains.

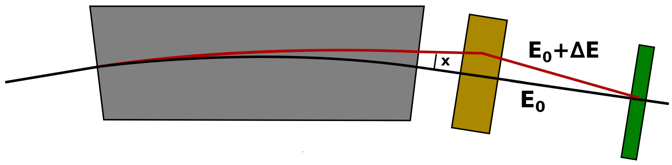

Figure 16: Dipole tapering strategy of optimising the tapering magnet strength numerically. The optimization constraint matched the orbit to zero at the BPM (green), which was located infront of the next dipole.

the respective energy does not correct the offset already created (see figure 15).
To fix this, the strengths of the tapering magnets were optimized numerically. In order to do so, beam position monitors (BPMs) were installed in front of every dipole and the tapering magnet strength was optimized in such a way that the orbit was zero at those BPMs. In the FCC-ee racetrack layout, an algorithm using 6592 tapering magnets and beam position monitors was used. The result is shown in figure 17.
Although the maximum offset does not decrease any further, the orbit looks smoother after the numerical optimization and there are no more offset peaks in the dispersion suppressors. In figures 13 and 17 it can be seen that tapering strategies involving tapering magnets after each dipole lead to an orbit decrease of approximately two orders of magnitude. This is true for both lattice layouts as well as for every setting of the beam energy and number of RF sections. Detailed plots for every parameter setting can be found in the appendix.
In order to answer the questions as to why the orbit decreases by two orders of magnitude respectively why it does not decrease any further, one has to look more closely at how the sawtooth effect is created. Using the transformation matrix method and starting from an ideal orbit, i.e. $x_i = 0$, $x_i' = 0$ and $\Delta E = E_{local} - E_0$, one can calculate the orbit offset arising within a dipole magnet at E_{local} due to the particle gradually drifting onto a dispersion trajectory.

$$x = -\rho(1 - cos(\alpha))\frac{\Delta E}{E_0} \tag{56}$$

$$x' = -sin(\alpha)\frac{\Delta E}{E_0} \tag{57}$$

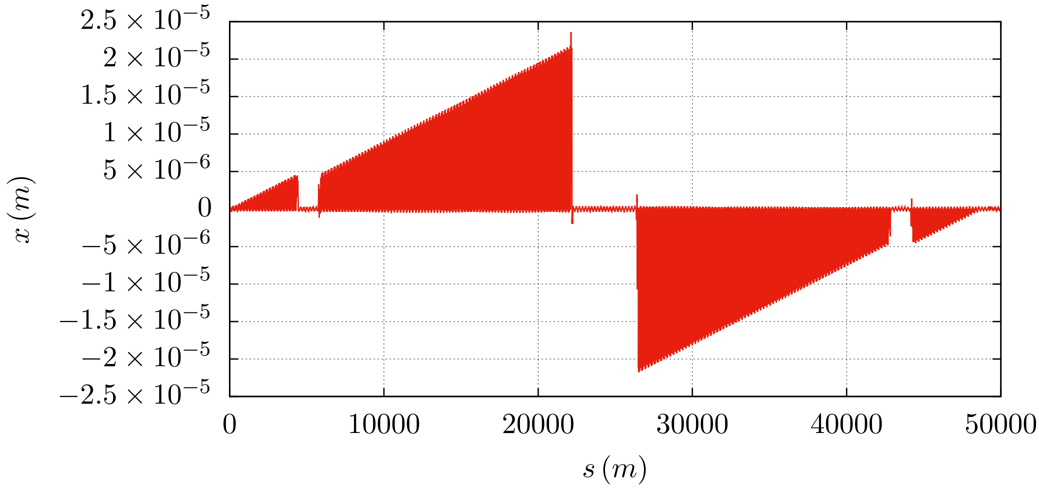

Figure 17: Orbit after a numerical optimization of the tapering magnet strengths. Although the maximum offset does not decrease any further, the orbit looks smoother and more regular. Also, there are no more orbit peaks in dispersion suppressor sections.

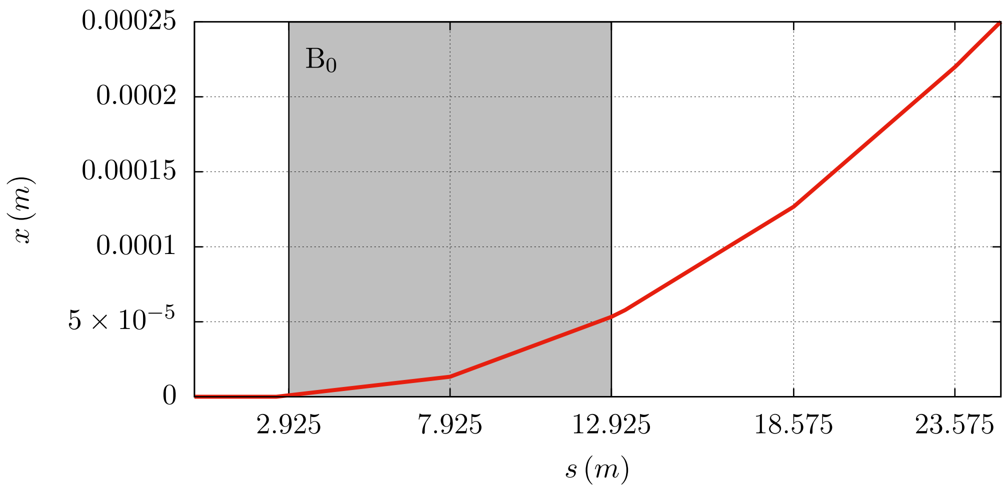

Figure 18: Orbit offset arising within a dipole field B_0 due to a local beam energy deviation $\Delta E = E_{local} - E_0$. Using the maximum value of ΔE in the FCC-ee racetrack layout at 175 GeV, x evaluates to approximately $5.3 * 10^{-5}$ m.

The maximum value of ΔE can be calculated using the total energy loss per turn, $\Delta E_{max} = \frac{U_0}{4}$. Therefore, in the FCC-ee racetrack lattice layout at an energy of 175 GeV, ΔE_{max} evaluates to 1971.82 MeV. Thus,

$$x_{max} = 5.367 * 10^{-5}\,\mathrm{m} \quad \text{and} \quad \mathrm{x'_{max}} = 1.0739 * 10^{-5}, \tag{58}$$

which can also be seen in figure 18. Using the tapering strategy with additional magnets, this orbit offset is corrected after each dipole with the bending angle method. This adaption of the bending angle to the local beam energy however does not correct the offset already created within the dipole magnet. If the tapering magnet strengths are however not adjusted according to the bending angle method, but are instead set by a numerical orbit optimization algorithm, the tapering magnets actively correct the "intrinsic" offset created within the dipoles, thus smoothing out and further improving the orbit. However, even with the numerical optimization, the tapered orbit showed no significant further decrease, making a strong argument that in the case of tapering using additional magnets, an orbit decrease of approximately two orders of magnitude is indeed the best that can be done.

An additional source of orbit disturbances are deflections due to the beam passing quadrupoles off-center. In thin-lens approximation, which is a good approximation for the quadrupoles in FCC-ee, these deflections evaluate to

$$x'_{quad} \approx x l_{quad} K_1 \approx 1 * 10^{-6} \tag{59}$$

with the orbit offset x, the length of the quadrupole l_{quad} and its strength K_1. They are an order of magnitude smaller than the deflections within dipoles due to local energy deviations and therefore only have a negligible influence. They are not the reason why the orbit cannot be reduced any further with the tapering magnet strategy. In fact, the tapering magnets can be set in such a way, that the orbit is zero at every quadrupole, thus eliminating their influence altogether. The resulting orbit can be seen in figure 19 and is a factor of 2 larger than the orbit after the numerical optimization. A detailed view of this plot is very useful, as with the quadrupole influence removed, the contribution of each dipole to the orbit offset becomes apparent and can be easily checked analytically using the transformation matrix method. In agreement with the result in eq. (58), the orbit reaches values of up to $\pm 5.4 * 10^{-5}\,m$, at the highest and lowest local energy, respectively.

Dipole Tapering by Adjusting the Strength of the Dipole

Dipole tapering using additional tapering magnets decreases the closed orbit distortion by approximately two orders of magnitude. To improve the orbit further, the dipole magnets themselves have to be adjusted to the local beam energy. This method, although easy in theory, bears a variety of problems in terms of simulation. To understand the following,

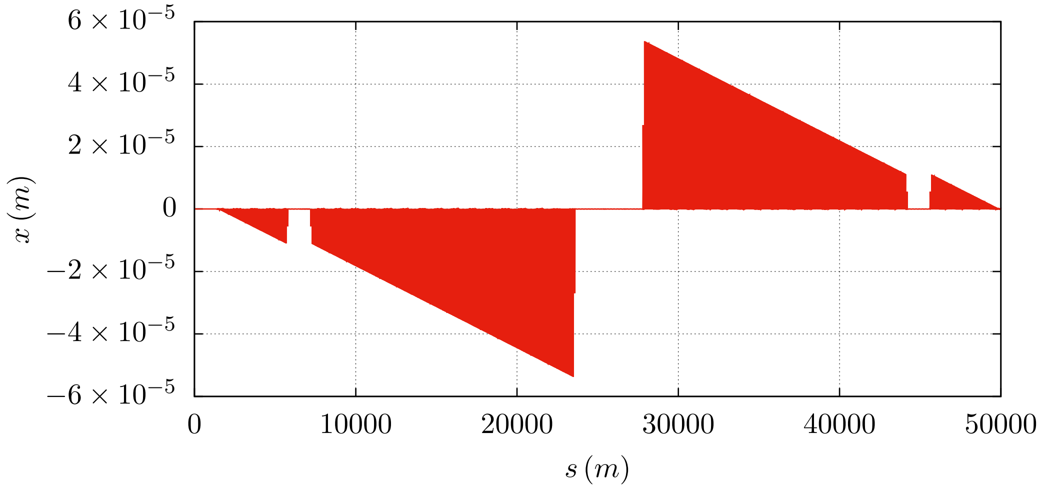

Figure 19: Orbit of FCC-ee at an energy of 175 GeV and tapering magnets set in such a way that the offset is zero at each quadrupole. This way, the influence of every single dipole on the orbit can be investigated.

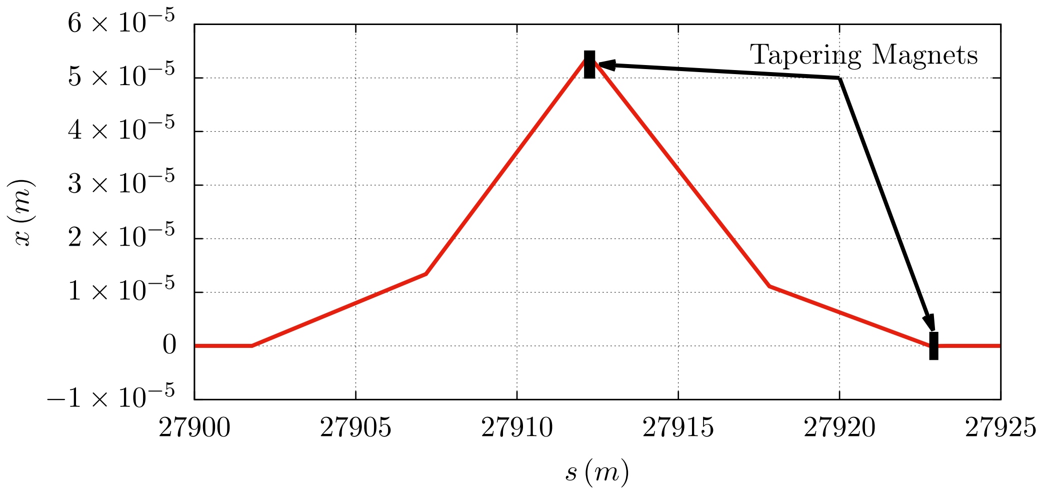

Figure 20: Detailed view of the orbit in an arc cell with maximum positive energy deviation. The plot shows the contribution of the first dipole magnet in the cell to the orbit offset. Tapering magnets after each dipole are set in such a way, that the orbit is zero at every quadrupole. The maximum offset is in agreement with the offset calculated in eq. (58).

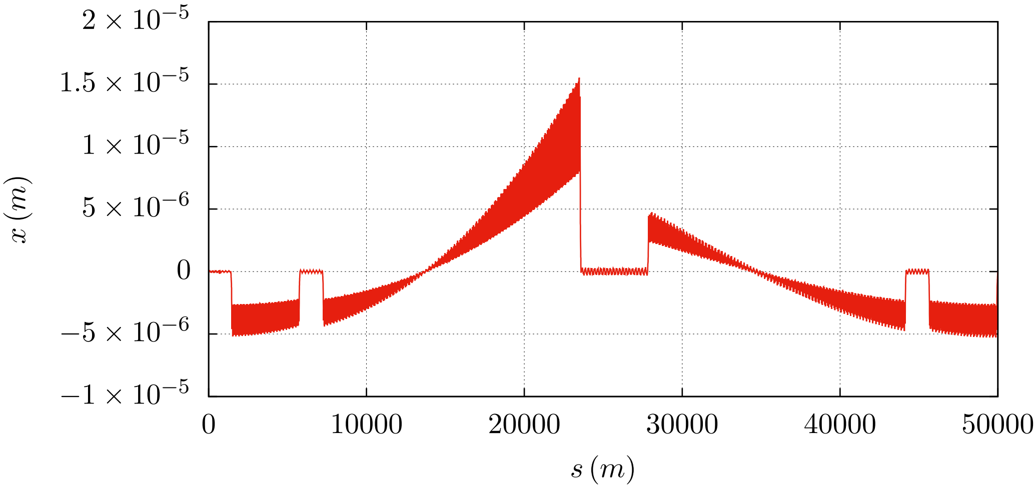

Figure 21: Orbit after adjusting the dipole strengths to the local beam energy according to the bending angle method

one has to differentiate between the design orbit and the closed orbit. The design orbit is the path of a charged particle with design momentum through idealized magnets without fringe fields. It is in a sense the ideal orbit, to which the real closed orbit of a particle is in reference to. A particle with zero orbit offset moves on the design orbit. In *MAD-X*, the design orbit is defined by the dipole magnets. A change in the dipole strengths affects the closed orbit as well as the design orbit. As the design orbit serves as the frame of reference for the closed orbit, only the change of the closed orbit relative to the new design orbit would be observed. A way to change the dipole magnet strengths, but keep the original design orbit, is to introduce tapering corrections to the dipole field via constant dipole errors. This, however, proves to be very time-consuming in simulation. For this reason, the tapering studies in this case were conducted primarily for the "worst-case scenario" of an energy of 175 GeV and two RF sections.

The bending angle method is still valid, the only difference is that the correction to the bending angle α_{Local} is now assigned directly to the dipole as a constant dipole error rather than to an additional tapering magnet after the dipole. Figure 21 shows the orbit after the application of this method.

Compared to the tapering strategy with additional magnets, the maximum orbit offset does not decrease significantly. However, the overall behaviour of the orbit changes a great deal. The "oscillations" of the orbit, which were caused by the alternating deflections of dipoles and tapering magnets, no longer occur. Furthermore, the orbit now shows some sort of quadratic dependency, indicating an influence of quadrupole magnets.

A detailed view of a small segment of an arc section (figure 22) shows that with the decreased influence of the dipoles, the orbit is now predominantly determined by the

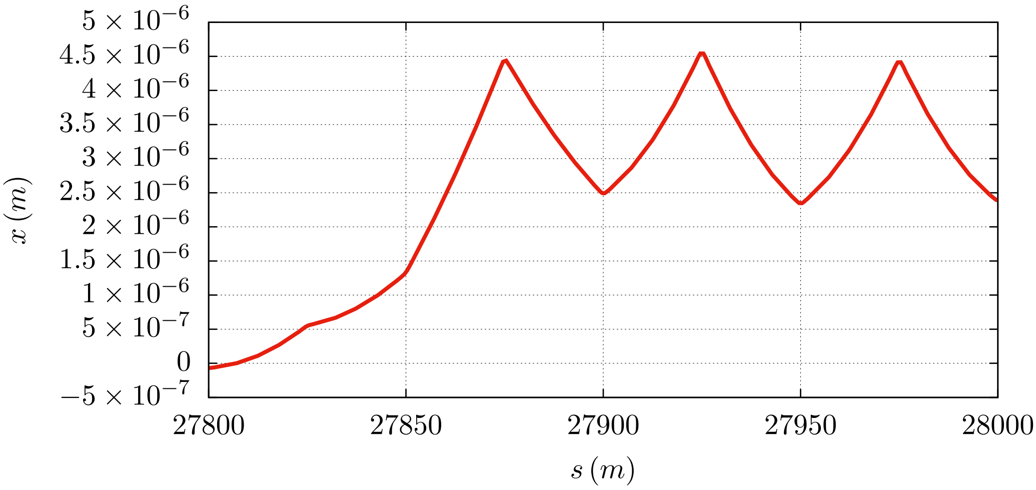

Figure 22: Detailed view of a small segment of 200 m of an arc section after a straight section. The influence of the dipole magnets on the orbit is clearly diminished, making apparent a now dominant influence of quadrupole magnets.

quadrupoles. Calculations show that, while orbit deflections of dipoles have decreased approximately thee orders of magnitude from $x' = 10^{-5}$ to approximately $6 * 10^{-8}$, orbit deflections of quadrupole magnets are

$$x'_{QD} = 3.23 * 10^{-7} \tag{60}$$

$$x'_{QF} = -7.938 * 10^{-7} \tag{61}$$

for defocussing and focussing quadrupoles respectively. As there are four dipoles in between each focussing quadrupole, dipole and quadrupole influences are in the same order of magnitude and there is a fragile equilibrium between the influence of defocussing quadrupoles and dipoles on one hand and focussing quadrupoles on the other hand.

However, as was stated earlier, setting the dipole errors according to the bending angle method is not perfect. The dipoles not being at their optimal value is the reason why they are still responsible for tiny deflections, which are then amplified by the quadrupoles. The quadrupole field strengths and thus their deflections depend on the orbit offset, which therefore shows a quadratic growth in the arc sections. Therefore, a numerical optimization of the dipole error values is necessary, which was done in the following way:

The dipoles were split into three parts and two "virtual" dipole magnets of zero length were put in between. These two dipoles were used to match x and x' after each dipole to zero. After that, those two field strengths were averaged and implemented as dipole error for the respective dipole. Due to the transition from orbit corrector strength to dipole error, these values were still not optimal, but they were a better approximation to the optimal value. They were used as new initial conditions in an iterative process resulting

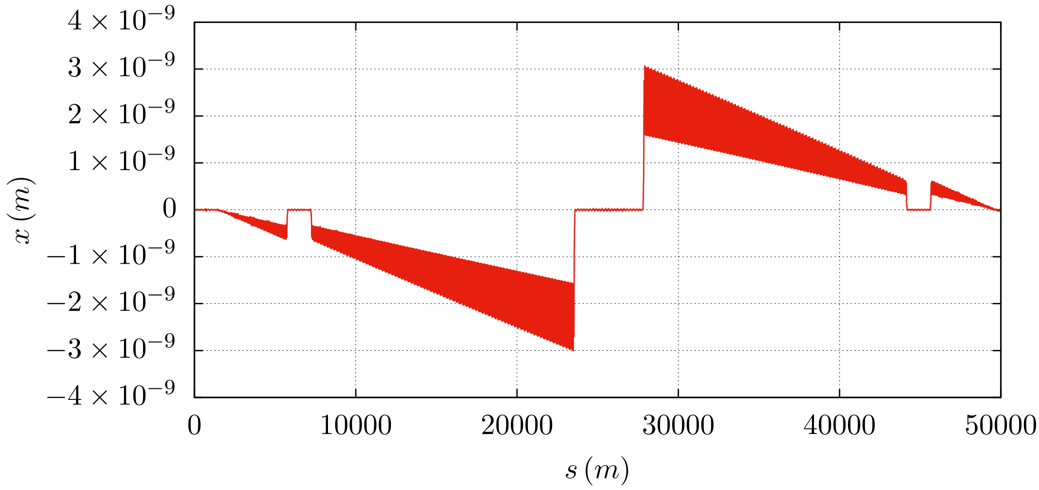

Figure 23: Orbit offset after an iterative numerical optimization of the dipole strength values. The orbit decreases to approximately $3 * 10^{-9}$ m, an improvement of about four orders of magnitude compared to the tapering strategies with additional magnets and setting dipole strengths according to the bending angle method.

in the optimal dipole strengths.

Using this method, the orbit offset can be decreased to about $3 * 10^{-9}$ m, which is an improvement of a about six orders of magnitude compared to the orbit without tapering and an improvement of about four orders of magnitude compared to the orbit with tapering magnets. At an energy of 175 GeV, this orbit offset is in the same order of magnitude as the equilibrium beam emittance of approximately $1 * 10^{-9}$ m. For all intents and purposes, this orbit offset can be treated as ideal.

Calculations show that there is a limit as to how far an orbit offset can be decreased by dipole tapering. This limit is due to the fact that the particle loses an amount of energy ΔE_{rad} on its trajectory through the dipole via synchrotron radiation. So even if the dipole is set to the local beam energy E_{local}, this energy value is only ever correct at one point within the dipole. Thus, the particle still has an energy deviation $(\frac{\Delta E_{rad}}{2})/E_{local}$ at the beginning of the dipole and $(-\frac{\Delta E_{rad}}{2})/E_{local}$ at the end. Using the transformation matrix method, the dipole can be split into subparts, each of which the particle traverses at slightly different energies. By increasing the number of subparts, the continuous loss of energy throughout the dipole can be simulated. The orbit offset caused by continuous loss of energy due to radiation can be calculated as follows:

$$\begin{pmatrix} x_{after}(s) \\ x'_{after}(s) \\ \frac{-\frac{\Delta E}{2}}{E_{local}} \end{pmatrix} = \prod_{n=N}^{1} \begin{pmatrix} cos\frac{\alpha}{2} & \rho sin\frac{\alpha}{2} & \rho(1-cos\frac{\alpha}{2}) \\ -\frac{1}{\rho}sin\frac{\alpha}{2} & cos\frac{\alpha}{2} & sin\frac{\alpha}{2} \\ 0 & 0 & \frac{\frac{\Delta E}{2}-\frac{n\Delta E}{N}}{\frac{\Delta E}{2}-\frac{(n-1)\Delta E}{N}} \end{pmatrix} \begin{pmatrix} x_{before}(s) \\ x'_{before}(s) \\ \frac{\frac{\Delta E}{2}}{E_{local}} \end{pmatrix} \tag{62}$$

In the case of the FCC-ee racetrack lattice at an energy of 175 GeV and 2 RF cavity sections, this *intrinsic offset*, which exists even in a tapered dipole solely due to the energy loss within the dipole, evaluates to approximately $3 * 10^{-9}$ m. These calculations are in agreement with the orbit shown in figure 23, which shows a kind of "decreased sawtooth effect" caused be the intrinsic orbit offset within dipoles, with a maximum offset of approximately $3 * 10^{-9}$ m.
An ideal orbit with zero offset throughout the machine could only be reached, if the strength of the dipole were to be adjusted to the local beam energy continuously throughout each dipole magnet. Although at this point, it has to be emphasised that a closed orbit in the nanometer scale is orders of magnitude smaller than orbit distortions caused by other sources like misaligned magnets, etc. For all intents and purposes, this tapered orbit can be treated as the ideal design orbit.

Averaged Tapering Strategies

This marks the end of the tapering studies, in which each dipole is treated individually. Two different tapering strategies were introduced, both feasible in real machines and both showing remarkable results within their own natural limits. Tapering with additional magnets showed an orbit improvement of approximately two orders of magnitude, tapering of dipole field strengths even showed an improvement of up to six orders of magnitude, decreasing the orbit to approximately $3 * 10^{-9}$ m. Up to now, the subject was treated regarding to what is ideally possible. Now, the focus will be shifted to what is necessary.
In a real machine, optimization of the individual dipole strengths can be done in different ways, e. g. by using individually powered correction coils at the end of each magnet, in these studies represented by an additional magnet after a dipole, or by adjusting the strength of a dipole with correction coils, in these studies represented by a constant dipole error. In both cases, equipping each dipole with its own correction mechanism will be a very costly task.
Depending on how large an orbit offset can be considered acceptable, two additional tapering scenarios have been taken into consideration. In the first scenario, the already built-in orbit correction system is used. These corrector magnets are normally used to correct orbit fluctuations created by misaligned magnets. They already exist in the machine, so there would be no additional cost in also using them for tapering purposes. The orbit correction magnets are however not located after each dipole but after each quadrupole, as the effectiveness of orbit corrections is proportional to $\sqrt{\beta_u}$ and beta functions take their maximums at the center of focussing quadrupoles in the respective plane. There are therefore two dipoles creating orbit offsets in between each correction. Applying this procedure, the residual orbit decreases to approximately $4 * 10^{-5}$ m and is thus twice as high as with individual tapering using correction kickers (see figure 24).

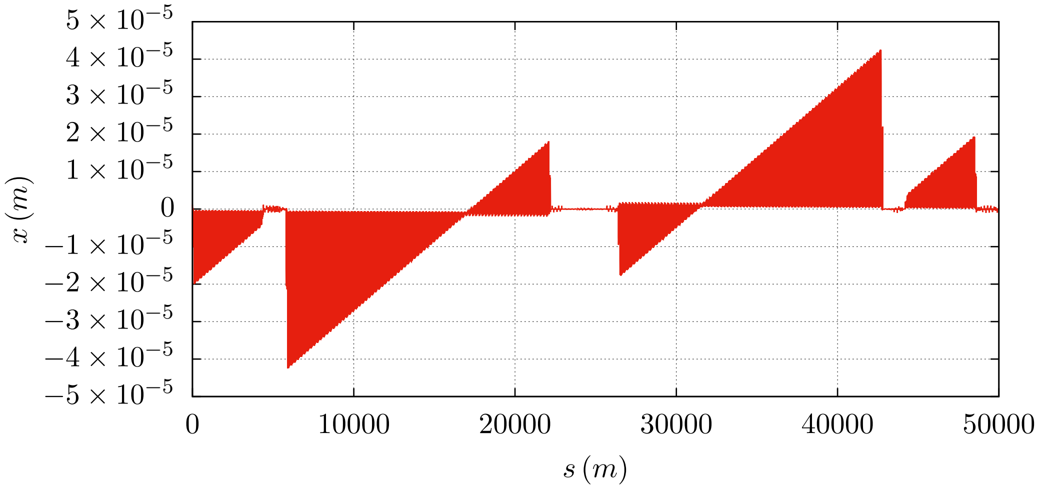

Figure 24: Orbit offset after the tapering procedure of using orbit correction kickers. Due to the fact that orbit correction kickers are implemented after every quadrupole, there are two dipoles creating orbit offset in between each correction. The residual orbit is twice as high as with individual tapering and decreases to approximately $4 * 10^{-5}$ m.

In the second scenario, the concept of grouping dipoles together is taken further. Families of dipoles are created and each dipole family is set to a specific *averaged tapered dipole strength*. This value is acquired by using eq. (54) on each element of the family and averaging over them.

The studies focussed on the racetrack lattice of FCC-ee. Each arc of the layout was chosen to be one dipole family. For the FCC-ee racetrack lattice, this means that there are eight dipole families. However, the racetrack lattice layout consists of two identical halves, so there are only four independent dipole strengths.

Figure 25 shows the orbit offset after this tapering procedure was applied. The lengths of the two different arc types in the racetrack layout (SARC and LARC, see figure 3) differs with 4.4 km and 16.4 km respectively a great deal. As a consequence, the orbit offset in the long arcs is approximately four times larger than in the small arcs.

In order to reduce this difference in orbit offset, the dipoles in the long arcs were split into two dipole families each, increasing the number of dipole families from eight to twelve and the number of individual dipole strength values from four to six.

However, in this case additional quadrupole matching sections are necessary at the crossover of the dipole families in the long arcs. This is necessary because, with the long arcs divided into two families, the orbit is at its maximum negative offset after the first half of the arc (see figure 26). The tapered strengths of the second half however are not designed to cope with this additional offset $x(s)$ and kick $x'(s)$. Therefore, these parameters need to be corrected by installing additional matching sections into the machine, similar to those in between dispersion suppressors and straight sections.

With these changes applied, the maximum offset decreases to approximately $3 * 10^{-4}$ m

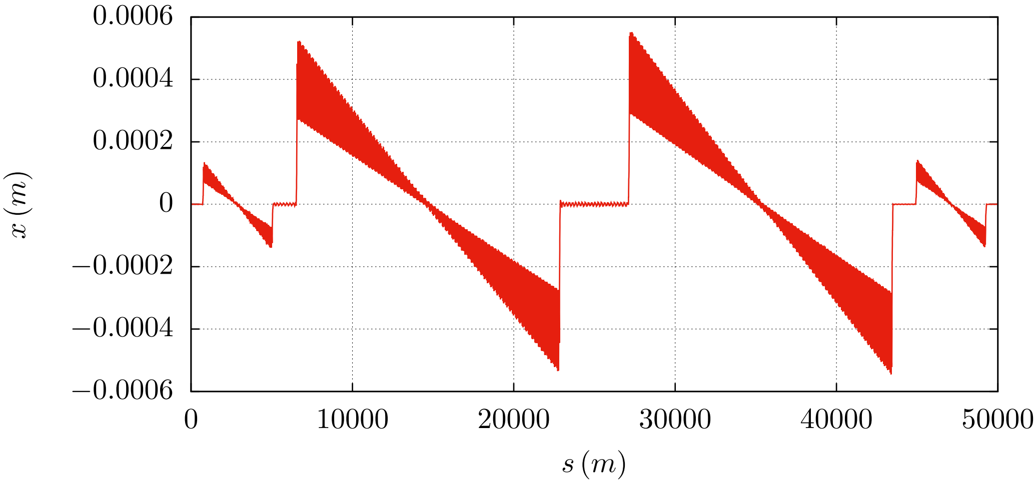

Figure 25: Orbit offset after the tapering procedure of using 8 dipole families of averaged tapered strength. The orbit offset in the long arcs is approximately four times larger than in the short arcs, as in the long arcs, approximately four times as many dipoles are averaged over.

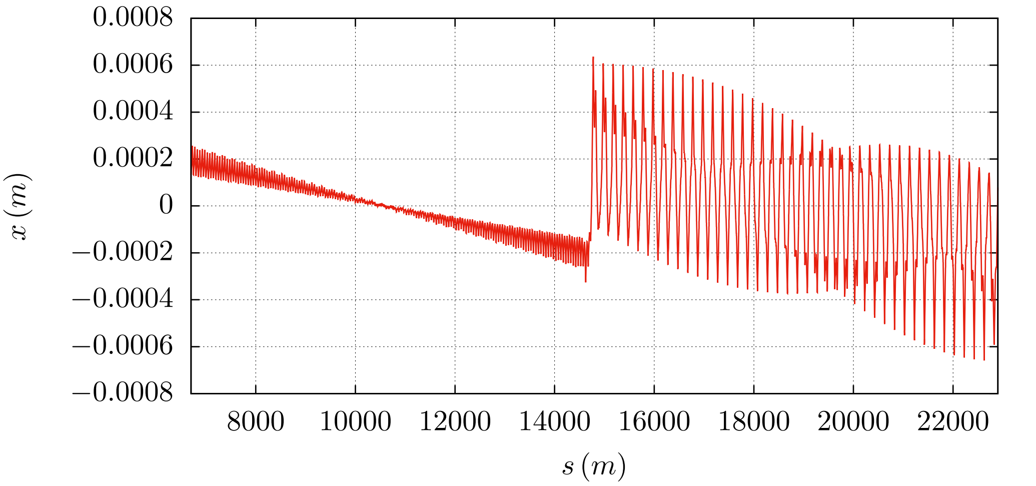

Figure 26: Orbit offset in a long arc section after arcwise tapering using 12 dipole families. Without an additional matching section in the middle of the arc, the tapered dipole strengths of the second half cannot cope with the additional orbit offset $x(s)$ and $x'(s)$ at the point of transition.

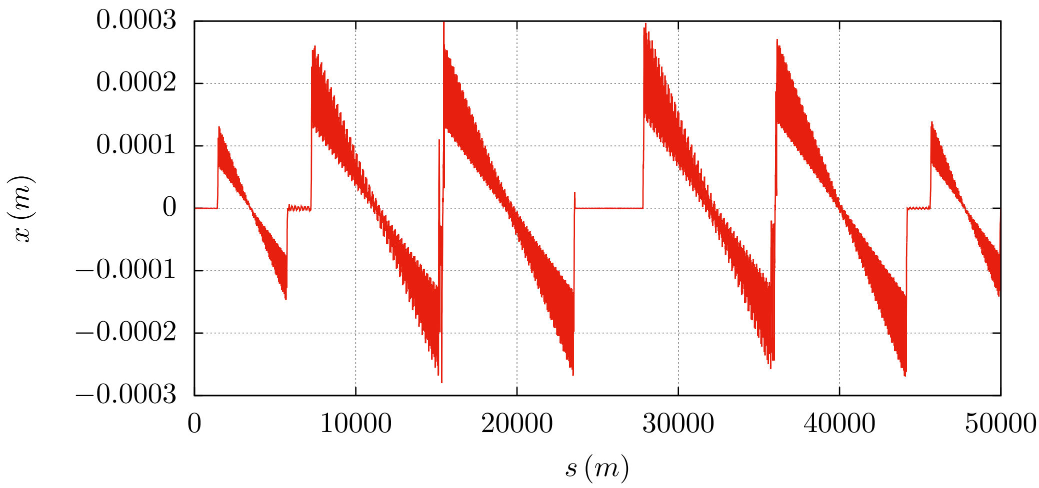

Figure 27: Orbit offset after arcwise tapering using 12 dipole families. With additional matching sections installed in the middle of the long arcs, the orbit can be stabilized and the maximum offset decreases to approximately $3 * 10^{-4}$ m.

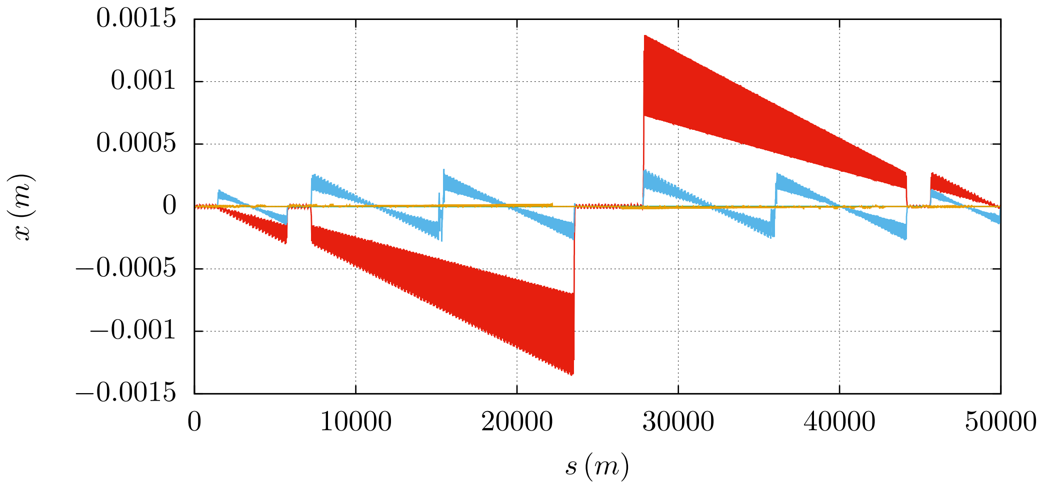

Figure 28: Comparison of the orbit offset without tapering (red), with individual tapering of every dipole using additional tapering magnets (yellow) as well as with arcwise tapering using twelve dipole families (blue). The orbit after individual tapering using dipole errors is not visible, due to the even smaller orbit offset in the order of 10^{-9} m.

(see figure 27).
In the arcwise tapering studies, the changes to the dipoles were applied using additional tapering magnets. However, for these studies, it makes no difference, whether tapering is applied using additional tapering magnets or adjusted dipole fields, as the differences between these two strategies become apparent only at much smaller orbit offsets.
Finally, figure 28 shows a comparison of the orbit offset without tapering, with individual tapering of every dipole using additional tapering magnets as well as with arcwise tapering using twelve dipole families. The orbit after individual tapering using dipole errors is not visible in the plot due to the much smaller orbit offset in the order of magnitude of 10^{-9} m.
To summarize, table 4 shows the different tapering strategies, the factor by which the orbit is decreased as well as the maximum orbit offset after the application of the respective strategy in the FCC-cc racetrack lattice layout at 175 GeV and with 2 RF sections:

Table 4: Overview of the different tapering strategies introduced in these studies. The orbit improvement factor is given by the maximum orbit offset of the untapered orbit, divided by the maximum offset of the tapered orbit. The orbit improvement factor stays roughly the same for every setting of parameters such as lattice layout, energy and number of RF sections. It is therefore a good indicator for the effectiveness of the respective tapering strategy. The maximum offset of the tapered orbit is given for the FCC-ee racetrack lattice layout at 175 GeV and 2 RF sections.

Tapering Strategy	Orbit improvement factor	Maximum orbit offset
Individual tapering using tapering magnets	60	$2.3 * 10^{-5}$
Individual tapering using dipole errors	450000	$3 * 10^{-9}$
Tapering using the orbit correction system	30	$4.2 * 10^{-5}$
arcwise tapering with 8 dipole families	2.5	$5.5 * 10^{-4}$
arcwise tapering with 12 dipole families	4.7	$3 * 10^{-4}$

The orbit improvement factor for each tapering procedure stays roughly the same for each setting of parameters like lattice layout, energy and number of RF sections. For example, the improvement factor of individual taperig using additional magnets is 60, so the orbit in the racetrack lattice with 2 RF sections at 175 GeV reduces from 1.3 mm to approximately $2 * 10^{-5}$ m. With 8 RF sections at 175 GeV, it reduces from $7 * 10^{-4}$ m to approximately $1.2 * 10^{-5}$ m, and with 2 RF sections at 45.5 GeV, it reduces from $2.4 * 10^{-5}$ m to approximately $3.5 * 10^{-7}$ m. More examples of the orbit before and after tapering for the energies of 45.5, 120 and 175 GeV can be found in the appendix.
In conclusion, the sawtooth orbit in a given machine can be reduced rather easily using one of the tapering strategies presented in this thesis. Furthermore, the impact on synchrotron radiation-dependent parameters like energy loss per turn is very small. In fact, in the most

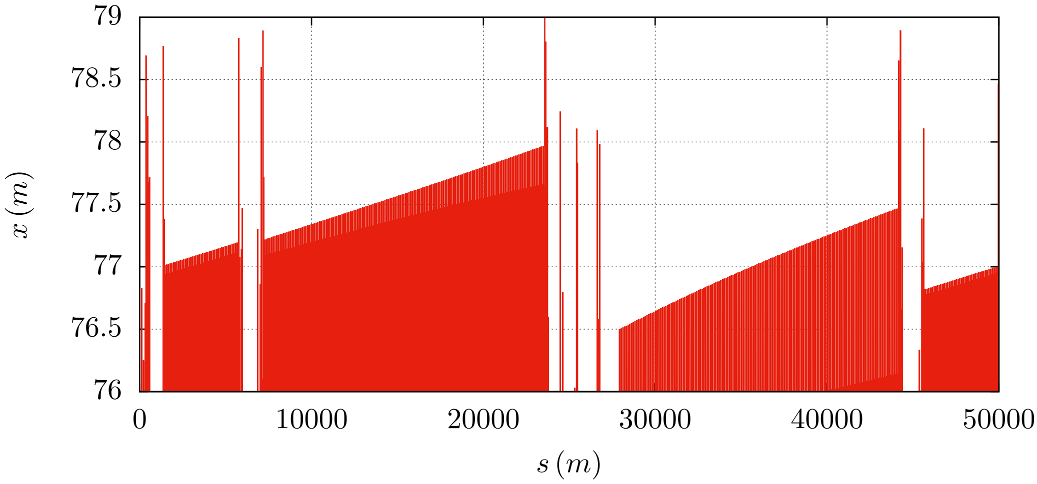

Figure 29: Beta functions over a half ring of the FCC-ee racetrack lattice at an energy of 175 GeV and 2 RF sections. The beta function increases with decreasing beam energy.

extreme case of 175 GeV and 2 RF sections, the energy loss per turn is reduced by 0.34 % and the horizontal emittance is reduced by 2 %. At 45.5 GeV and 2 RF sections, the energy loss per turn is reduced by a factor of $2 * 10^{-6}$ and the horizontal emittance is reduced by a factor of $5 * 10^{-4}$.

Effects of Local Energy Oscillations on Beam Optics

Oscillations of the local beam energy not only influence the bending properties of dipole magnets, but also the focussing properties of quadrupole magnets. The quadrupole focussing strength K_1 depends on the local beam energy in the same way as the dipole bending angle:

$$K_1 = \frac{c\,e}{E_{local}} \frac{dB_y}{dx} \tag{63}$$

The quadrupole strength defines both the phase advance per cell $\Psi(s)$ and the beta function $\beta(s)$. Thus, a variation of the horizontal and vertical quadrupole focussing strengths in turn induces a variation of the beta functions, called the *beta-beat*.

Too high a beta beat can cause the machine to become unstable. In FCC-ee, a beta beat lower than approximately 10 % is regarded a necessary criterion for a stable run. In the FCC-ee racetrack lattice layout at 175 GeV and 2 RF sections, the beta beat due to synchrotron radiation is ≤1.6 %. The beta beat is calculated throughout the lattice by comparing the values of the beta function at each element to the beta function of an ideal optics without radiation. The maximum value is chosen:

$$\frac{\Delta\beta}{\beta} = max(\frac{\beta - \beta_{ideal}}{\beta_{ideal}}) \tag{64}$$

The use of sextupoles in chromaticity correction strategies (see section 5) introduces additional quadrupole fields for off-center particles. A very simple chromaticity correction scheme using only one sextupole family per plane causes the beta beat to increase to 4.9 %. A more complex correction scheme using local chromaticity correction will increase this value further. Additionally, any magnet misalignment has a tremendous effect on the beta beat, as first tolerance studies have shown (see [10]). It is therefore best to keep the beta beat as small as possible. In the case of the simple one family per plane correction scheme, the application of a dipole tapering strategy eliminates all off-center field contributions of the sextupoles and causes the beta beat to decrease to 1.5%. More examples on the positive effect of dipole tapering on the machine stability will be shown in further tolerance studies.

To conclude this section, it can be stated that by using dipole tapering strategies, the sawtooth orbit can be reduced to the theoretical minimum, which is determined only by beam energy and the length of the dipole. In the FCC-ee racetrack lattice at 175 GeV, this minimum is approximately $3 * 10^{-9}$ m. An orbit offset in this order of magnitude renders all orbit distortions caused by feed-down effects negligible. By not assigning an individual tapering strength to each dipole, but grouping dipoles into families and assigning each dipole family an averaged tapered strength, the maximum orbit offset is reduced to a value depending on the number of dipole families. Dipole tapering influences the beam optics by eliminating any off-center contributions of quadrupoles and sextupoles. It reduces the beta beat caused by the implementation of chromaticity correction schemes, magnet misalignments, etc. Further information on how dipole tapering improves beam stability will be delivered by tolerance studies.

4 Wiggler Studies

In radiation sources, insertion elements such as wigglers and undulators are elements to create large intensities of synchrotron radiation. While the spectrum of radiation emitted by wigglers resembles the spectrum of an ordinary bending dipole magnet, undulators create coherent synchrotron radiation of high intensity, which is collimated into a narrow band of frequencies in the spectrum. Light sources use a combination of these two insertion elements to produce high intensities of synchrotron radiation of a desired frequency.
Colliders like FCC-ee however use wigglers for their damping properties. The main goal in these machines is to achieve the highest possible luminosity in order to maximize the collision rate. The luminosity of a collider is indirectly proportional to the transverse beam sizes and thus to the transverse emittances. For that reason, being able to tune the beam emittances within a certain range is crucial to achieve the optimal collider luminosity. This controlled tuning of the beam emittance can be achieved by using wigglers to introduce additional radiation damping or quantum excitation to the machine. As in FCC-ee only wigglers are used, this term will be used primarily. However, the formulae describing particle trajectories and properties of the emitted radiation are valid for both insertion devices.
Wigglers and undulators consist of dipole magnets of alternating polarity in y-direction in order to create a periodic magnetic field B_y. On the plane $y = 0$, the magnetic field has the form

$$B_y(s) = B_{y,0} \cos(\frac{2\pi}{\lambda} s) \tag{65}$$

with the period length λ and the field amplitude $B_{y,0}$. This magnetic field leads to coupled equations of motion for the particle movement within the insertion device

$$\ddot{x} = -\dot{s} \frac{e}{m_e \gamma_L} B_y(s) \tag{66}$$

$$\ddot{s} = \dot{x} \frac{e}{m_e \gamma_L} B_y(s). \tag{67}$$

These equations can be decoupled, because up to the first order the transverse particle velocity $\dot{x}$ is negligible compared to the longitudinal velocity $\dot{s}$. Thus, eq. (66) for the motion in x direction can be solved by assuming $\dot{s} = \beta c$. The resulting velocity $\dot{x}$ can then be plugged into eq. (67) for the movement in s direction.
The result of eq. (66) is an oscillating movement in x direction

$$x(t) = K\frac{\lambda}{2\pi\gamma_L}cos(\frac{2\pi}{\lambda}\beta ct). \tag{68}$$

with the dimensionless factor

$$K = \frac{\lambda e B_{z,0}}{2\pi m_e c}. \tag{69}$$

Using eq. (68) to solve eq. (67), the longitudinal particle trajectory within a periodic wiggler field can be split into two parts. The first part is a reduction of the general particle velocity within the wiggler, which can be expressed in terms of a modification of the β-factor

$$\beta_{wig} = \frac{\dot{s}}{c} = \beta[1 - \frac{1}{2\gamma_L^2}(1 + \frac{K^2}{2})]. \tag{70}$$

The second part is an oscillating movement, similar to the transversal trajectory $x(t)$. These two contributions result in the final longitudinal motion

$$s(t) = \beta_{wig}ct + \frac{K^2\lambda}{16\pi\gamma_L^2}sin(\frac{4\pi}{\lambda}\beta ct). \tag{71}$$

In the coordinate system of a particle moving through the wiggler at the speed $\beta_{wig}c$, the particle trajectory resembles a closed 8-shape. For $K \ll 1$, the longitudinal oscillation can be considered negligible. Without this longitudinal velocity and thus energy oscillation, the particle behaves like a Hertzian dipole and emits monochromatic radiation of a certain frequency $\omega = \gamma_L \frac{2\pi}{\lambda}\beta c$, which is the frequency of the Lorentz-contracted particle oscillations through the wiggler of a period length λ. Using a Lorentz transformation back to the laboratory system, the wavelength of the radiation emitted by an insertion element depending on the emission angle θ_W with respect to the beam axis is:

$$\lambda_l(\theta_W) = \frac{\lambda_u}{2\gamma_L^2}(1 + \frac{K^2}{2} + \gamma_L^2\theta_W^2). \tag{72}$$

The dimensionless factor K is actually used to distinguish between wigglers and undulators. The maximum emission angle of radiation emitted by an insertion element is $\theta_{W,max} \approx \frac{K}{\gamma_L}$. If $K \leq 1$, the maximum emission angle is smaller than the natural opening angle of synchrotron radiation $\frac{1}{\gamma_L}$. This means that the radiation field of photons contains contributions from various wiggler poles, which overlap and interfere with each other. The radiation spectrum therefore consists of a spectral line of the frequency ω_l with a very narrow bandwidth of $\Delta\omega_l = \frac{\omega_l}{N_{wig}}$ and its higher harmonics. The width of the peaks in the spectrum is proportional to ω_l as well as the number of the wiggler poles N_{wig}. An insertion device featuring a spectrum with these characteristics is called an undulator.

If $K \gg 1$, the maximum emission angle exceeds the natural opening angle of synchrotron radiation by a large factor. This means that every point of the insertion element can be treated as an independent source of radiation. There is no interference of the radiation

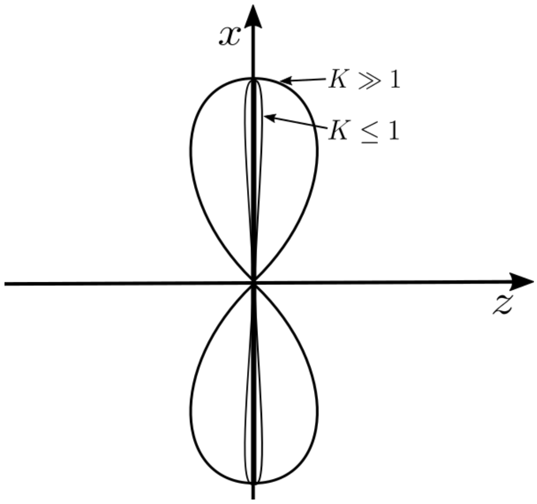

Figure 30: Normalized particle trajectory in the comoving coordinate system of a particle moving through the wiggler at the speed $\beta_{wig}c$. If $K \leq 1$, the longitudinal oscillation can be neglected and the particle behaves like a Hertzian dipole, emitting monochromatic dipole radiation of the frequency $\omega = \gamma_L \frac{2\pi}{\lambda} \beta c$

emitted from different locations in the magnet. The spectrum of the emitted synchrotron radiation is continuous and resembles the spectrum of an ordinary bending magnet. An insertion device featuring a spectrum with these characteristics is called a wiggler. For the reasons explained above, the elements used in the FCC-ee lattice are wigglers.

Depending on where wigglers are located within the machine, they influence the accelerator differently. In the following calculations, it is assumed that over the length of the wiggler element, neither the beta functions nor the dispersion functions fluctuate significantly. This assumption is fulfilled sufficiently well in FCC-ee. If the wiggler is installed in a section without dispersion, the overall synchrotron radiation integral $\mathcal{I}_5$ remains unchanged. However, there is synchrotron radiation created within the wiggler, contributing to the radiation integral $\mathcal{I}_2$. The emittance thus decreases according to:

$$\Delta\epsilon_x = -C_q \frac{\gamma_L^2}{J_x} \frac{\mathcal{I}_{5x}}{\mathcal{I}_{2,ring}^2} \mathcal{I}_{2,wiggler} \tag{73}$$

with $\mathcal{I}_{2,wiggler}$ being the contribution of the wiggler element to $\mathcal{I}_2$ and the factor $C_q = \frac{55}{32\sqrt{3}} \frac{\hbar}{\mathrm{m_e c}} \approx 3,832 \cdot 10^{-13}$. Thus, the overall beam emittance decreases. Such a wiggler is called *damping wiggler*. If the wiggler is installed in a dispersive section of the accelerator, the overall emittance changes according to:

$$\Delta\epsilon_x = C_q \frac{\gamma_L^2}{J_x} \left(\frac{1}{\mathcal{I}_{2,ring}} \mathcal{I}_{5x,wiggler} - \frac{\mathcal{I}_{5x}}{\mathcal{I}_{2,ring}^2} \mathcal{I}_{2,wiggler}\right). \tag{74}$$

Thus, depending on where in the accelerator the wiggler is installed, either the radiation damping effect can dominate and the emittance decreases, or the contribution of $\mathcal{I}_5$ domi-

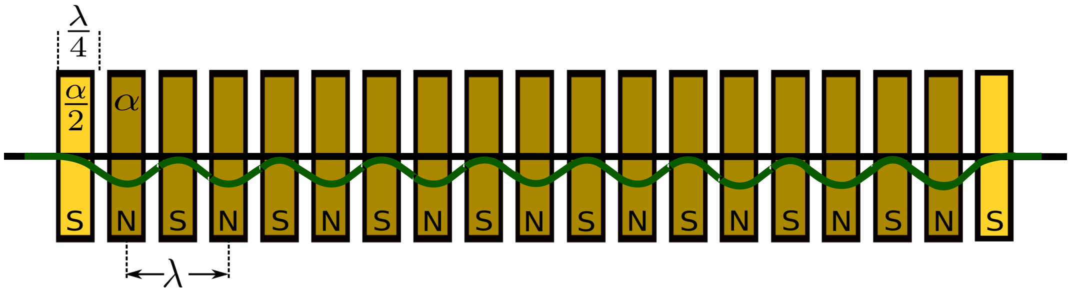

Figure 31: Basic layout of a 19 pole half-bend wiggler. The poles are of equal length, so in order for the end poles (yellow) to have half the bending angle of the central poles (ochre), they must have half the magnetic field strength. Due to the equal bending angle of the central poles, the wiggler period length is constant throughout the wiggler. A particle trajectory throughout the wiggler is depicted in green.

nates and the emittance increases. A wiggler which is installed in a dispersive section and therefore increases the emittance is called an *excitation wiggler*.
The exact design of a damping wiggler (pole and gap length, number of wiggler poles,...) installed in a dispersion free section is of minor importance, as the emittance solely decreases due to the increase of synchrotron radiation and thus only depends on the sum of the squared dipole bending angles of the wiggler dipoles $\sum_i \frac{\alpha_i^2}{l_i}$.
The specific location of an excitation wiggler however does very much matter, as the emittance depends on the radiation integral $\mathcal{I}_5$, which in turn depends on the local dispersion $D(s)$ and the first derivative of the dispersion $D'(s)$. Choosing the right location means a bigger contribution to $\mathcal{I}_5$ and therefore an increase in efficiency of the excitation wiggler.
In order for the wiggler field not to interfere with the closed orbit and to not deflect the beam in any way, the following condition must be fulfilled:

$$\int_{wiggler} B_y(s)ds = B_{y,0} \int_{wiggler} \cos(\frac{2\pi}{\lambda}s)ds = 0 \tag{75}$$

In principal, there is no constraint on how this condition can be fulfilled. However, one particular way to achieve this is the so called half-bend wiggler, which features central poles of equal bending angle and edge poles adjusted to half the bending angle of the central poles. This way, the wiggler length always yields

$$l_{wiggler} = n\lambda + \frac{\lambda}{2} \tag{76}$$

with λ being the wiggler period length and n being the number of period lengths. A period length is the distance a particle travels in order to perform a full oscillation in the magnetic field of the wiggler. In half-bend wigglers, a wiggler period equals the lengths of two central poles and two gaps.

Another important parameter for dipole magnets and especially wigglers is the *critical energy*

$$E_{crit} = \frac{3\hbar c \gamma_L^3}{2\rho} \tag{77}$$

with the dipole bending radius ρ. The critical energy is a parameter used to describe the characteristics of the synchrotron radiation spectrum of bending magnets. A critical energy higher than 1 MeV means that electron-positron pair production effects can occur. Depending on the location within the accelerator, this can lead to additional strain on the radiation protection, as well as to unwanted signals in detectors and must therefore be avoided.

Wiggler Designs

Damping Wigglers

In this section, different wiggler designs will be introduced and tested in the FCC-ee racetrack lattice. First, the wigglers will be placed in dispersion free sections and will therefore work as damping wigglers. Later on, dispersion will be introduced in these sections and the wigglers will work as excitation wigglers.
In a real machine, the emittance only needs to be tunable around the design value by a factor of about 10%, as the accelerator lattice was already designed to have the optimal beam emittance and luminosity. However, small deviations from this optimal value can occur due to a number of reasons like magnet alignment and field errors, feed-down effects and collective effects like the beam-beam effect, the impedance of the accelerator, etc. It is these deviations that can be corrected by the use of excitation or damping wigglers. However, in order to test the viability of the different wiggler designs over a large range of magnetic field strength, a much more challenging goal of a factor of 2 in emittance increase or decrease was chosen for the following studies.
The first design which was taken into consideration was that of FCC-ee's predecessor, LEP. LEP was another electron-positron accelerator, which was built in the tunnel that now houses the LHC. It therefore had a length of 27 km, was operated at a center-of-mass energy of 91 GeV to 100 GeV and was later upgraded to 200 GeV.
In LEP, eight wigglers were used, each with a total length of 2.99 m. Each wiggler consisted of three dipole magnets. The middle pole had a length of 0.74 m and was operated at a field strength of 1 T, the edge poles had a length of 0.925 and were operated at 0.4 T, resulting in the required overall bending angle of zero.
Radiation emitted by the main pole of this wiggler inserted to the FCC-ee racetrack lattice at a beam energy of 175 GeV has a critical energy of 21 MeV. This value exceeds the pair production threshold of 1 MeV by a large amount and pair production effects within the wiggler must therefore be taken into consideration.

The contribution of the wiggler to the second synchrotron radiation integral evaluates to $\mathcal{I}_{2,wiggler} = 3.0404 * 10^{-6}$. The radiation loss per wiggler is then approximately 40 MeV and the emittance decreases by:

$$\Delta\epsilon = -2.5 * 10^{-12}. \tag{78}$$

Therefore, with a horizontal beam emittance of 1.3 nm, approximately 50 of these wigglers would be necessary in the FCC-ee lattice at 175 GeV to reduce the emittance by 10 %.
With superconducting magnet coils, magnetic fields greater than 1 T are easily achievable, so one could be tempted to keep the LEP design and just increase the magnetic field strength. This, however, is not possible, as figure 33 shows.
The behaviour of the emittance in figure 33 can be explained as follows. Up to now, it was assumed that the dispersion in wigglers located in dispersion free straight sections is zero at every point in the wiggler. This, however, is not true, as the wiggler poles themselves are a source of dispersion. Although in order to prevent any influence of the wiggler on the beam, the overall dispersion must be zero, this rule does not forbid for dispersion to exist within the wiggler. This internal dispersion created by the wiggler poles (see figure 34) in turn creates a $\mathcal{I}_5 \neq 0$ and a positive contribution to the horizontal emittance $\Delta\epsilon > 0$. In some wiggler designs, this contribution can outweigh the damping effect and lead to an overall increase of the emittance.
It is therefore impossible to simply use the design of the LEP-wiggler with increased the magnetic field strength.
A new damping wiggler design must focus on keeping the internal dispersion of the wiggler small. This can be achieved by shortening the wiggler pole and gap lengths. To increase the impact each wiggler has on the emittance, more poles can be added. During the course of these studies, wiggler designs with 39, 79, 119 and 159 poles have been tested. In these designs, both the edge and the central poles have a length of 10 cm, interrupted by gaps of 2.5 cm. By shortening the pole lengths, higher magnetic field strengths can be realised without resulting in too high an internal dispersion. In all four cases, 16 wigglers were distributed equally in the four long straight sections (LSS) of the FCC-ee racetrack lattice

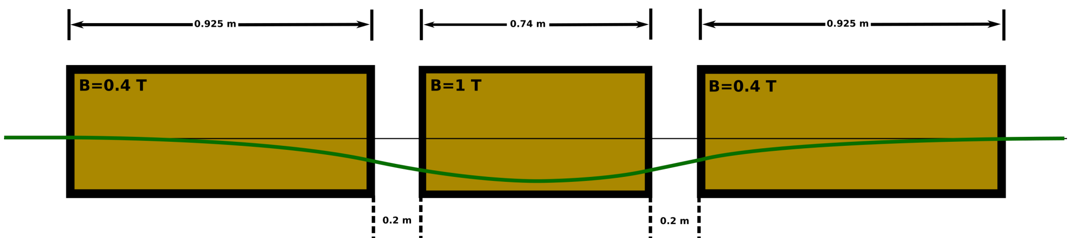

Figure 32: Basic layout of the 3 pole LEP wiggler. Due to the low number of poles, only half a wiggler period is fulfilled. The particle trajectory throughout the wiggler is shown in green.

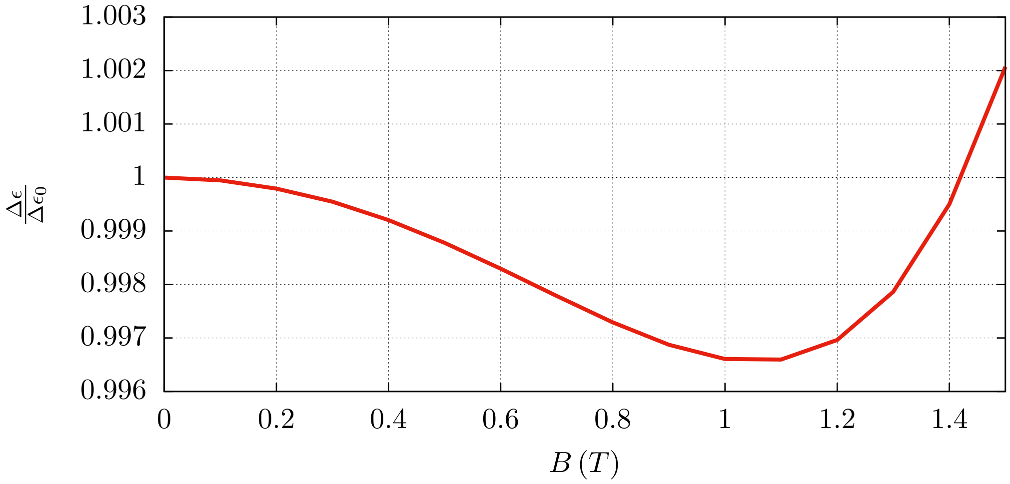

Figure 33: Relative horizontal emittance against the magnetic field of the main wiggler pole. For low field strengths, the damping effect predominates and the emittance decreases. However, when the magnetic field reaches a strength of approximately 1.1 T, the contribution of $\mathcal{I}_5$ created by the internal dispersion of the wiggler poles starts to outweigh the damping effect and the emittance increases.

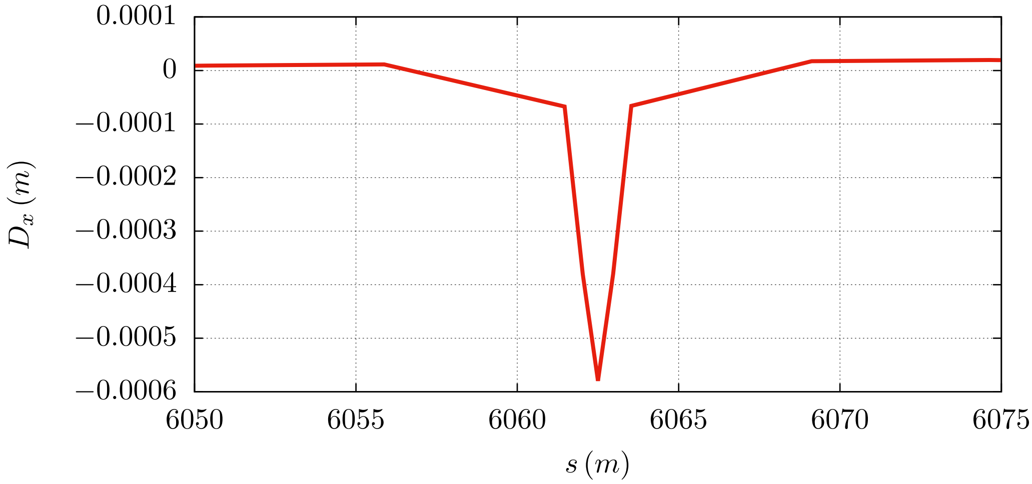

Figure 34: Dispersion created within the wiggler. With sufficient dipole strengths, this dispersion creates a contribution to $\Delta\epsilon$ high enough to outweigh the emittance decreasing effect of radiation damping.

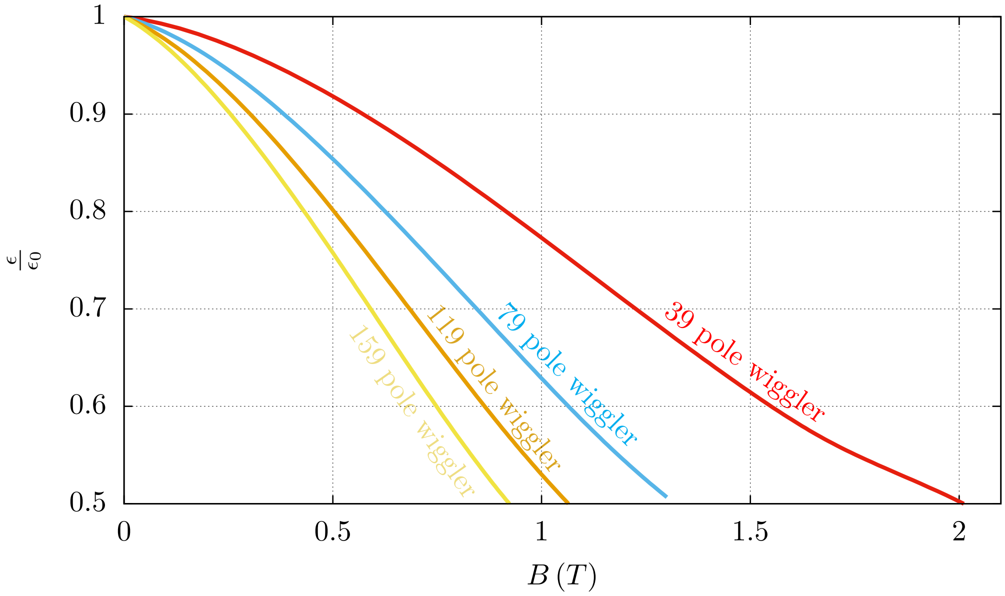

Figure 35: Relative horizontal emittance against the magnetic field of the main wiggler poles B for the 39, 79, 119 and 159 pole wigglers in the FCC-ee racetrack lattice at an energy of 175 GeV.

(see figure 3). The 39, 79, 119 and 159 pole wigglers have a length of 4.85 m, 9.85 m, 14.85 m and 19.85 m, respectively. The maximum length of a wiggler design is limited by the available space in between a defocussing and focussing quadrupole of a lattice cell, which is 23.5 m. The 159 pole wiggler is already close to this upper limit. The four designs were studied using the FCC-ee racetrack lattice design at energies of 45.5 GeV, 120 GeV and 175 GeV.

Figures 35 to 37 show the decrease of the horizontal emittance ϵ_x against the magnetic field strength of the wiggler main poles B at a beam energy of 175 GeV. Contrary to the 3 pole wiggler design, it is possible to decrease the horizontal emittance to $0.9\epsilon_0$ and even to $0.5\epsilon_0$ with all four designs. An emittance reduction of 10 % is achieved between a magnetic field strength of approximately 0.25 T with the 159 pole design and approximately 0.6 T with the 39 pole design. The radiation loss, at which this emittance reduction is achieved, is the same for all four wiggler designs and is approximately 8.8 GeV at $0.9\epsilon_0$ and approximately 16 GeV at $0.5\epsilon_0$ (see figures 36 and 37). The reason for this is that in the case of an ideal damping wiggler, the decrease of the emittance is purely achieved by additional radiation damping. A few basic calculations

$$\epsilon_x = C_q \frac{\gamma_L^2}{J_x} \frac{\mathcal{I}_{5x}}{\mathcal{I}_2} = C_q \frac{\gamma_L^2}{J_x} \frac{\mathcal{I}_{5x}}{\mathcal{I}_{2,ring} + \mathcal{I}_{2,wiggler}} \tag{79}$$

show, that in order to decrease the emittance by 10 %, $\mathcal{I}_{2,wiggler}$ must be $\frac{1}{9}\mathcal{I}_{2,ring}$, so the

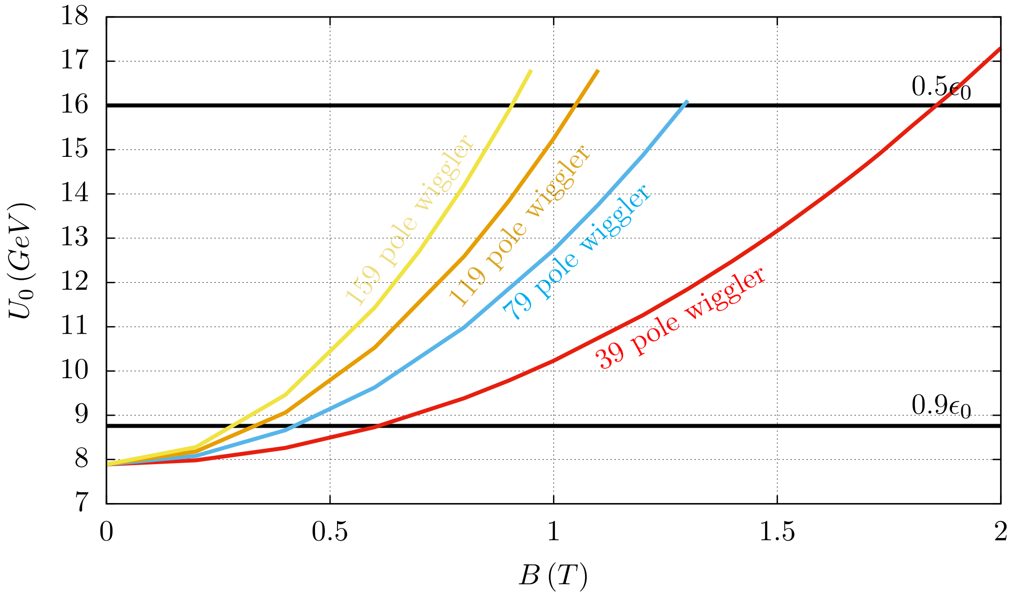

Figure 36: Energy loss per turn U_0 against the magnetic field of the wiggler main poles B for the 39, 79, 119 and 159 pole wigglers in the FCC-ee racetrack lattice at an energy of 175 GeV. The black horizontal lines mark the energy loss, at which the horizontal emittance is decreased to $0.9\epsilon_0$ and $0.5\epsilon_0$. The energy loss per turn at $0.5\epsilon_0$ is 16 GeV, more than twice the energy loss without wigglers. This additional energy loss is a result of the dispersion created by the wiggler poles, which causes a positive contribution to the emittance. This contribution must be coped with additional radiation damping, calling for higher field strengths and additional energy loss.

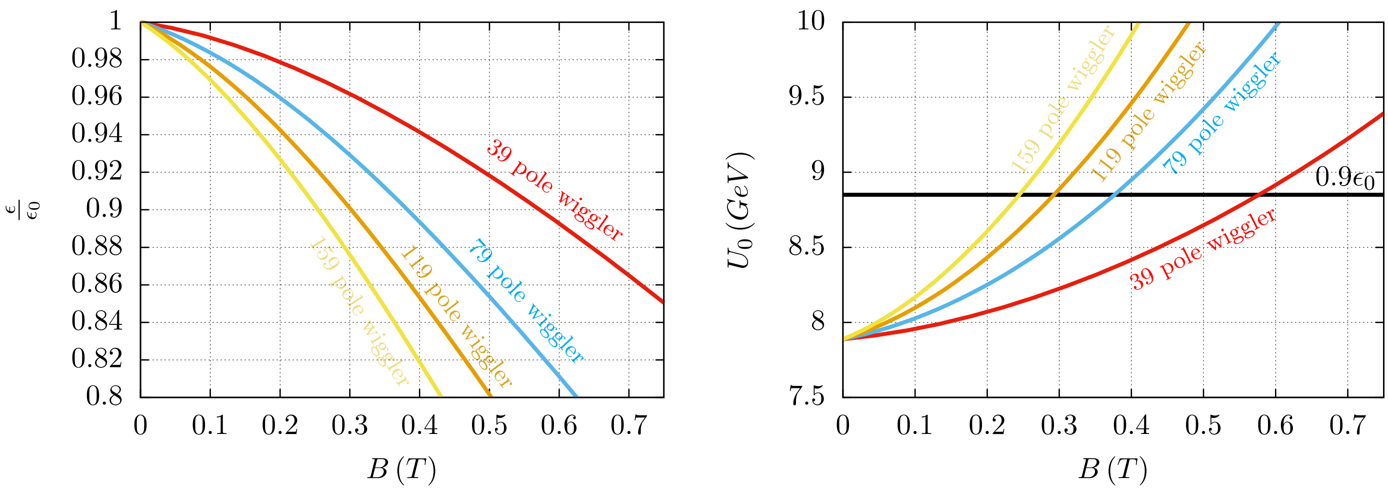

Figure 37: More detailed view of figures 35 and 36, showing the important parameter space around an emittance decrease of 10 %.

amount of synchrotron radiation emitted by the 16 wigglers is one ninth of the total amount emitted in the arcs. This result is true for every lattice design at every energy. For the FCC-ee racetrack lattice at an energy of 175 GeV, this means an additional energy loss of approximately 0.88 GeV per turn (see figure 37).
According to equation (74), dispersion created by the wiggler poles causes a $\mathcal{I}_{5,wiggler} \neq 0$ and thus a positive contribution to the emittance. This positive contribution has to be coped with additional radiation damping. Therefore, higher magnetic field strengths are necessary in a real wiggler than in an ideal damping wiggler with $\mathcal{I}_{5,wiggler} = 0$ in order to decrease the emittance. Higher magnetic field strengths also mean additional radiation loss. For that reason, the total energy loss per turn at $\epsilon = 0.5\epsilon_0$ in figure 36 is approximately 16 GeV instead of the radiation loss of an ideal damping wiggler of 15.76 GeV.
At the magnetic field strength necessary to decrease the emittance by 10 %, the critical energy of synchrotron radiation emitted by the wiggler poles is between 4.89 MeV in case of the 159 pole wiggler and 11.82 MeV in case of the 39 pole wiggler.
Figures 38 to 42 show the behaviour of the horizontal emittance and the energy loss per turn against the magnetic field strength of the wiggler main poles for beam energies of 120 and 45.5 GeV respectively. At 120 GeV, the 39 pole wiggler design deviates from the other designs. The horizontal emittance cannot be decreased to $0.5\epsilon_0$, but rather shows a minimum at approximately $0.62\epsilon_0$. Further increase of the magnetic field results in an increase of the emittance. This is similar to the behaviour of the 3 pole wiggler. The dispersion created by the wiggler poles causes a $\mathcal{I}_{5,wiggler}$, which at approximately 1.1 T starts to outweigh the damping effect.
At 120 GeV, the critical energy of the synchrotron radiation emitted from the wiggler dipoles at the field strengths necessary to decrease the emittance by 10 % ranges from 1.53 MeV in case of the 159 pole wiggler to 3.16 MeV in case of the 39 pole wiggler. At 45.5 GeV, the emittance again shows no atypical behaviour. The critical energy at an emittance decrease of 10 % is below the pair production threshold and ranges from 0.083 MeV in case of the 159 pole wiggler to 0.17 MeV in case of the 39 pole wiggler.

Excitation Wigglers

Now, the properties of the presented wiggler designs will be studied when working as excitation wigglers. The goal is to increase the horizontal beam emittance by 10 %, although in order to test the viability of the wiggler designs, again a larger range of the magnetic field strength is covered. It can be shown that an increase of the emittance by a factor of 2 is possible. For the following studies, the accelerator lattice was slightly altered. In order to create dispersive straight sections, the dispersion suppressors in the two opposing straight sections LSS1 and LSS3 (see figure 3) in the FCC-ee racetrack lattice were removed. The dispersion in these sections is of the same order of magnitude as the dispersion in the arcs. As the contribution of $\mathcal{I}_{5,wiggler}$ in eq. (74) has a much larger effect on the emittance than

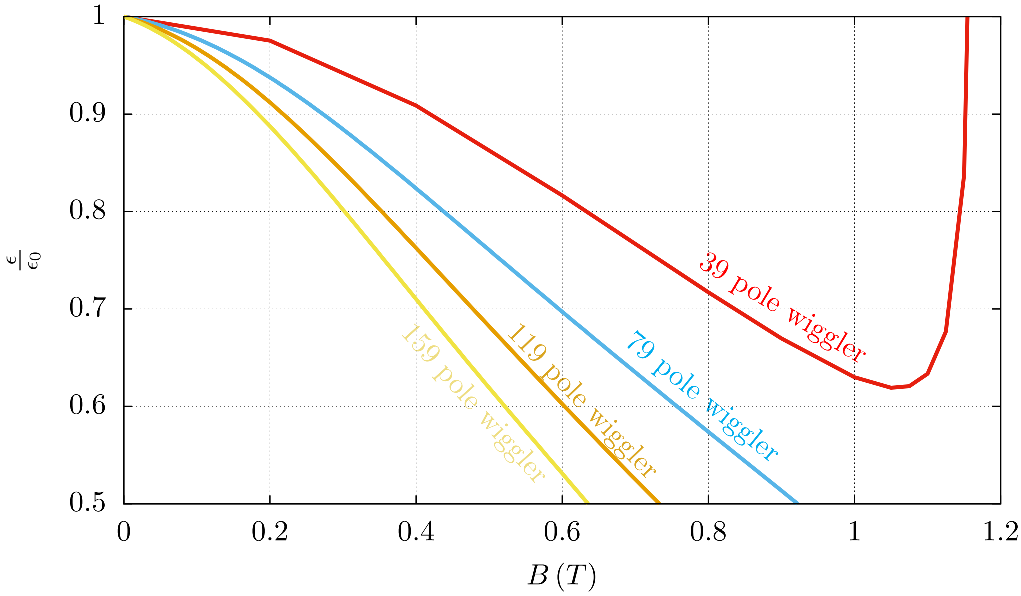

Figure 38: Relative horizontal emittance against the magnetic field of the main wiggler poles B for the 39, 79, 119 and 159 pole wigglers in the FCC-ee racetrack lattice at an energy of 120 GeV. The 39 pole wiggler deviates from the other designs and shows a minimum of the horizontal emittance of $0.62\epsilon_0$ at a field strength of 1.05 T.

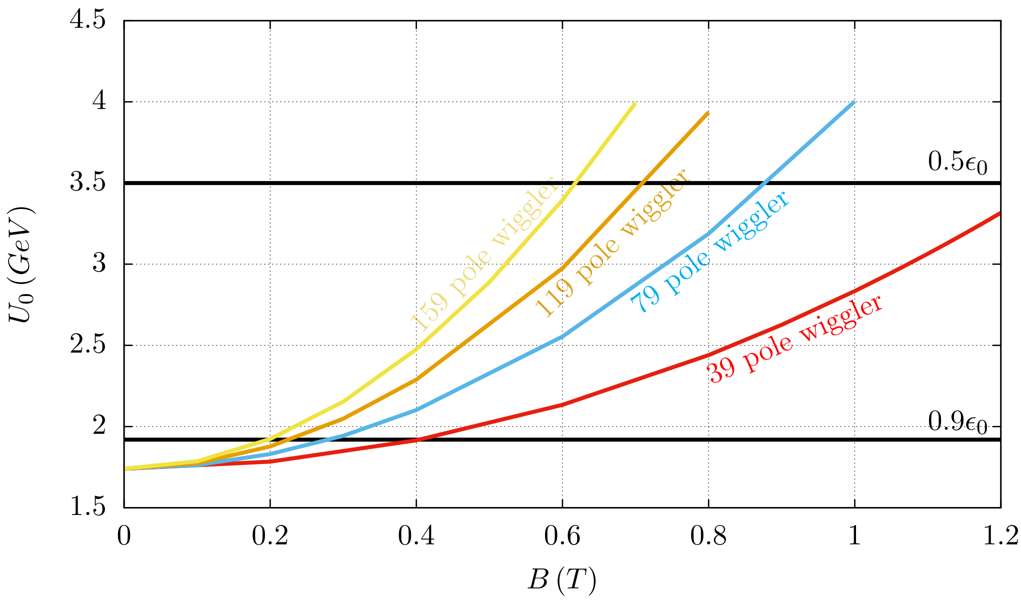

Figure 39: Energy loss per turn U_0 against the magnetic field of the wiggler main poles B for the 39, 79, 119 and 159 pole wigglers in the FCC-ee racetrack lattice at an energy of 120 GeV. The black horizontal lines mark the points, at which the horizontal emittance is decreased to $0.9\epsilon_0$ and $0.5\epsilon_0$.

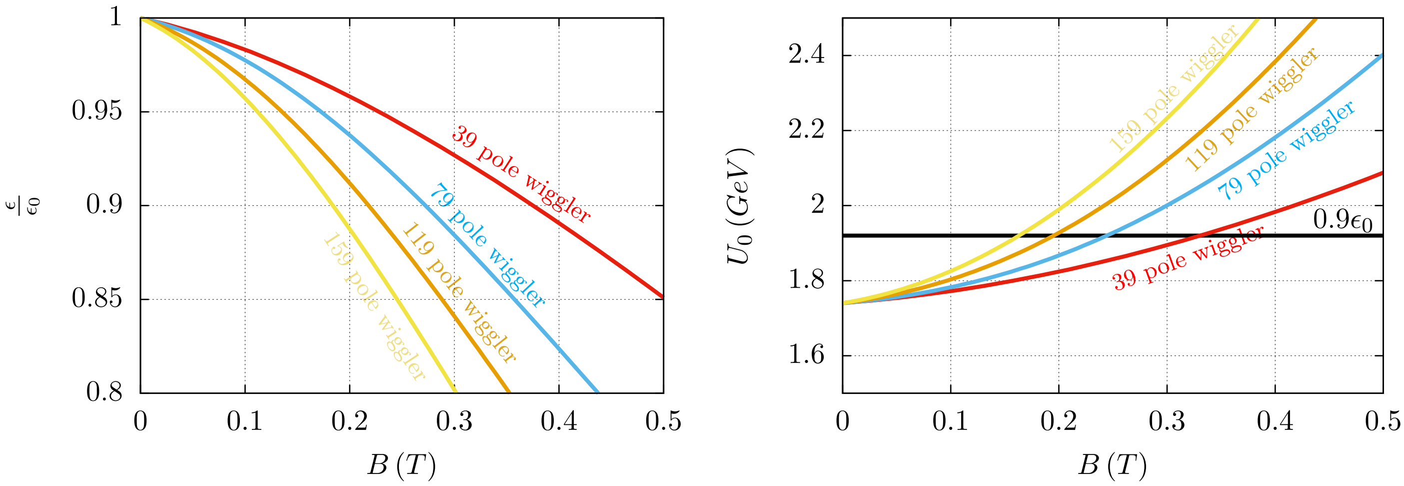

Figure 40: More detailed view of figures 38 and 39, showing the important parameter space around an emittance decrease of 10 %. The deviating behaviour of the 39 pole wiggler caused by the internal dispersion cannot yet be observed, as it only becomes apparent at higher magnetic field strengths.

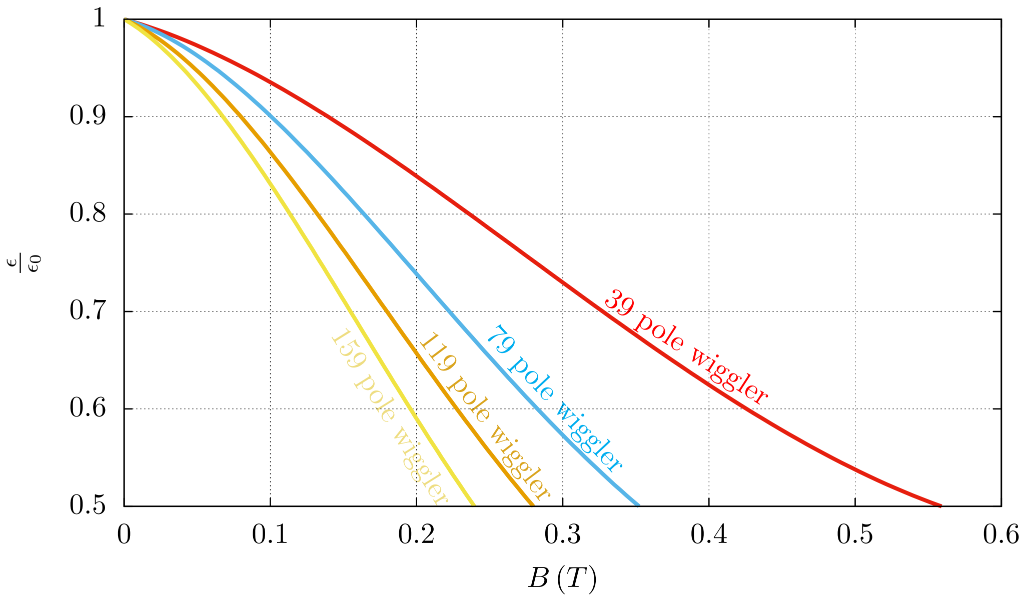

Figure 41: Relative horizontal emittance against the magnetic field of the main wiggler poles B for the 39, 79, 119 and 159 pole wigglers in the FCC-ee racetrack lattice at an energy of 45.5 GeV.

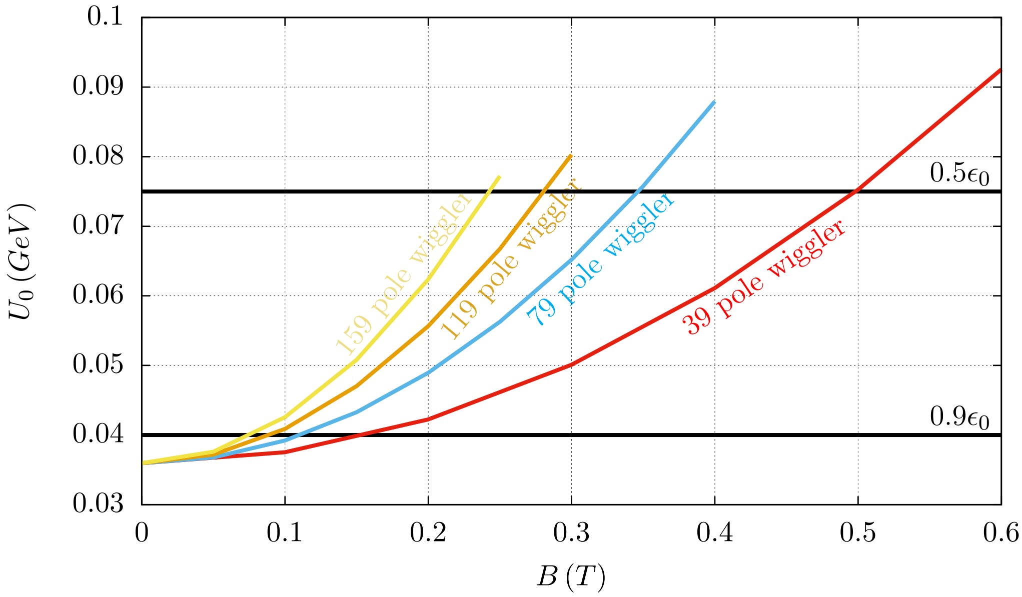

Figure 42: Energy loss per turn U_0 against the magnetic field of the wiggler main poles B for the 39, 79, 119 and 159 pole wigglers in the FCC-ee racetrack lattice at an energy of 45.5 GeV. The black horizontal line mark the points, at which the horizontal emittance is decreased to $0.9\epsilon_0$ and $0.5\epsilon_0$.

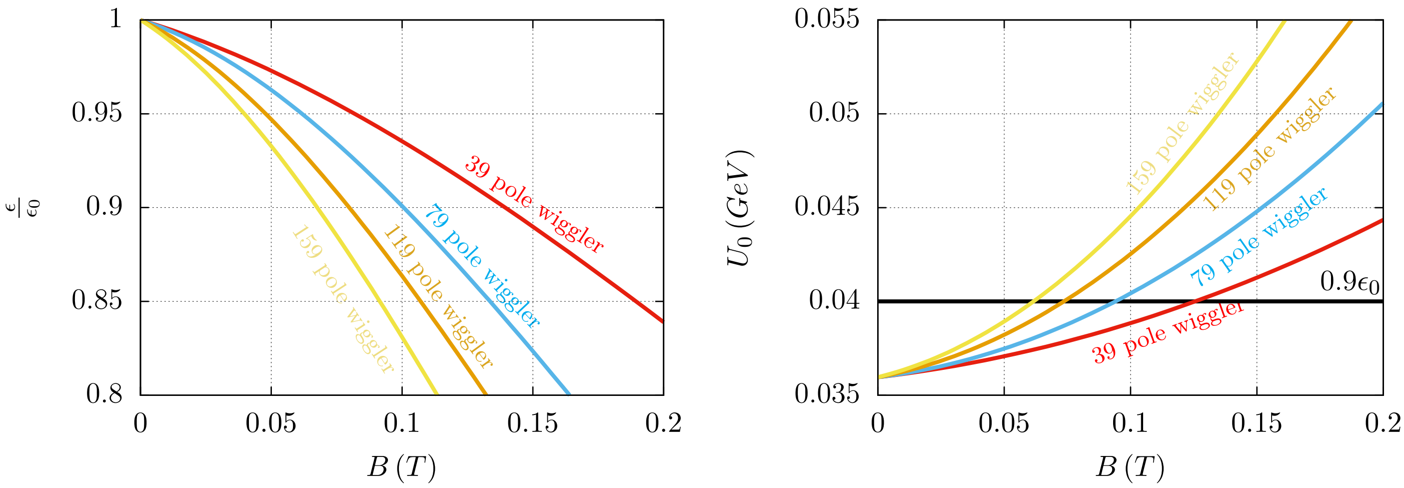

Figure 43: More detailed view of figures 41 and 42, showing the important parameter space around an emittance decrease of 10 %.

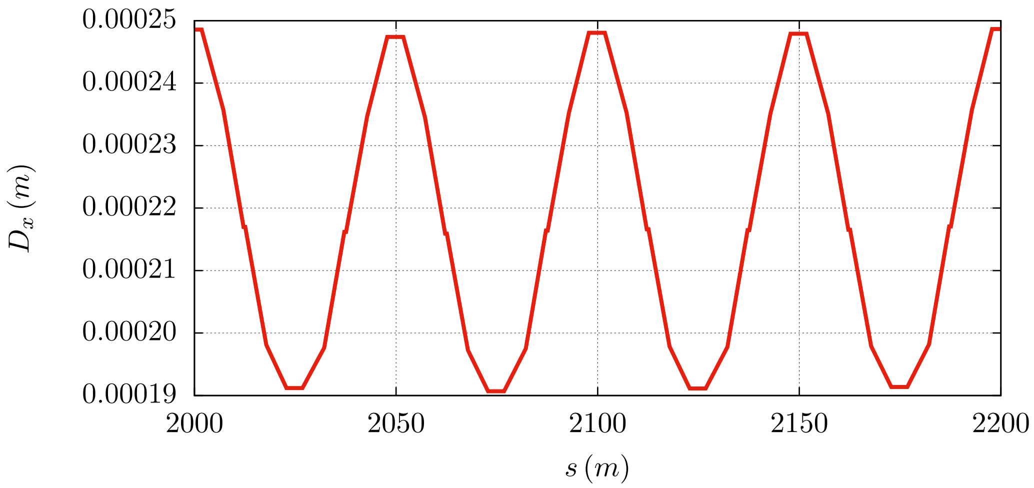

Figure 44: $\mathcal{H}$-function of four arc cells in the FCC-ee racetrack lattice at an energy of 175 GeV. Excitation wigglers should be placed close to the defocussing quadrupoles at the beginning or end of each cell, in order to optimize their impact on the emittance.

the contribution of $\mathcal{I}_{2,wiggler}$, much fewer wigglers are needed to increase the emittance than to decrease it.

Contrary to the damping wiggler studies, the location of the excitation wiggler within the lattice cell does very much matter, as can be seen in figure 44. The $\mathcal{H}$-function, which is used to calculate $\mathcal{I}_5$, oscillates within the cell, so choosing a location with a high $\mathcal{H}$-function leads to a higher impact on the emittance and thus to the need of fewer wigglers and lower magnetic fields.

For the following studies, only two wigglers were installed in the accelerator, one in each dispersive straight section. Again, the 39, 79, 119 and 159 pole wiggler designs have been tested. Additionally, the 3 pole LEP-design wiggler was tested as well. At 175 GeV, the wigglers were placed in locations with a dispersion of approximately 0.1 m, which is in the order of magnitude of the dispersion within the arcs.

Figures 45 and 46 show the relative horizontal emittance against the magnetic field strength for the FCC-ee racetrack lattice at 175 GeV. The 39 to 159 pole wigglers behave in a relatively similar manner, each addition of poles reducing the magnetic field strength necessary to increase the emittance. The behaviour of the LEP-type 3 pole wiggler however strongly deviates from the other designs. This is due to the longer wiggler poles and gaps, which create a much higher dispersion and $\mathcal{I}_{5,wiggler}$ even at lower fields, resulting in an emittance increase by a factor of 2 at an energy loss per turn of only 7925 MeV, compared to the considerably higher values from 8320 MeV for the 39 pole wiggler to 8570 MeV for the 159 pole wiggler.

The critical energy of the synchrotron radiation emitted by the different wiggler designs

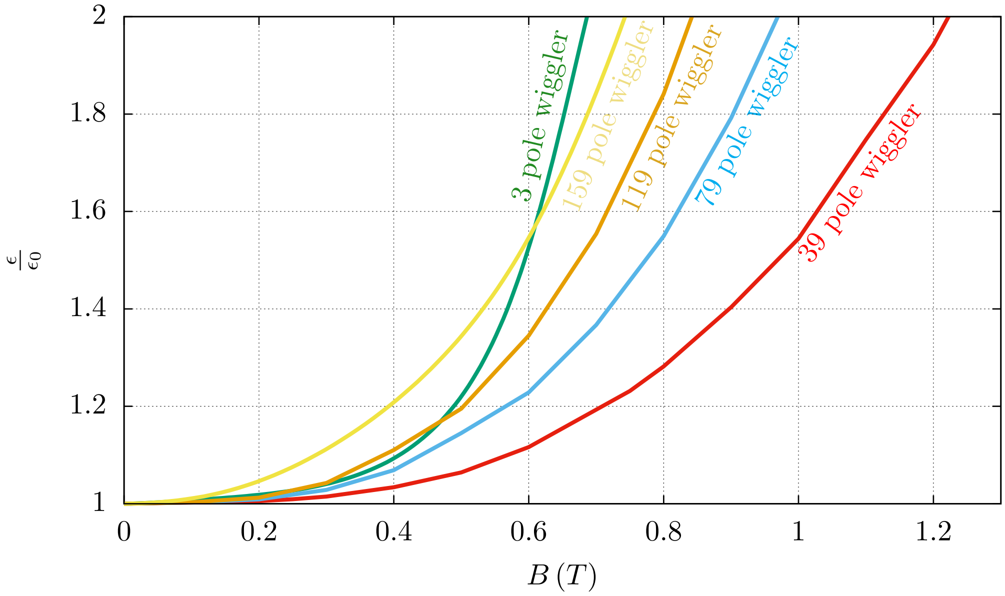

Figure 45: Relative horizontal emittance against the magnetic field of the main wiggler poles B for the 3, 39, 79, 119 and 159 pole wigglers in the FCC-ee racetrack lattice at an energy of 175 GeV. The 3 pole wiggler design strongly deviates from the others and becomes more efficient at higher field strengths.

at field strengths necessary for an emittance increase of 10 % is again higher than the pair-production threshold, reaching values from 5.7 MeV in case of the 3 pole wiggler to 10.4 MeV in case of the 39 pole wiggler. In damping wigglers, the additional energy loss per turn in order to reach a certain decrease in emittance is more or less the same for each wiggler design. This value is determined mainly by radiation damping and corrected only slightly by the contribution of $\mathcal{I}_{5,wiggler}$, which is different for each of the wiggler designs. In the case of excitation wigglers however, the additional energy loss per turn in order to reach a certain increase in emittance varies with each design, as now factors like the location of the wiggler within the cell and the $\mathcal{H}$-function within the wiggler must be taken into account.
Figures 45 to 47 show the increase of the horizontal emittance ϵ_x and the total energy loss per turn U_0 against the magnetic field strength of the wiggler main poles B at a beam energy of 175 GeV. The 159 pole wiggler increases the emittance by 10 % at field strengths of only 0.28 T. However, the 3 pole wiggler, although it requires a field strength of 0.41 T in order to increase the emittance by 10 %, causes the least additional radiation loss of only 21 MeV. The 159 pole wiggler requires an additional 130 MeV in order to achieve the same result. At higher field strengths, the 3 pole wiggler becomes the most efficient design, surpassing the 119 pole wiggler at 4.8 T and the 159 pole wiggler at 0.6 T. It increases the emittance to $2\epsilon_0$ at field strengths of approximately 0.7 T and with an additional energy loss per turn of only 32 MeV.

However, as figures 48 to 53 show, at 120 GeV and 45.5 GeV the situation is reversed and the 3 pole wiggler requires the highest field strengths of all the designs in order to increase the emittance. It however causes the least additional energy loss per turn. While at an energy of 120 GeV the 159 pole wiggler increases the emittance to $1.1\epsilon_0$ at a field strength

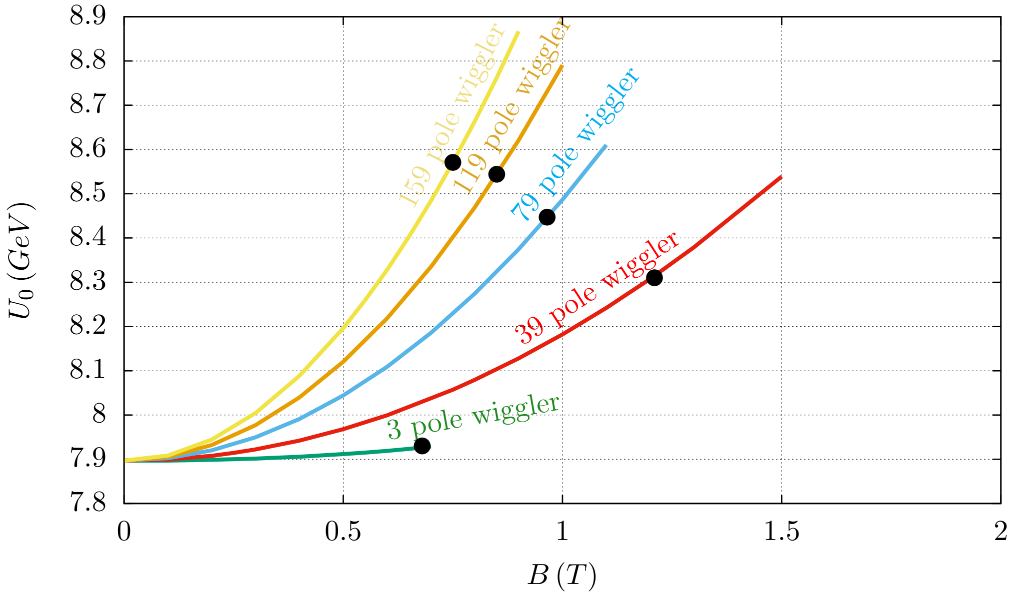

Figure 46: Energy loss per turn U_0 against the magnetic field of the wiggler main poles B for the 3, 39, 79, 119 and 159 pole wigglers in the FCC-ee racetrack lattice at an energy of 175 GeV. The black dots mark the points at which the horizontal emittance is increased to $2\epsilon_0$. Due to varying parameters like number of poles, pole length and gap length, the $\mathcal{H}$-function is different within each wiggler, resulting in different values of additional energy loss per turn. However, there seems to be a trend of increasing energy loss with increasing wiggler pole number.

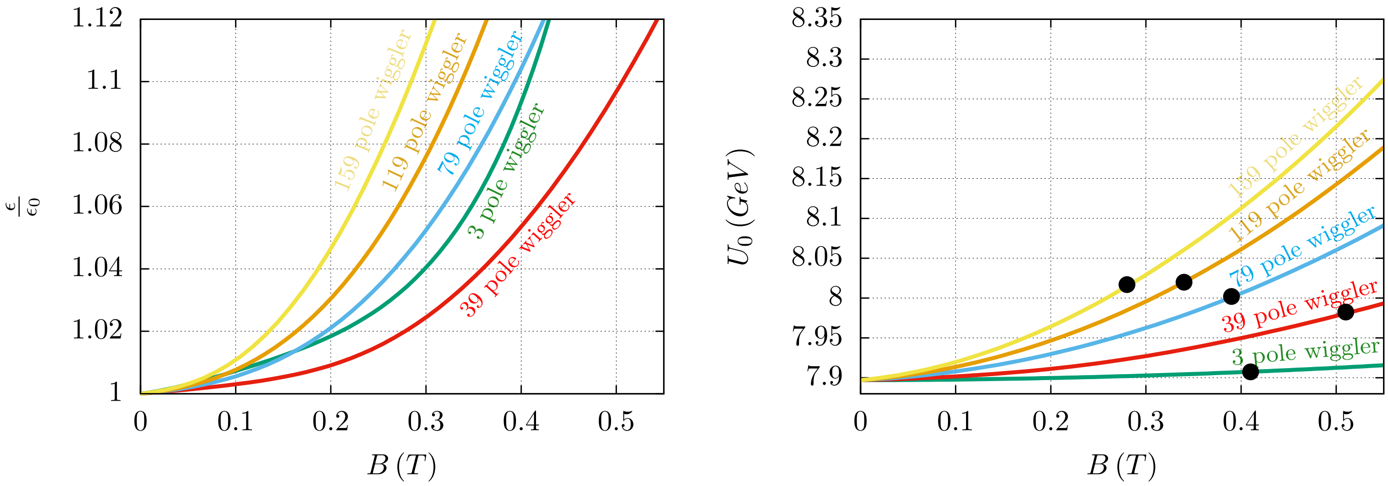

Figure 47: Detailed view of the relative horizontal emittance $\frac{\epsilon}{\epsilon_0}$ and the energy loss per turn U_0 against the magnetic field of the wiggler main poles B for the 3, 39, 79, 119 and 159 pole wigglers in the FCC-ee racetrack lattice at an energy of 175 GeV, showing the important parameter space around an emittance increase of 10 %. The black dots in the right plot mark the points at which the horizontal emittance is increased to $1.1\epsilon_0$.

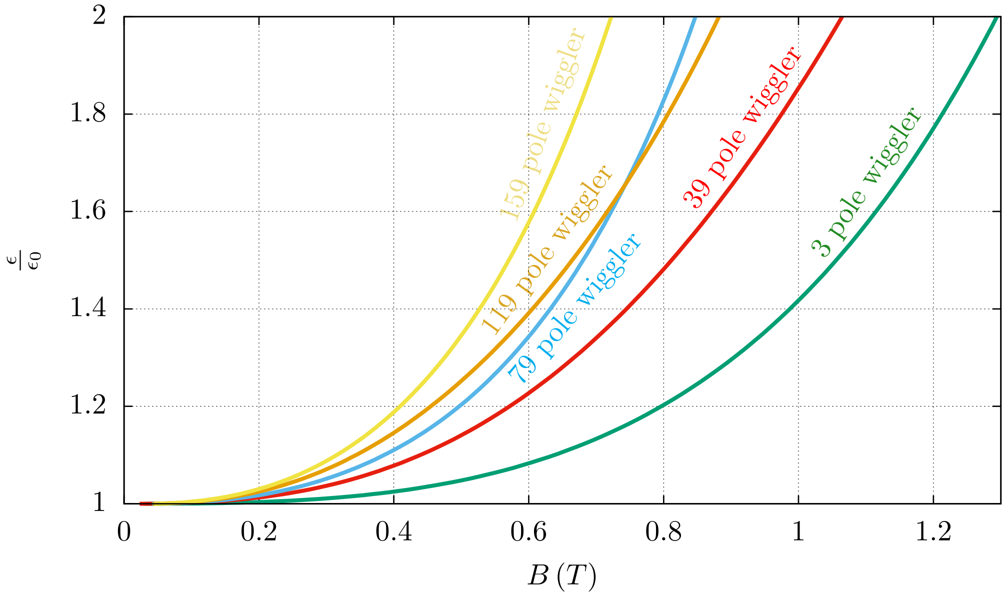

Figure 48: Relative horizontal emittance against the magnetic field of the main wiggler poles B for the 3, 39, 79, 119 and 159 pole wigglers in the FCC-ee racetrack lattice at an energy of 120 GeV.

of 0.23 T and causes an additional energy loss of 71 MeV per turn, the 3 pole wiggler needs a field strength of 0.64 T, but causes an additional energy loss of only 17 MeV. At 45.5 GeV the 159 pole wiggler increases the emittance to $1.1\epsilon_0$ at a field strength of 0.08 T and causes an additional energy loss of 0.65 MeV per turn, the 3 pole wiggler needs a field strength of 0.21 T and causes an additional energy loss of 0.3 MeV. Figures 48 to 53 also show that the correlation between pole number and efficiency in increasing the emittance is no longer as clear as it was in the damping wiggler studies. At 175 GeV, the 3 pole wiggler surpasses the other designs in efficiency with increasing field strength. At 120 GeV, the 79 pole wiggler surpasses the 119 pole wiggler at approx. 0.75 T and at 45.5 GeV, the 79 pole wiggler starts out as the most efficient design, but with increasing field strength drops behind the 159 and 119 pole wiggler.
At 120 GeV, the critical energy at field strengths causing an emittance increase of 10 % ranges from 3 MeV in case of the 159 pole wiggler to 6.1 MeV in case of the 3 pole wiggler. At 45.5 GeV, it ranges from 0.1 MeV in case of the 159 pole wiggler to 0.29 MeV in case of the 39 pole wiggler.

This marks the end of the wiggler studies of FCC-ee within this thesis. Even though they are rather fundamental with no specific wiggler or magnet design in mind, some important points can be derived from them:

- The specific design of a damping wiggler is of little relevance, as the emittance is

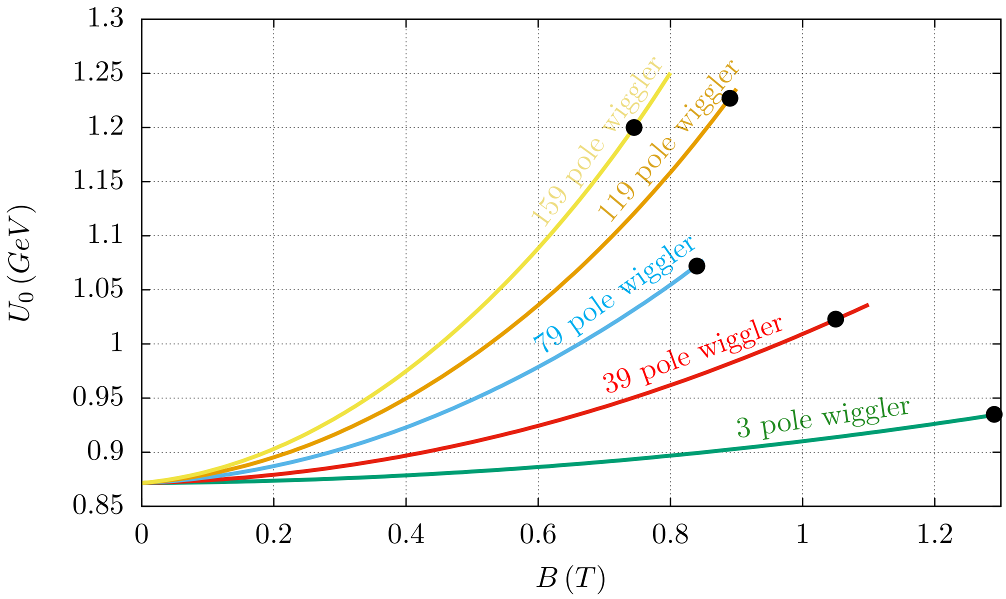

Figure 49: Energy loss per turn U_0 against the magnetic field of the wiggler main poles B for the 3, 39, 79, 119 and 159 pole wigglers in the FCC-ee racetrack lattice at an energy of 120 GeV. The black dots mark the points at which the horizontal emittance is increased by a factor of 2. Due to varying parameters like number of poles, pole length and gap length, the $\mathcal{H}$-function is different within each wiggler, resulting in different values of additional energy loss per turn. However, there seems to be a trend of increasing energy loss with increasing wiggler pole number.

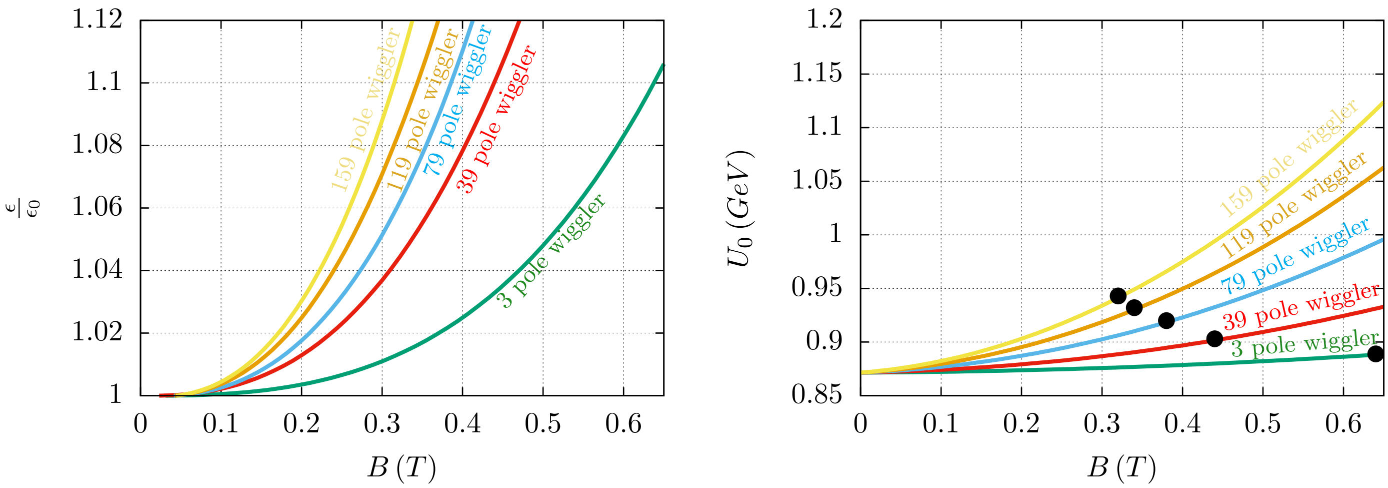

Figure 50: Detailed view of the relative horizontal emittance $\frac{\epsilon}{\epsilon_0}$ and the energy loss per turn U_0 against the magnetic field of the wiggler main poles B for the 3, 39, 79, 119 and 159 pole wigglers in the FCC-ee racetrack lattice at an energy of 120 GeV, showing the important parameter space around an emittance decrease of 10 %. The black dots in the right plot mark the points at which the horizontal emittance is increased by 10 %.

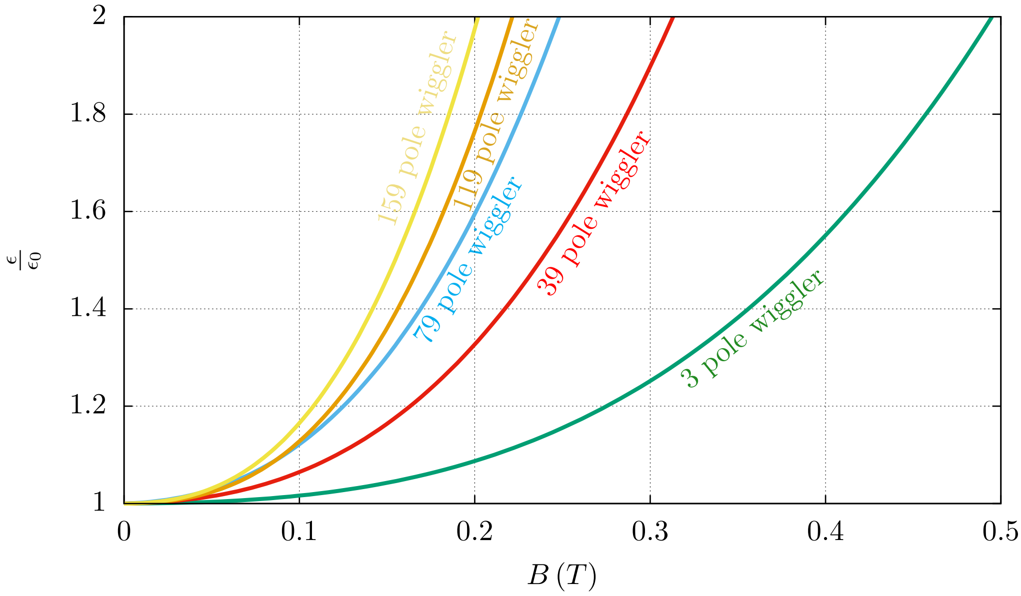

Figure 51: Relative horizontal emittance against the magnetic field of the main wiggler poles B for the 3, 39, 79, 119 and 159 pole wigglers in the FCC-ee racetrack lattice at an energy of 45.5 GeV.

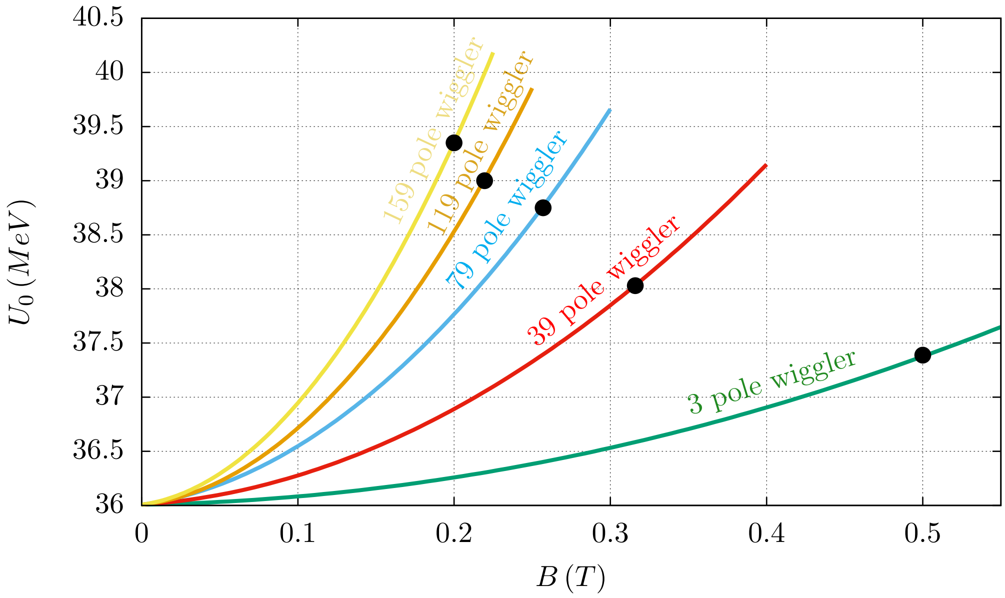

Figure 52: Energy loss per turn U_0 against the magnetic field of the wiggler main poles B for the 3, 39, 79, 119 and 159 pole wigglers in the FCC-ee racetrack lattice at an energy of 45.5 GeV. The black dots mark the points at which the horizontal emittance is increased to $2\epsilon_0$. Due to varying parameters like number of poles, pole length and gap length, the $\mathcal{H}$-function is different within each wiggler, resulting in different values of additional energy loss per turn. However, there seems to be a trend of increasing energy loss with increasing wiggler pole number.

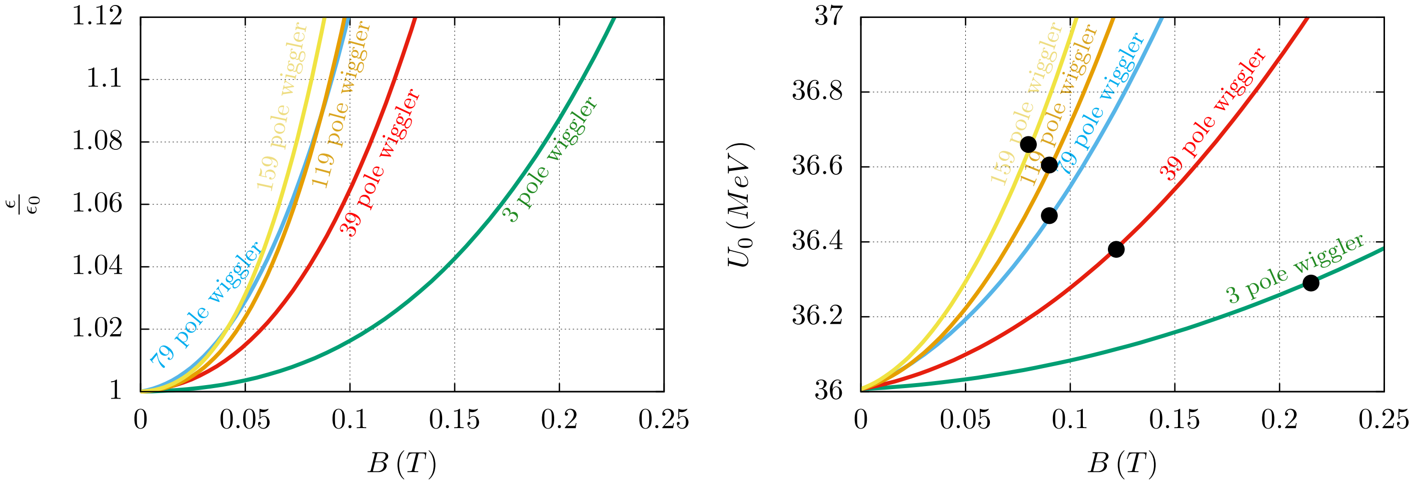

Figure 53: Detailed view of the relative horizontal emittance $\frac{\epsilon}{\epsilon_0}$ and the energy loss per turn U_0 against the magnetic field of the wiggler main poles B for the 3, 39, 79, 119 and 159 pole wigglers in the FCC-ee racetrack lattice at an energy of 45.5 GeV, showing the important parameter space around an emittance decrease of 10 %. The black dots in the right plot mark the points at which the horizontal emittance is increased $1.1\epsilon_0$.

decreased only by the effect of radiation damping and thus only depends on the sum of the squared dipole angles of the wiggler dipoles. In order to optimize damping efficiency, the dispersion created within the wiggler and thus $\mathcal{I}_{5,wiggler}$ should be kept as small as possible, resulting in wigglers with many poles, as well as small pole lengths and gaps.

- For excitation wigglers on the other hand, the actual wiggler design does matter. In order to increase the impact of the wiggler on the emittance, it should be placed in locations of a high $\mathcal{H}$-function in order to maximize $\mathcal{I}_{5,wiggler}$. Additionally, parameters like wiggler, pole and gap length greatly influence the dispersion and thus the $\mathcal{H}$-function created within the wiggler. Wiggler designs with fewer and longer poles, stronger magnetic fields, as well as longer gaps between the poles should be used in order to minimize the number of wigglers necessary.

- At 175 and 120 GeV, the critical energy of the synchrotron radiation emitted by the wigglers surpasses the pair production threshold of 1 MeV. When interacting with matter, this radiation can spontaneously create electron positron pairs, which can produce undesirable background signals in particle detectors. To prevent this, either wiggler dipoles cannot be allowed to surpass a certain field strength, or additional measures must be taken in order to absorb the wiggler radiation. Option one would mean that in FCC-ee at 175 GeV, wiggler dipoles are not allowed to surpass a field strength of 0.05 T, which is approximately the field strength of the arc dipoles. On the other hand, wiggler poles should be kept short in order to minimize the internal dispersion. With the given constraints, it is impossible to build a wiggler, which influences the beam emittance in a noticeable way. Therefore, it will most likely be necessary to take measures towards absorbing the radiation emitted by wigglers.

- Every design presented in these studies except for the 3 pole wiggler can actually be used both as a damping and as an excitation wiggler, depending on whether they are installed in a section with or without dispersion. The excitation wigglers have been placed in regions, where the dispersion is approximately 0.1 m. The dispersion in the arc sections of the FCC-ee racetrack lattice oscillates between 0.06 and 0.12 m, a similar dispersion can thus be introduced to straight sections simply by removing the dispersion suppressors of these sections. The same wiggler design can therefore be used to both de- and increase the emittance by 10 %, simply by adjusting the dispersion in the areas, in which said wiggler is installed.

5 Numerical Chromaticity Correction

In section 2 it was explained that the correction of the natural chromaticity of an accelerator is a crucial part of accelerator design. Chromaticity correction is necessary in order to minimize a tune shift with varying beam energy, which could cause the beam to hit an optical resonance and become unstable. Similar to the first order of the chromaticity,

$$Q' = \frac{dQ}{d(\frac{\Delta p}{p_0})}, \tag{80}$$

higher orders are defined as

$$Q^{(n)} = \frac{d^n Q}{d(\frac{\Delta p}{p_0})^n}. \tag{81}$$

Depending on these chromaticities, the tune shift can be expressed as

$$\Delta Q = (\frac{\Delta p}{p_0})Q^{(1)} + (\frac{\Delta p}{p_0})^2 Q^{(2)} + (\frac{\Delta p}{p_0})^3 Q^{(3)} + (\frac{\Delta p}{p_0})^4 Q^{(4)}. \tag{82}$$

Due to the size of FCC-ee and the energy at which it is operated, chromaticities are in an order of magnitude never before seen in an accelerator (see table 5). In order to ensure a minimal tune shift and to achieve a momentum acceptance of 2 %, chromaticity correction schemes must correct the chromaticity up to the fourth order. The sextupoles necessary to accomplish this need to be stronger than ever before. For comparison, the strengths of sextupoles used for chromaticity correction in LEP were in an order of magnitude of $10^{-1}\,\mathrm{Tm}^{-2}$. In FCC-ee, these strengths are an order of magnitude higher, reaching values of up to $5\,\mathrm{Tm}^{-2}$. Sextupole fields this strong have never been used in an accelerator before, so their influence on beam parameters like the emittance cannot be fully predicted. This is why in these studies, different chromaticity correction schemes are introduced and compared as to how they influence the momentum acceptance of the machine as well as if they have any detrimental influence on the beam emittance.

Downhill Simplex Algorithm

In general, chromaticity correction schemes involve carefully adjusted groups of sextupoles or sextupole families with well-defined phase advances between each element in the arcs of the accelerator as well as around the interaction points. A detailed work on this can be found in [9]. Normally, the optimization of the sextupole strengths is done with the built-in matching tools of *MAD-X*. Unfortunately, in *MAD-X* it is impossible to match the

Table 5: Chromaticities in FCC-ee up to fourth order

$Q_x^{(1)}$	$-5.85735670 * 10^2$
$Q_y^{(1)}$	$-8.59981425 * 10^2$
$Q_x^{(2)}$	$-1.68890097 * 10^4$
$Q_y^{(2)}$	$-2.00410338 * 10^6$
$Q_x^{(3)}$	$-2.50481275 * 10^{14}$
$Q_y^{(3)}$	$-1.67466100 * 10^{14}$
$Q_x^{(4)}$	$-5.00962176 * 10^{18}$
$Q_y^{(4)}$	$-3.34896167 * 10^{18}$

higher orders of the chromaticity globally for the whole machine. Therefore, a Downhill-Simplex optimization algorithm was created, which uses *MAD-X* to calculate the orders of chromaticity and creates a penalty function, which in this case has the form

$$\Delta Q = (Q_x^{(1)})^2 + (Q_y^{(1)})^2 + \delta^2[(Q_x^{(2)})^2 + (Q_y^{(2)})^2] + \delta^4[(Q_x^{(3)})^2 + (Q_y^{(3)})^2] + \delta^6[(Q_x^{(4)})^2 + (Q_y^{(4)})^2] \tag{83}$$

with the relative energy deviation δ and the n-th order chromaticity $Q^{(n)}$. This penalty function can of course be modified in many ways. For example, weight factors can be introduced to prioritise a certain order of chromaticity, etc. The algorithm then minimizes the function using the *downhill simplex method*, which works the following way:
The penalty function is essentially a function of N sextupole strengths $\Delta Q = \Delta Q(K_2)$, it is therefore a function in N dimensional space. The algorithm now creates a simplex, which is a (N+1)-polytope in this N dimensional space. In two dimensions for example, a simplex would be a triangle, in three dimensions a tetrahedron, and so forth.
Each point of the simplex corresponds to one set of values of the N sextupole strengths. After the simplex is created, the algorithm calculates ΔQ at each of the N+1 simplex vertices and orders them according to their value of the penalty function. The simplex point with the highest value is excluded. All the other points are used to calculate their geometric center or centroid. Now, the algorithm goes through a series of geometric operations, which are repeated until the minimum of the penalty function is found. The sequence of the geometric operations conducted is the following:
Firstly, the simplex point with the highest value of the penalty function is reflected through the centroid of the remaining points. If the reflected point now has the lowest value of the penalty function, the reflection is extended until a reflected point has a higher penalty function than the point before. This point then replaces the simplex point with the highest penalty function and the process is repeated.

If the reflection of the worst point produces a point with a penalty function higher than the values of all the remaining simplex points, a contraction of the worst point towards the geometric center of the remaining points must produce a point with a penalty function better than the worst simplex point. If this new simplex point has again the worst penalty function of all remaining simplex points, it is reflected through the centroid of the remaining points. Otherwise, the new worst point is determined and the process starts anew. This way, the simplex converges to a minimum of the penalty function, optimizing the set of initial parameters. In FCC-ee, this algorithm was applied to optimize families of sextupoles in order to minimize the horizontal and vertical chromaticities up to the fourth order.

Two different types of sextupole schemes were optimized with the downhill simplex algorithm: a global chromaticity correction scheme using a number of sextupole families in the arcs as well as a combination of global and local chromaticity correction, which uses sextupole families in the arcs and a number of sextupoles in the straight sections around the two interaction points. Four different configurations of global chromaticity correction were tested: 1 sextupole family per arc and per plane, resulting in 8 individually powered sextupole families. 2 families per arc in the horizontal and 3 per arc in the vertical plane, resulting in 20 individually powered sextupole families. 6 families per arc and per plane, resulting in 48 individually powered sextupole families, and finally, a scenario with 54 families per plane. In this scenario the sextupole families were not redefined in each arc. For example, the third sextupole in each arc belongs to one sextupole family, the fourth belongs to another, and so forth. In the short arcs, each sextupole represents an individual family, resulting in 42 sextupole families per plane. The sextupoles in the long arcs were divided into 54 families. The first 42 families therefore consist of eight sextupoles each, the following 14 only exist in the long arcs and consist of four sextupoles each. This design was chosen mainly to see whether there is a significant difference between defining sextupole families globally and defining them individually in each arc.
Three different configurations of combined global and local schemes were tested: 1 sextupole family per arc and per plane, 2 families per arc in the horizontal and 3 per arc in the vertical plane and 6 families per arc and per plane. Tables 6 and 7 show the chromaticities up to fourth order after applying the global and combined correction schemes respectively. With each sextupole correction scheme, the chromaticites can be reduced by several orders of magnitude. However, the combined correction schemes generally reduce the third and fourth order of chromaticity to a larger extent than the global correction schemes. This is due to the fact that a great deal of the chromaticity is created by the strong focussing quadrupoles around the interaction points. The sextupoles of the local chromaticity correction scheme can correct these contributions much more efficiently than the global correction scheme which only uses sextupoles in the arcs. Figure 54 shows the

Table 6: Chromaticities in FCC-ee up to fourth order after applying the different global chromaticity correction schemes.

(a) 1 family per arc and plane

$Q_x^{(1)}$	$-3.52400061 * 10^1$
$Q_y^{(1)}$	$3.35003426 * 10^3$
$Q_x^{(2)}$	$-2.15943537 * 10^3$
$Q_y^{(2)}$	$3.06818050 * 10^5$
$Q_x^{(3)}$	$-1.15603112 * 10^7$
$Q_y^{(3)}$	$1.25014933 * 10^{10}$
$Q_x^{(4)}$	$-1.97375675 * 10^{10}$
$Q_y^{(4)}$	$-2.54868382 * 10^{10}$

(b) 2 families per arc in the horizontal, 3 in the vertical plane

$Q_x^{(1)}$	$2.88279324 * 10^1$
$Q_y^{(1)}$	$3.26153739 * 10^1$
$Q_x^{(2)}$	$-6.95331249 * 10^2$
$Q_y^{(2)}$	$-4.05765961 * 10^4$
$Q_x^{(3)}$	$-2.20436098 * 10^6$
$Q_y^{(3)}$	$-1.70802602 * 10^6$
$Q_x^{(4)}$	$-4.66343408 * 10^6$
$Q_y^{(4)}$	$-2.57387001 * 10^6$

(c) 6 families per arc and plane

$Q_x^{(1)}$	$-5.01534788 * 10^2$
$Q_y^{(1)}$	$2.16476966 * 10^3$
$Q_x^{(2)}$	$6.90392465 * 10^3$
$Q_y^{(2)}$	$1.18283016 * 10^5$
$Q_x^{(3)}$	$-1.58851598 * 10^7$
$Q_y^{(3)}$	$6.18922029 * 10^9$
$Q_x^{(4)}$	$2.22943299 * 10^{10}$
$Q_y^{(4)}$	$4.20327069 * 10^9$

(d) 54 sextupole families per plane in total

$Q_x^{(1)}$	$3.75855915 * 10^1$
$Q_y^{(1)}$	$-2.31680187 * 10^1$
$Q_x^{(2)}$	$-1.26919849 * 10^2$
$Q_y^{(2)}$	$-1.51144826 * 10^4$
$Q_x^{(3)}$	$3.03378710 * 10^6$
$Q_y^{(3)}$	$-6.87511605 * 10^7$
$Q_x^{(4)}$	$-5.53882273 * 10^9$
$Q_y^{(4)}$	$-4.22936364 * 10^{10}$

horizontal and vertical tune against the relative momentum deviation $\delta = \frac{\Delta p}{p_0}$ without chromaticity correction, as well as with a combination of local and global chromaticity correction with 1 family per arc and plane, with 2 per arc in the horizontal and 3 per arc in the vertical plane as well as with 6 families per arc and plane, respectively. With a combined correction scheme of 6 sextupole families per arc and plane as well as a local correction around the IPs, the negative and positive momentum acceptance of FCC-ee can be increased from -0.07 and 0.01 % without any correction to -0.38 and 0.5 %, respectively.

Influence on Beam Emittance

Additionally to the momentum acceptance tests it was tested, if the implementation of these correction schemes has any influence on the beam emittance. On that account, the emittance was calculated for each correction scheme at beam energies of 45.5, 120 and

Table 7: Chromaticities in FCC-ee up to fourth order after applying the different combined chromaticity correction schemes.

(a) 1 family per arc and plane

$Q_x^{(1)}$	$-2.60800547 * 10^0$
$Q_y^{(1)}$	$9.29312270 * 10^2$
$Q_x^{(2)}$	$-6.64013442 * 10^1$
$Q_y^{(2)}$	$-1.48097471 * 10^0$
$Q_x^{(3)}$	$-3.53636551 * 10^4$
$Q_y^{(3)}$	$-7.96904942 * 10^3$
$Q_x^{(4)}$	$2.91038305 * 10^5$
$Q_y^{(4)}$	$1.00044417 * 10^5$

(b) 2 families per arc in the horizontal, 3 in the vertical plane

$Q_x^{(1)}$	$-3.68401896 * 10^0$
$Q_y^{(1)}$	$1.78168717 * 10^1$
$Q_x^{(2)}$	$-1.16555668 * 10^2$
$Q_y^{(2)}$	$-2.95064339 * 10^3$
$Q_x^{(3)}$	$4.08647338 * 10^2$
$Q_y^{(3)}$	$-1.6044055 * 10^3$
$Q_x^{(4)}$	$-1.36424205 * 10^4$
$Q_y^{(4)}$	$9.09494702 * 10^4$

(c) 6 families per arc and plane

$Q_x^{(1)}$	$-2.60800547 * 10^0$
$Q_y^{(1)}$	$9.29312270 * 10^2$
$Q_x^{(2)}$	$-6.64013442 * 10^1$
$Q_y^{(2)}$	$-1.48097471 * 10^0$
$Q_x^{(3)}$	$-3.53636551 * 10^4$
$Q_y^{(3)}$	$-7.96904942 * 10^3$
$Q_x^{(4)}$	$2.91038305 * 10^5$
$Q_y^{(4)}$	$1.00044417 * 10^5$

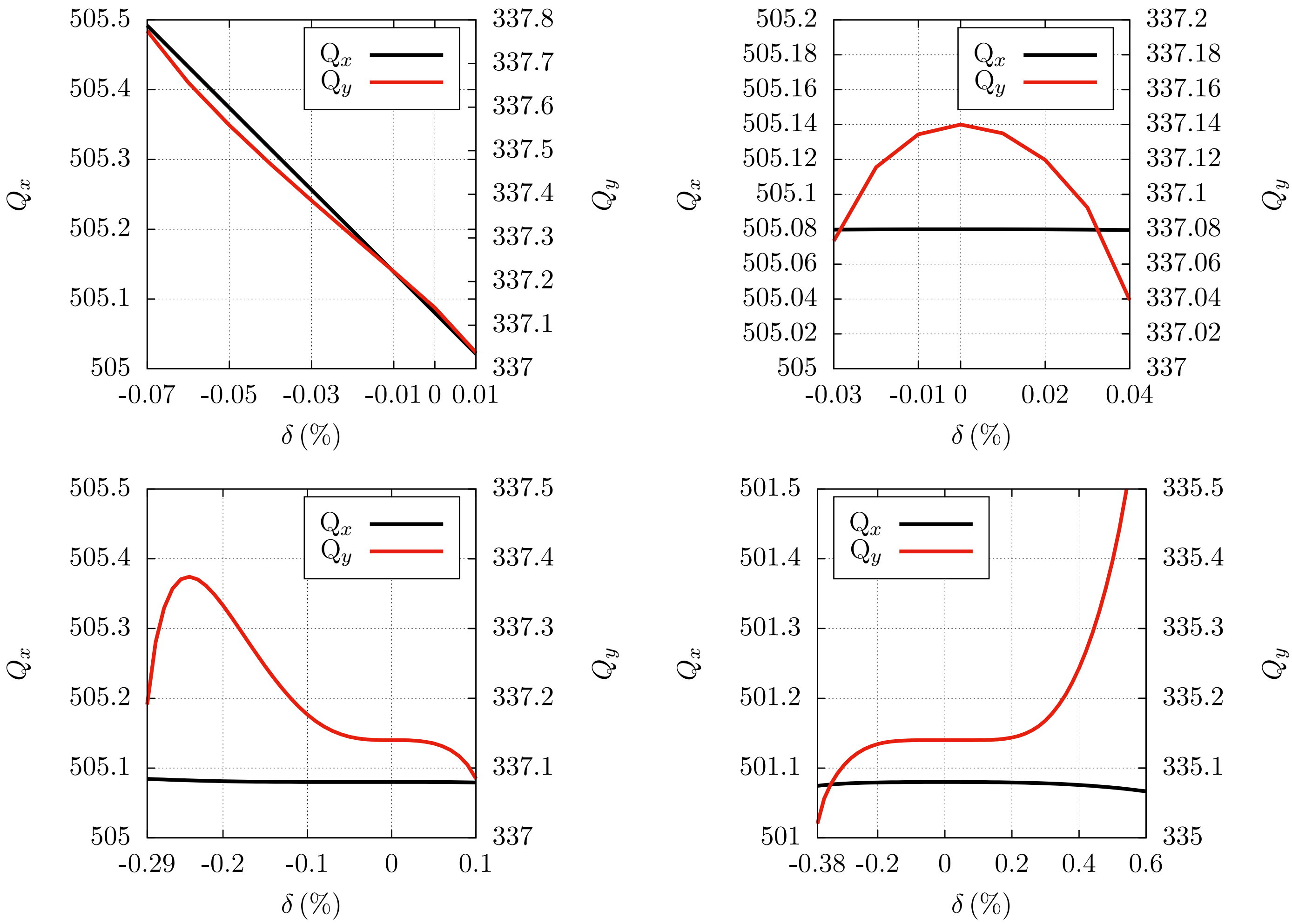

Figure 54: Horizontal and vertical tune against the relative momentum deviation δ in four different stages of chromaticity correction. The momentum acceptance is limited by either the horizontal or vertical tune crossing an integer or half integer resonance, or by both tunes having the same fractional tune, resulting in a coupling resonance. In either case, the beam becomes unstable. Top left: momentum acceptance without a sextupole correction scheme. Top right: momentum acceptance with a chromaticity correction scheme of one sextupole family per plane. Only the linear chromaticity is corrected. Bottom left: momentum acceptance with a chromaticity correction scheme of 2 sextupole families in the horizontal plane and three families in the vertical plane per arc. Chromaticities of first and second order are corrected analytically by correcting the W-function, see [9]. Bottom right: momentum acceptance with a chromaticity correction scheme of 6 sextupole families per arc and per plane. The sextupole strengths are determined by the downhill-simplex algorithm. Chromaticities are corrected up to the fourth order.

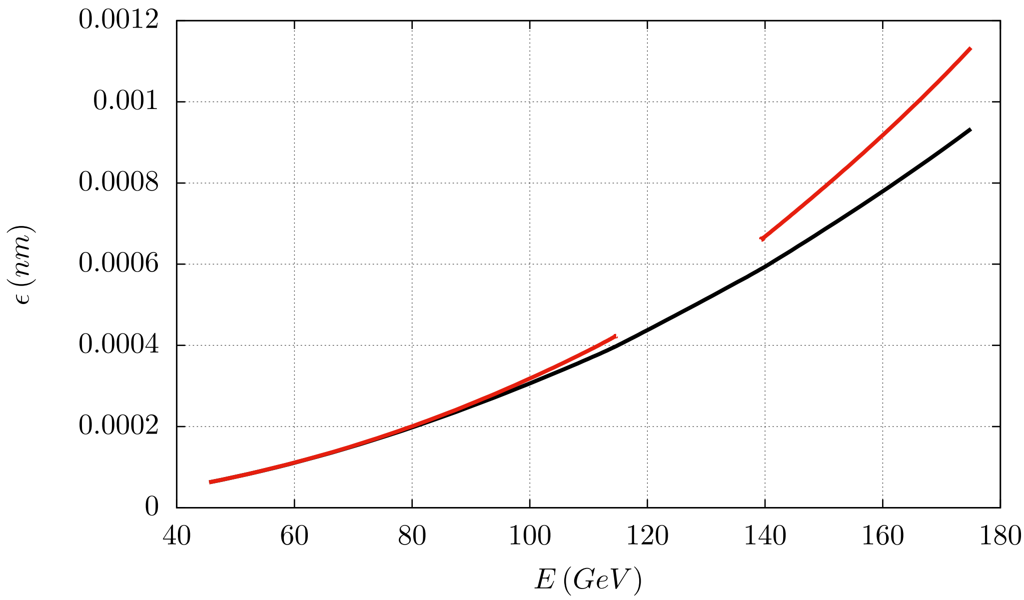

Figure 55: Horizontal emittance for different beam energies without chromaticity correction (black) and with a global chromaticity correction scheme with 2 sextupole families per arc in the horizontal and 3 in the vertical plane (red). This particular chromaticity correction scheme causes an increase in the beam emittance, which increases with increasing beam energy. While at 45.5 GeV the relative error is only 0.05 %, at 175 GeV it is already 21.4 %. In addition to that, the correction scheme causes the beam to become unstable in an energy range between 114.68 and 139.3 GeV.

175 GeV and compared to the design emittance at the respective energy. At 45.5 GeV, the implementation of none of the correction schemes results in an emittance increase higher than approximately 0.05 %. At 120 GeV, the combined correction schemes collectively show a decrease in the emittance of approximately 0.9 %, while the behaviour of the global schemes differs from strategy to strategy. The strategies with 1 and 6 families per arc and plane show an emittance increase of 0.02 % and 0.07 % respectively, the strategy with 54 families per plane causes an emittance increase of 3.5 % and the strategy with 2 families per arc in the horizontal and 3 in the vertical plane causes the beam to become unstable altogether. A detailed overview of the behaviour of this strategy at different energies is shown in figure 55. At 175 GeV, the implementation of any of the presented correction schemes results in an emittance increase. However, the amount of the increase differs widely. The global correction schemes with 1 family per arc and plane, 2 per arc in the horizontal and 3 per arc in the vertical plane, 6 families per arc and plane as well as with 54 families per plane cause an emittance increase of 0.4 %, 21.4 %, 0.4 % and 54.5 %, respectively. The combined global and local correction schemes with 1 family per arc and plane, 2 per arc in the horizontal and 3 per arc in the vertical plane, as well as 6 families per arc and plane cause an emittance increase of 4.2 %, 4.5 % and 6.0 %, respectively.

In conclusion, one can say that first chromaticity studies using a downhill simplex algorithm in order to correct the chromaticity up to the fourth order yields an improvement of the positive and negative momentum acceptance from -0.07 and 0.01 % to -0.38 and 0.5 %, respectively. This value can with sufficient certainty be further improved by a better understanding of the individual orders of chromaticity and how they influence the momentum acceptance of the machine. The penalty function of the algorithm can then be adapted accordingly. In addition to that it should be noted that due to the high sextupole strengths, the implementation of a chromaticity correction system can influence the beam emittance to a large extent. The choice of the correct chromaticity correction scheme in FCC-ee must therefore not be made with the sole focus on optimizing the momentum acceptance of the machine, but also with its influence on the emittance in mind.

6 Summary

In FCC-ee, a large sawtooth effect of up to 1.4 mm at 175 GeV leads to additional orbit distortions and focussing errors caused by the feed-down effect created by a particle passing through a quadrupole or sextupole magnet at a large offset. To solve this problem, dipole magnets can be adjusted to the local beam energy in a process called dipole tapering.
Different tapering scenarios were introduced and their influence on the orbit and beam optics was tested: Individual dipole tapering, meaning the individual adjustment of every dipole to the local beam energy, as well as arcwise or averaged dipole tapering, which grouped a certain number of dipoles into a dipole family and assigned each dipole family an averaged tapered strength. With individual dipole tapering, it was possible to decrease the orbit by six orders of magnitude to the theoretical limit only determined by the length of the dipole and the beam energy. In the FCC-ee racetrack lattice at 175 GeV, this limit is approximately $3 * 10^{-9}$ m.
Using averaged dipole tapering, the orbit reduction depends on the number of dipole families used in the process. With four and six dipole families, the orbit is reduced by a factor of 2.5 and 4.7, respectively. In the FCC-ee racetrack lattice at 175 GeV, this means a maximum orbit offset of $5.5 * 10^{-4}$ and $3 * 10^{-4}$, respectively. Dipole tapering significantly reduces the beta beat introduced by chromaticity correction schemes or misaligned quadrupoles by eliminating all feed-down effects. First tolerance studies show an increased resistance of tapered lattices to quadrupole misalignments.
In order to achieve the highest possible luminosity, FCC-ee was designed to have a certain optimal design emittance. However, various effects can cause small deviations from this design value. In order to regain the optimal luminosity, the beam emittance needs to be tunable by approximately 10 % around the design value. To accomplish this, damping wigglers are installed in the accelerator to decrease the emittance and excitation wigglers to increase it. During the course of this thesis, different wiggler designs, all but one of them applicable as both damping and excitation wigglers, were introduced and compared. It was shown that both an emittance decrease and increase by 10 % are possible with reasonable additional radiation loss. However, the critical energy of the synchrotron radiation emitted by the wiggler poles surpasses the electron positron pair production threshold of 1 MeV at beam energies of 120 and 175 GeV, calling for additional shielding in order to absorb the radiation.
Finally, the influence of different chromaticity correction strategies on the beam emittance was tested. To ensure a small tune shift and to achieve a momentum acceptance of 2 %, chromaticites in FCC-ee need to be corrected up to the fourth order. Several different correction schemes were implemented and an algorithm using the downhill simplex method

was created in order to find the optimum sextupole strengths. Applying this algorithm, the negative and positive momentum acceptance of FCC-ee $\frac{\Delta p}{p_0}$ could be increased significantly from -0.07 and 0.01 % to -0.4 and 0.5 %, respectively. Additionally it was shown that a chromaticity correction scheme in FCC-ee can have significant influence on the beam emittance, one of them increasing it by as much as 54.5 %. The choice of the correct chromaticity correction scheme must therefore not be made with the sole focus on optimizing the momentum acceptance, but also with its influence on the emittance in mind.

Appendix

In this section, further plots of different tapering studies can be found.

Tapering strategy with additional tapering magnets

The following plots show the orbit after the tapering procedure using additional magnets. One can see that, independently of the beam energy and the number of RF sections being used, the orbit always decreases by approximately two orders of magnitude.

Racetrack layout, 45.5 GeV, 2 RF sections

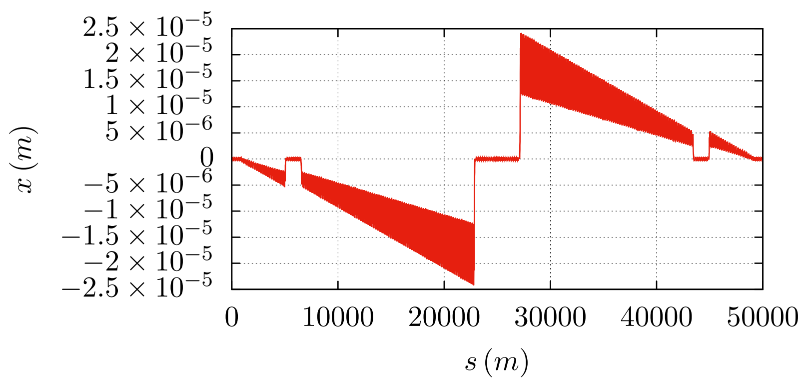

Figure 56: Orbit with a beam energy of 45.5 GeV and two sections with RF cavities before tapering.

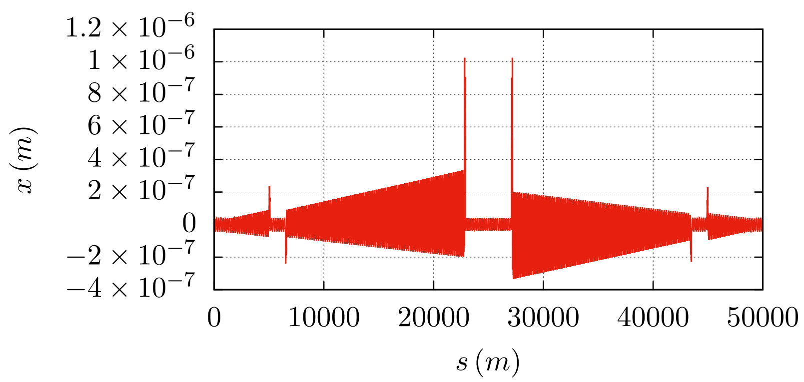

Figure 57: Orbit with a beam energy of 45.5 GeV and two sections with RF cavities after tapering with additional magnets according to the bending angle completion principle.

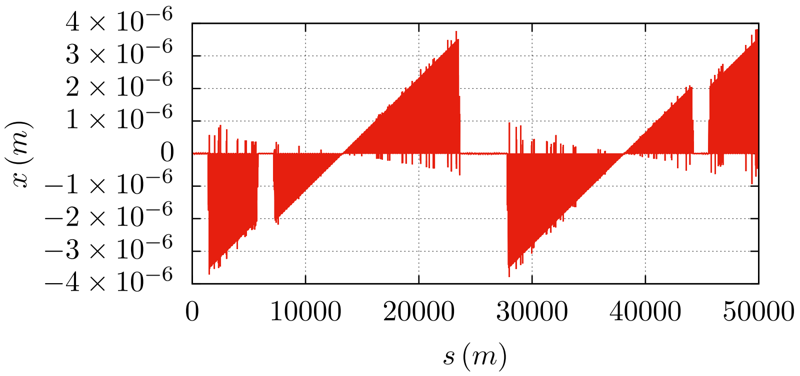

Figure 58: Orbit with a beam energy of 45.5 GeV and two sections with RF cavities after tapering with numerically optimized tapering magnet strengths. The irregularities of the orbit are due to the fact, that the numerical optimization algorithm of MAD-X works reliably only up to a certain lower limit, which the tapered orbit already reached.

Racetrack layout, 45.5 GeV, 4 RF sections

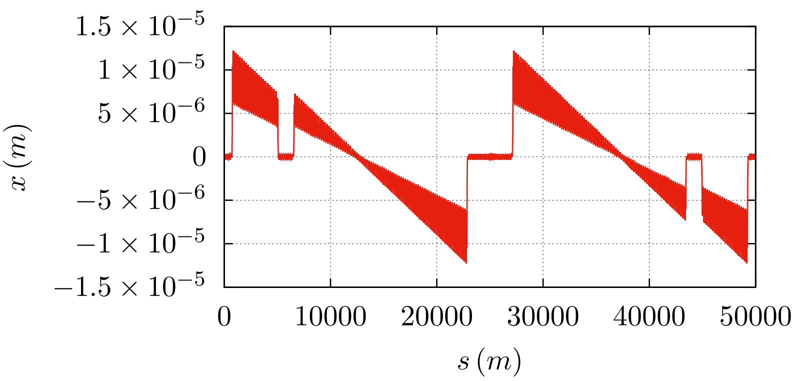

Figure 59: Orbit with a beam energy of 45.5 GeV and four sections with RF cavities before tapering.

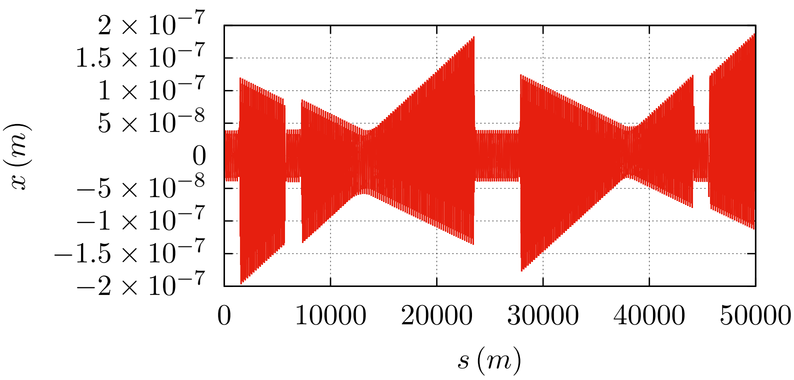

Figure 60: Orbit with a beam energy of 45.5 GeV and four sections with RF cavities after tapering with numerically optimized tapering magnet strengths.

Racetrack layout, 45.5 GeV, 6 RF sections

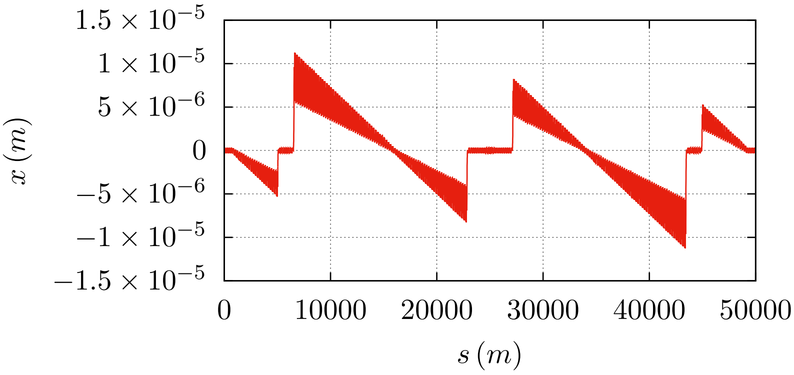

Figure 61: Orbit with a beam energy of 45.5 GeV and six sections with RF cavities before tapering.

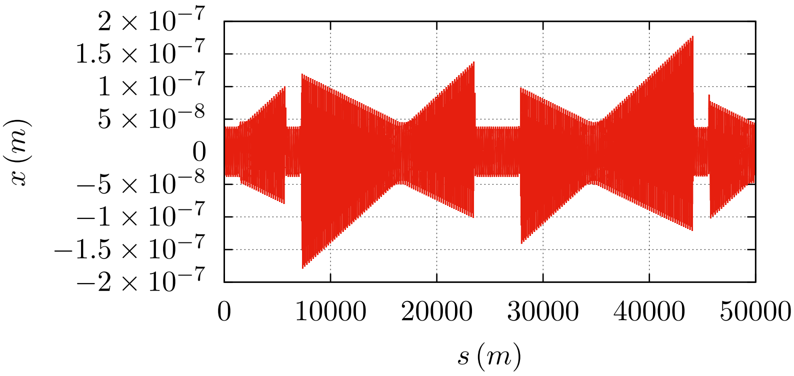

Figure 62: Orbit with a beam energy of 45.5 GeV and six sections with RF cavities after tapering with numerically optimized tapering magnet strengths.

Racetrack layout, 45.5 GeV, 8 RF sections

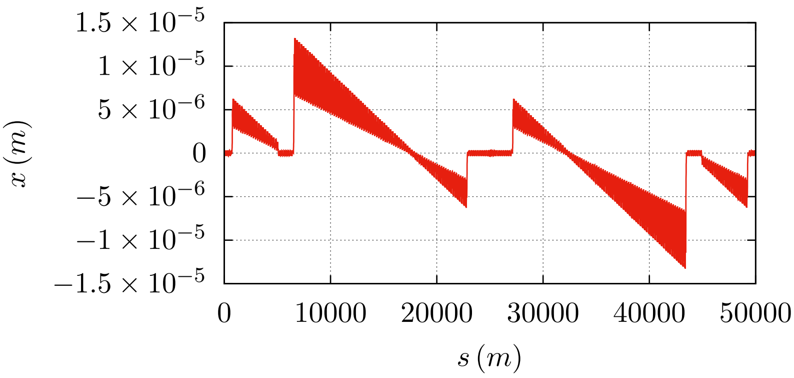

Figure 63: Orbit with a beam energy of 45.5 GeV and eight sections with RF cavities before tapering.

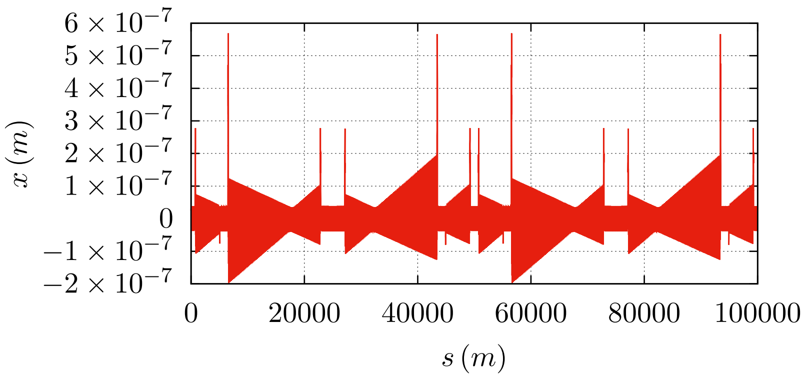

Figure 64: Orbit with a beam energy of 45.5 GeV and eight sections with RF cavities after tapering with additional magnets according to the bending angle completion principle.

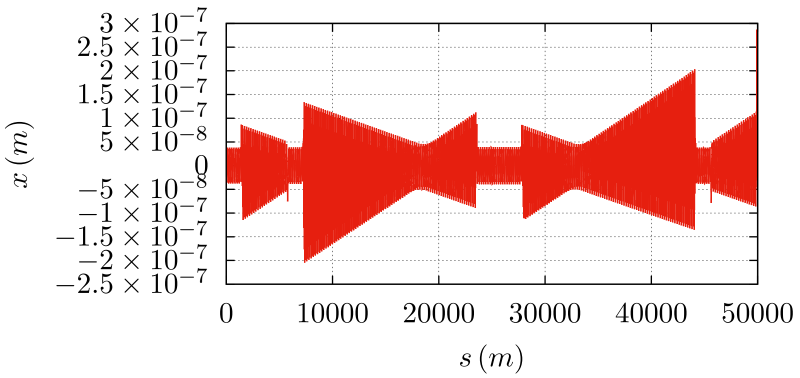

Figure 65: Orbit with a beam energy of 45.5 GeV and eight sections with RF cavities after tapering with numerically optimized tapering magnet strengths.

Racetrack layout, 120 GeV, 2 RF sections

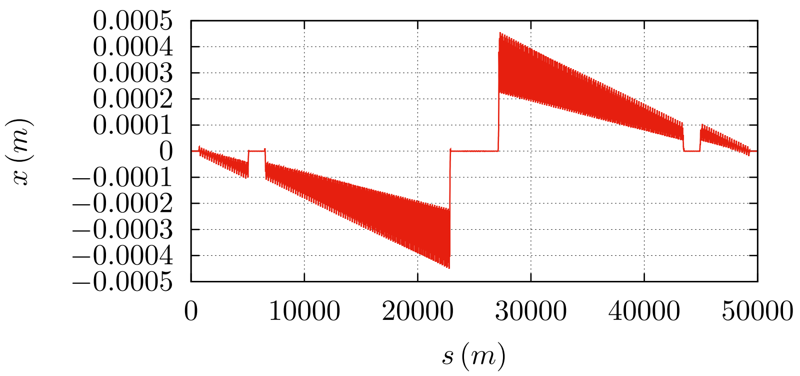

Figure 66: Orbit with a beam energy of 120 GeV and two sections with RF cavities before tapering.

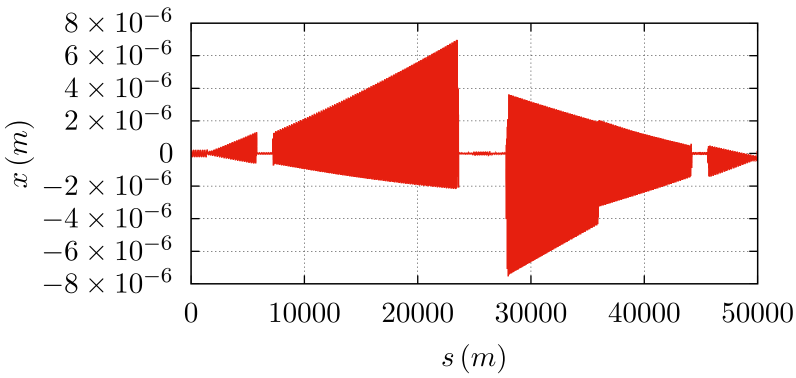

Figure 67: Orbit with a beam energy of 120 GeV and two sections with RF cavities after tapering with numerically optimized tapering magnet strengths.

Racetrack layout, 120 GeV, 4 RF sections

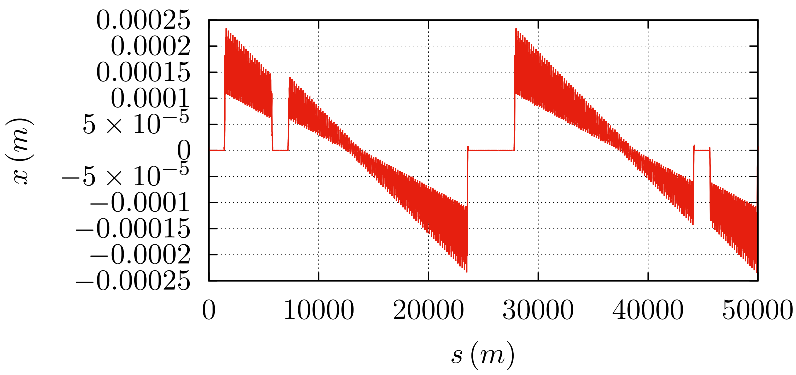

Figure 68: Orbit with a beam energy of 120 GeV and four sections with RF cavities before tapering.

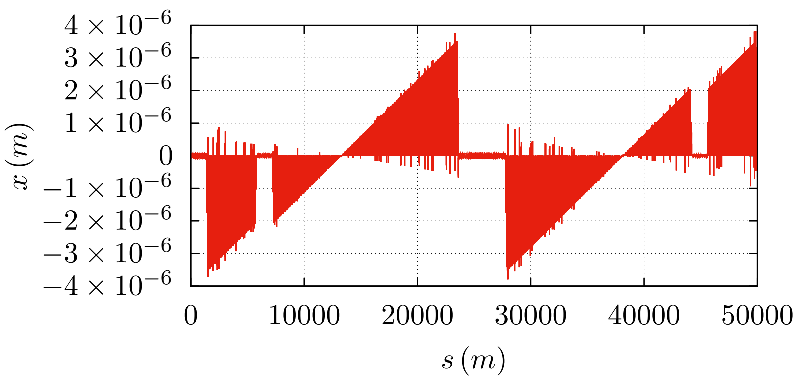

Figure 69: Orbit with a beam energy of 120 GeV and four sections with RF cavities after tapering with numerically optimized tapering magnet strengths.

Racetrack layout, 120 GeV, 6 RF sections

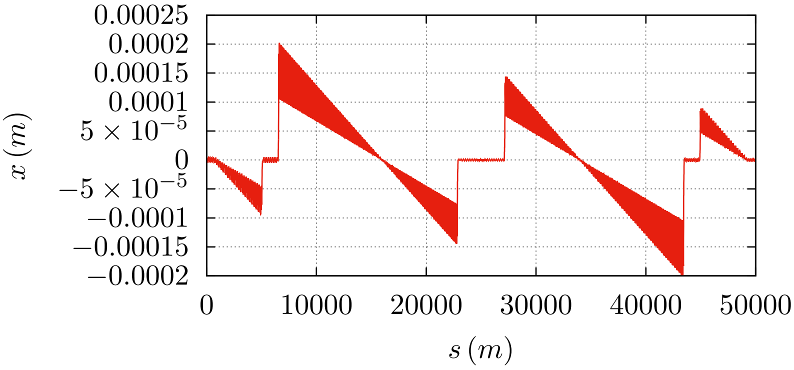

Figure 70: Orbit with a beam energy of 120 GeV and six sections with RF cavities before tapering.

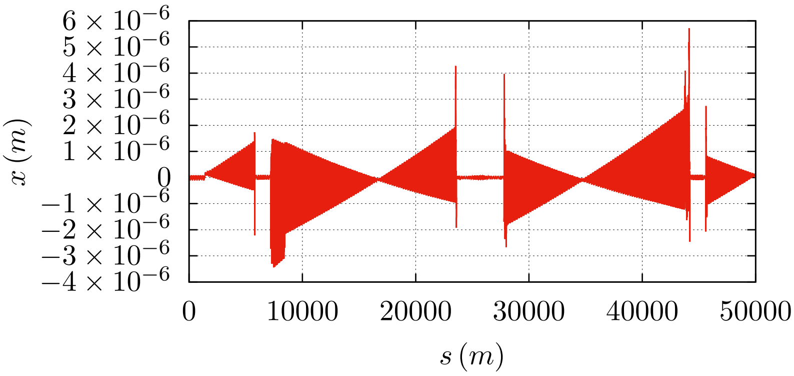

Figure 71: Orbit with a beam energy of 120 GeV and six sections with RF cavities after tapering with numerically optimized tapering magnet strengths.

Racetrack layout, 120 GeV, 8 RF sections

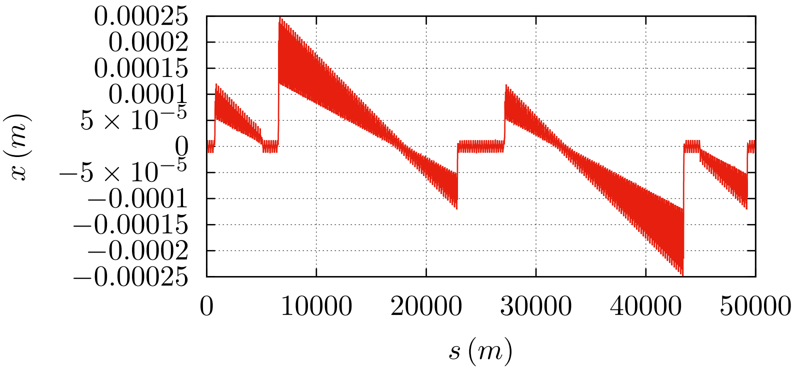

Figure 72: Orbit with a beam energy of 45.5 GeV and eight sections with RF cavities before tapering.

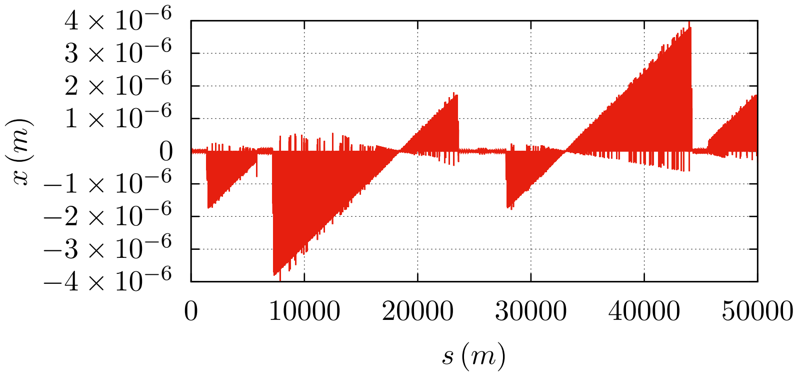

Figure 73: Orbit with a beam energy of 120 GeV and eight sections with RF cavities after tapering with numerically optimized tapering magnet strengths.

Racetrack layout, 175 GeV, 2 RF sections

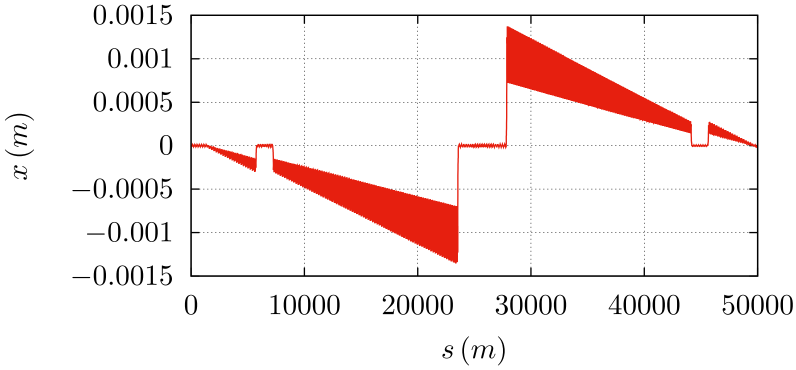

Figure 74: Orbit with a beam energy of 175 GeV and two sections with RF cavities before tapering.

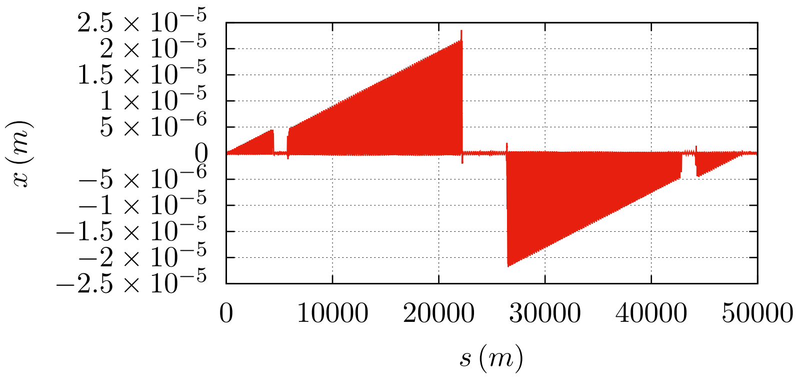

Figure 75: Orbit with a beam energy of 175 GeV and two sections with RF cavities after tapering with numerically optimized tapering magnet strengths.

Racetrack layout, 175 GeV, 4 RF sections

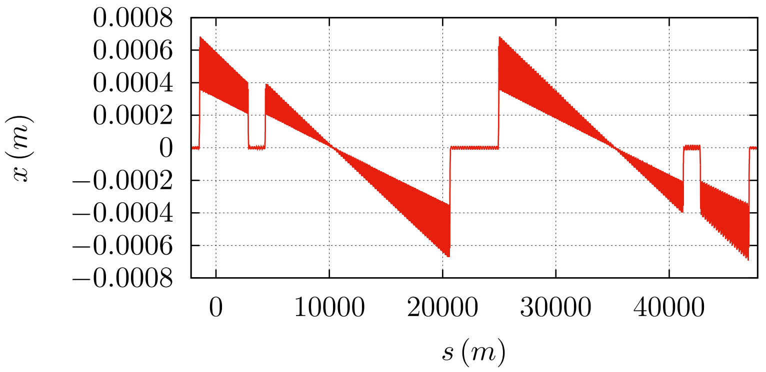

Figure 76: Orbit with a beam energy of 175 GeV and four sections with RF cavities before tapering.

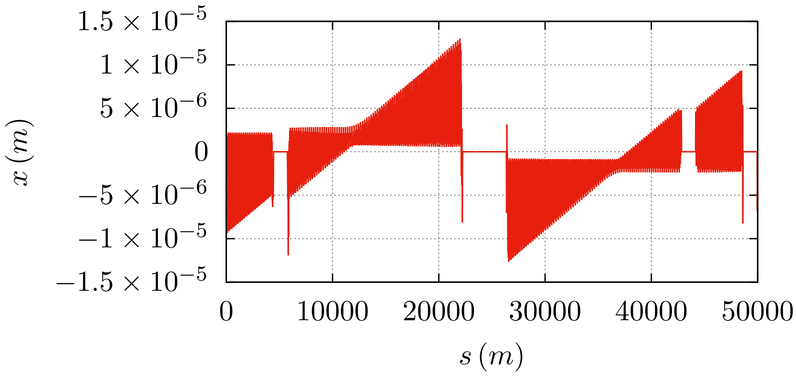

Figure 77: Orbit with a beam energy of 175 GeV and four sections with RF cavities after tapering with numerically optimized tapering magnet strengths.

Racetrack layout, 175 GeV, 6 RF sections

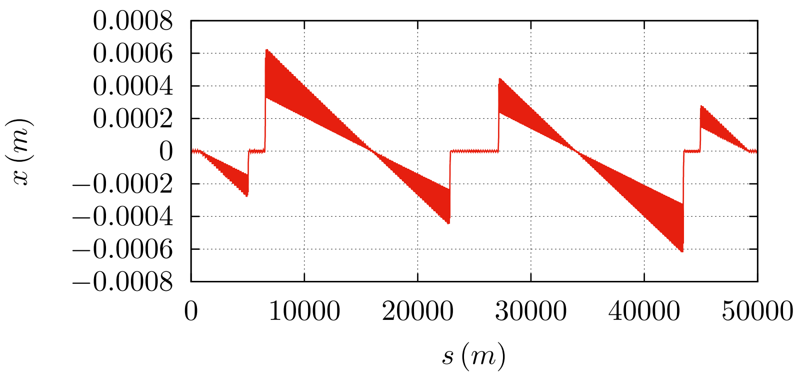

Figure 78: Orbit with a beam energy of 175 GeV and six sections with RF cavities before tapering.

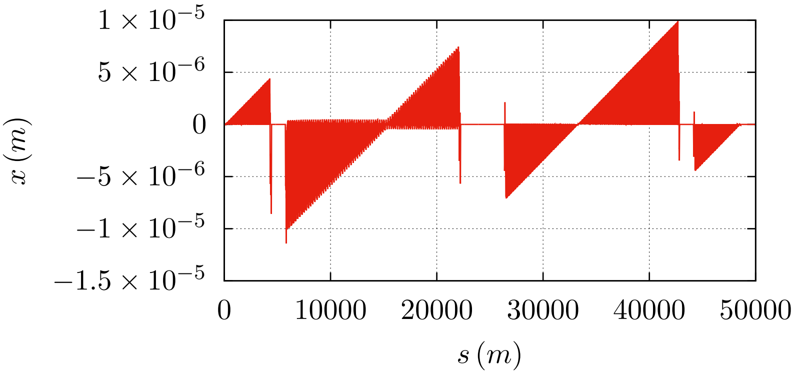

Figure 79: Orbit with a beam energy of 175 GeV and six sections with RF cavities after tapering with numerically optimized tapering magnet strengths.

Racetrack layout, 175 GeV, 8 RF sections

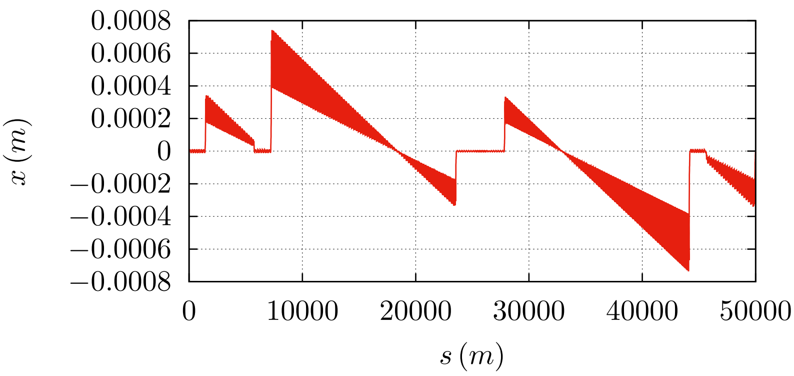

Figure 80: Orbit with a beam energy of 45.5 GeV and eight sections with RF cavities before tapering.

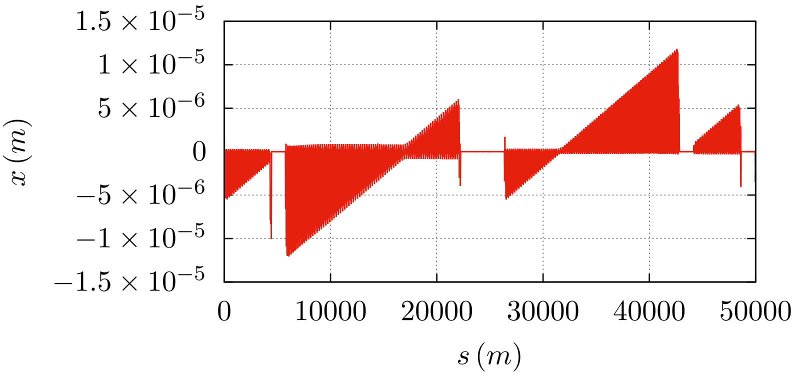

Figure 81: Orbit with a beam energy of 175 GeV and eight sections with RF cavities after tapering with numerically optimized kicker magnet strengths.

References

[1] H. Grote, F. Schmidt, L. Deniau, G. Roy. **The *MAD-X* Program, User's Reference Manual.** Feb. 19, 2015

[2] Website of the MAD project. [Online]. Available: http://mad.web.cern.ch/mad/

[3] H. Grote, F.C. Iselin. **The MAD Program, User's Reference Manual.** Jan. 18, 1994

[4] R.H. Helm, M.J. Lee, P.L. Morton, M. Sands. **Evaluation of Synchrotron Radiation Integrals.** Jun. 1973

[5] M. Sands. **The physics of electron storage rings. An introduction.** Nov. 1970

[6] K. Wille. **Physik der Teilchenbeschleuniger und Synchrotronstrahlungsquellen.** Teubner, 1996

[7] H. Wiedemann. **Particle Accelerator Physics.** Springer, 1993

[8] T. Raubenheimer. **The Generation and Acceleration of Low Emittance Flat Beams For Future Linear Colliders.** Nov. 1991

[9] B. Haerer. **Lattice Design and Beam Optics Calculations for the new Large-Scale Electron-Positron-Collider FCC-ee.** Feb. 2017

[10] S. Aumon, B.Haerer, B. Holzer, K. Oide, A. Doblhammer. **Tolerance Studies and Dispersion Free Steering for Extreme Low Emittance in the FCC-ee Project.** May 2016

[11] **Future Circular Collider Study Kickoff Meeting.** *https://indico.cern.ch/event/282344/*

[12] *http://tlep.web.cern.ch/*